

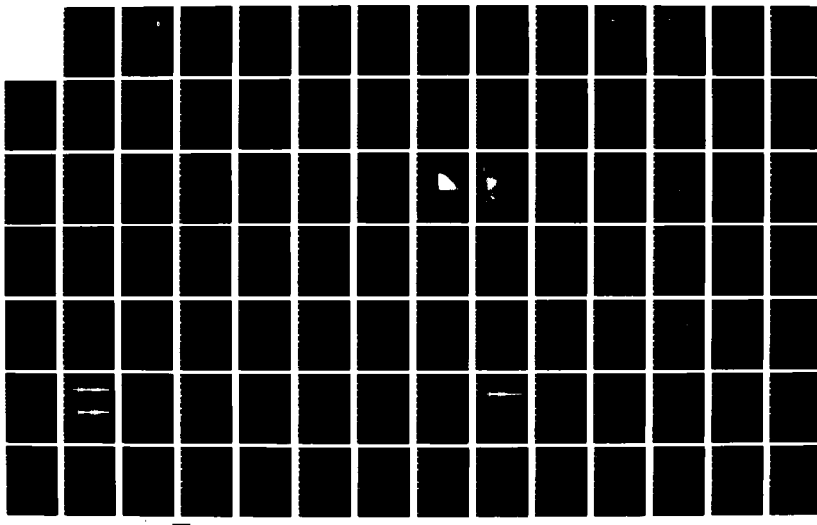
AD-A171 744

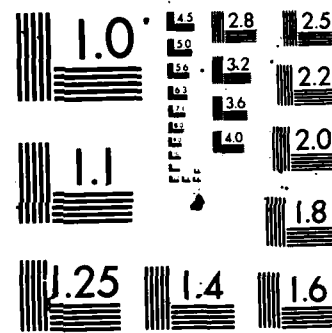
EVALUATION OF THE PERFORMANCE DURING THE GSE TECHNICAL
TEST(U) SCIENCE APPLICATIONS INTERNATIONAL CORP
ARLINGTON VA A CAMPANELLA ET AL JUL 86 SAIC-86/1114
UNCLASSIFIED MDA983-84-C-0028

1/2

F/G 17/18

NL





MICROCOPY RESOLUTION TEST CHART
NATIONAL BUREAU OF STANDARDS-1963-A

AD-A171 744

Technical Report C86-06
July 1986

1
S DTIC
SELECTED
SEP 08 1986
D
FD

TECHNICAL REPORT FOR THE PERIOD
1 JANUARY - 30 JUNE 1986

Center Staff

FILE COPY

DISTRIBUTION STATEMENT A
Approved for public release;
Distribution Unlimited

SPONSORED BY:
DEFENSE ADVANCED RESEARCH PROJECTS AGENCY

Center for Seismic Studies
1300 N. 17th Street, Suite 1450
Arlington, Virginia 22209-3871
Telephone: (703) 276-7900

86 9 08 100

Technical Report C86-06
July 1986

TECHNICAL REPORT FOR THE PERIOD
1 JANUARY – 30 JUNE 1986

Center Staff

The views and conclusions contained in this document are those of the authors and should not be interpreted as representing the official policies, either expressed or implied, of the Defense Advanced Research Projects Agency or the U.S. Government.

Sponsored by:
DEFENSE ADVANCED RESEARCH PROJECTS AGENCY
Monitored by:
Defense Supply Service – Washington
Under Contract No. MDA 903-84-C-0020

Science Applications International Corp.
1735 Jefferson Davis Highway, Suite 907
Arlington, VA 22202

Unclassified

SECURITY CLASSIFICATION OF THIS PAGE

REPORT

AD-A171 744

Form Approved
OMB No 0704-0188
Exp Date Jun 30 1986

1a REPORT SECURITY CLASSIFICATION Unclassified			1b DOWNGRADING		
2a SECURITY CLASSIFICATION AUTHORITY			3 DISTRIBUTION/AVAILABILITY OF REPORT		
2b DECLASSIFICATION/DOWNGRADING SCHEDULE			Unlimited		
4 PERFORMING ORGANIZATION REPORT NUMBER(S) SAIC-86/1114 Technical Report C86-06			5 MONITORING ORGANIZATION REPORT NUMBER(S)		
6a NAME OF PERFORMING ORGANIZATION Science Applications International Corporation		6b OFFICE SYMBOL (If applicable)	7a NAME OF MONITORING ORGANIZATION Defense Supply Service - Washington		
6c ADDRESS (City, State, and ZIP Code) 1735 S. Jefferson Davis Hwy., Suite 907 Arlington, Virginia 22202			7b ADDRESS (City, State, and ZIP Code) Room 1D245, The Pentagon Washington, D.C. 20310		
8a NAME OF FUNDING/SPONSORING ORGANIZATION Defense Advanced Research Projects Agency		8b OFFICE SYMBOL (If applicable)	9 PROCUREMENT INSTRUMENT IDENTIFICATION NUMBER MDA-84-C-0020		
8c ADDRESS (City, State, and ZIP Code) 1400 Wilson Boulevard Arlington, Virginia 22209			10 SOURCE OF FUNDING NUMBERS		
			PROGRAM ELEMENT NO	PROJECT NO	TASK NO
			A04882		WORK UNIT ACCESSION NO
11 TITLE (Include Security Classification) Technical Report for the Period 1 January - 30 June 1986 (Unclassified)					
12 PERSONAL AUTHOR(S) A. Campanella, H. Israelsson, A. Jurkevics, P. Dysart, J. Pulli, C. Romney					
13a TYPE OF REPORT Technical Report		13b TIME COVERED FROM 1/1 TO 6/30/86		14 DATE OF REPORT (Year, Month, Day) 1986 July	
15 PAGE COUNT 135					
16 SUPPLEMENTARY NOTATION					
17 COSATI CODES			18 SUBJECT TERMS (Continue on reverse if necessary and identify by block number)		
FIELD	GROUP	SUB-GROUP	Seismology Nuclear Monitoring Research		
			GSETT Polarization Filtering		
			Seismic Analysis Seismic Network Capability		
19 ABSTRACT (Continue on reverse if necessary and identify by block number) Continuing evaluations of the Center's performance during the GSE Technical Test led to improvements in the automatic association program and verified that the automatic signal detector flagged all expected seismic P-waves. Research on methods for the analysis of seismic data resulted in demonstration of promising methods for identifying pP by polarization filtering and a correlation method. Polarization filtering was applied to two events near the Aral Sea and helped determine that complications in the signals at NORESS were not due to a multiple explosive source. Another investigation of regional events recorded at NORESS revealed spectral differences that could be used to discriminate between earthquakes and explosions in a limited source region. Network capability studies demonstrated agreement between SNAP/D estimates and results from a network in the Baykal region, as well as possible effects of source radiation patterns on station detection thresholds. Analysis of explosion generated and synthetic waveforms showed that waveform periods and shapes can be used to constrain estimates of t*, and illustrated the strong dependence of t* estimates on assumptions about near-source conditions.					
20 DISTRIBUTION/AVAILABILITY OF ABSTRACT <input checked="" type="checkbox"/> UNCLASSIFIED/UNLIMITED <input type="checkbox"/> SAME AS RPT <input type="checkbox"/> DTIC USERS			21 ABSTRACT SECURITY CLASSIFICATION Unclassified		
22a NAME OF RESPONSIBLE INDIVIDUAL Ann U. Kerr			22b TELEPHONE (Include Area Code) (202) 694-3145		22c OFFICE SYMBOL DSO/GSD

Table of Contents

1. EVALUATION OF THE GSE TECHNICAL TEST	1-1
1.1. Performance of the RSTN Signal Detector During the GSE Technical Test (GSETT)	1-1
1.2. A Note on Computational Experiments with Automatic Association of GSETT Data	1-14
2. RESEARCH TO IMPROVE ANALYSIS OF SEISMIC DATA	2-1
2.1. Use of Polarization Filtering to Enhance Depth Phases in P-Coda	2-1
2.2. Correlation of P-Coda to Detect Depth Phases, Applications of RSTN Data	2-10
2.3. Application of Polarization Processing to NORESS and RSTN Recordings of Two Events in West Kazakh, S.S.R.	2-21
2.4. Expanded Use of Computers in Regional Seismic Data Analysis	2-29
3. NETWORK CAPABILITY AND DESIGN	3-1
3.1. A Note on Earthquake Detectability: Radiation Pattern Effects	3-1
3.2. A Note on Earthquake Detectability: A Comparison Between a Local and a Global Network	3-14
4. YIELD ESTIMATION	4-1
4.1. Sensitivity of mb to Earth Attenuation	4-1



Accesion For	
NTIS	CRA&I <input checked="" type="checkbox"/>
DTIC	TAB <input type="checkbox"/>
U: announced	<input type="checkbox"/>
Justification	
By	
Distribution /	
Availability Codes	
Dist	Avail and/or Special
A-1	

1. EVALUATION OF THE GSE TECHNICAL TEST

1.1. PERFORMANCE OF THE RSTN SIGNAL DETECTOR DURING THE GSE TECHNICAL TEST (GSETT)

During the GSETT, the Center for Seismic Studies, in its capacity as a "National Data Center" analyzed signals recorded by three RSTN stations: RSNY, RSON, and RSSD. Characteristics of RSTN station detection capabilities can yield important information concerning station biases and effectiveness of the signal detector. Detections are based on a change in the power level of the recorded signal. Acceptance is based on the quality of the detection.

The signal detector was designed to recognize, mark and characterize the onset of seismic waves. The criterion for "recognition" was a specified increase in the power level of the signal. The detection algorithm is based on the "Z" statistic of Snell and Swindell (1977), which is designed to adapt to gradual variations in the ground noise level. The algorithm computes the ratio of the average power over two seconds of recording to the average power over the preceding 60 seconds. This power ratio is normalized by a continuously updated computation of the variance of the power ratio to form the "Z" statistic. Normalization by the variance of the power ratio tends to stabilize the detector and produce a more uniform rate of false alarm. (US/GSE/37, Appendix II.)

A potential signal is declared to be detected when the normalized power ratio exceeds a specified detection threshold; in this instance a detection threshold of four standard deviations from the mean. The power ratio is improved by preprocessing the data using a time domain bandpass filter (to enhance the signal-to-noise ratio). A bandpass prefilter of 0.7 - 4 Hz was used initially. Two weeks into the technical test, the passband prefilter parameters were changed to 0.9 - 4 Hz, due to an excessive percentage of false alarms (detections on high levels of noise). (US/GSE/37, Appendix II.) In what follows, potential signals flagged by the automatic event detector will be called "detections;" those established to be valid seismic event phases by an analyst will be called "signals."

An interactive system ("Graphic Parameter Measurement," or gpm) was developed by Science Horizons, Inc., for use on a SUN micro-computer. During the technical test, the system was used primarily to review "detections," eliminate false alarms, refine computer generated parameters, identify seismic phases, and extract additional parameters from the valid seismic signals. Table I shows the percentage of signals accepted and rejected.

TABLE I

	Total detections	% accepted in analysis	% rejected in analysis
RSNY	1269	36.09	63.91
RSON	1993	65.93	34.07
RSSD	3238	40.83	59.17
Total	6500	42.60	52.40

Of the total signals accepted in analysis, 76.36% (704 events) concurred with NEIS events and 23.64% (218 events) did not. The numbers of events detected by each station is a function of the magnitude of the events occurring during the GSETT and of the individual station detection threshold. The magnitude threshold for participating RSTN stations was found in the standard way, as the point where a log-linear plot of the cumulative numbers of events versus magnitude departs from a straight line (*Figure 1*). These thresholds correspond in a general way with observed noise levels at each station.

Two databases were compared, the first (database A) containing all the RSTN detections flagged by the Center detector; the second (database B), a list of expected arrival times from valid NEIS events recorded during the technical test. A detection was initially considered "valid" if the NEIS and computed RSTN arrival times agreed to within 20 seconds. The resulting list of detections (database C) that met this criteria were then compared with a third (database D) containing detections that were rejected by the analyst during the technical test. List E, rejected but apparently valid detections, is comprised of 152 signals that matched up when comparing lists C and D (*Figure 2*). Rejected but apparently valid detections were reanalyzed and grouped into four categories, illustrated by examples in *Figures 3-6*:

- Category 1. Erroneous rejection - 12 signals (*Figure 3*). These were only rejected signals that were subsequently confirmed to be truly valid based on a reanalysis of the recorded waveform.
- Category 2. Questionable signal (below quality reporting level) - 76 detections (*Figure 4*).
- Category 3. Interference (spikes, possible signals masked by another clear signal at predicted time or event clearly at wrong distance to be that reported by NEIS) - ten detections (*Figure 5*).
- Category 4. Noise (no measurable signal) - 54 detections (*Figure 6*).

Categories 3 and 4 clearly comprise power level changes not related to the NEIS reported events that triggered the automatic detector, but were properly rejected by the analyst. Category 2 contains power level changes that could be valid detections, but the analyst was unable to measure a useful arrival time, or amplitude, or both. Category 1 contains signals that were initially rejected by accident, or upon more careful study, were elevated from Category 2 to Category 1. Only events with magnitudes given by NEIS will be analyzed (*Figure 7*).

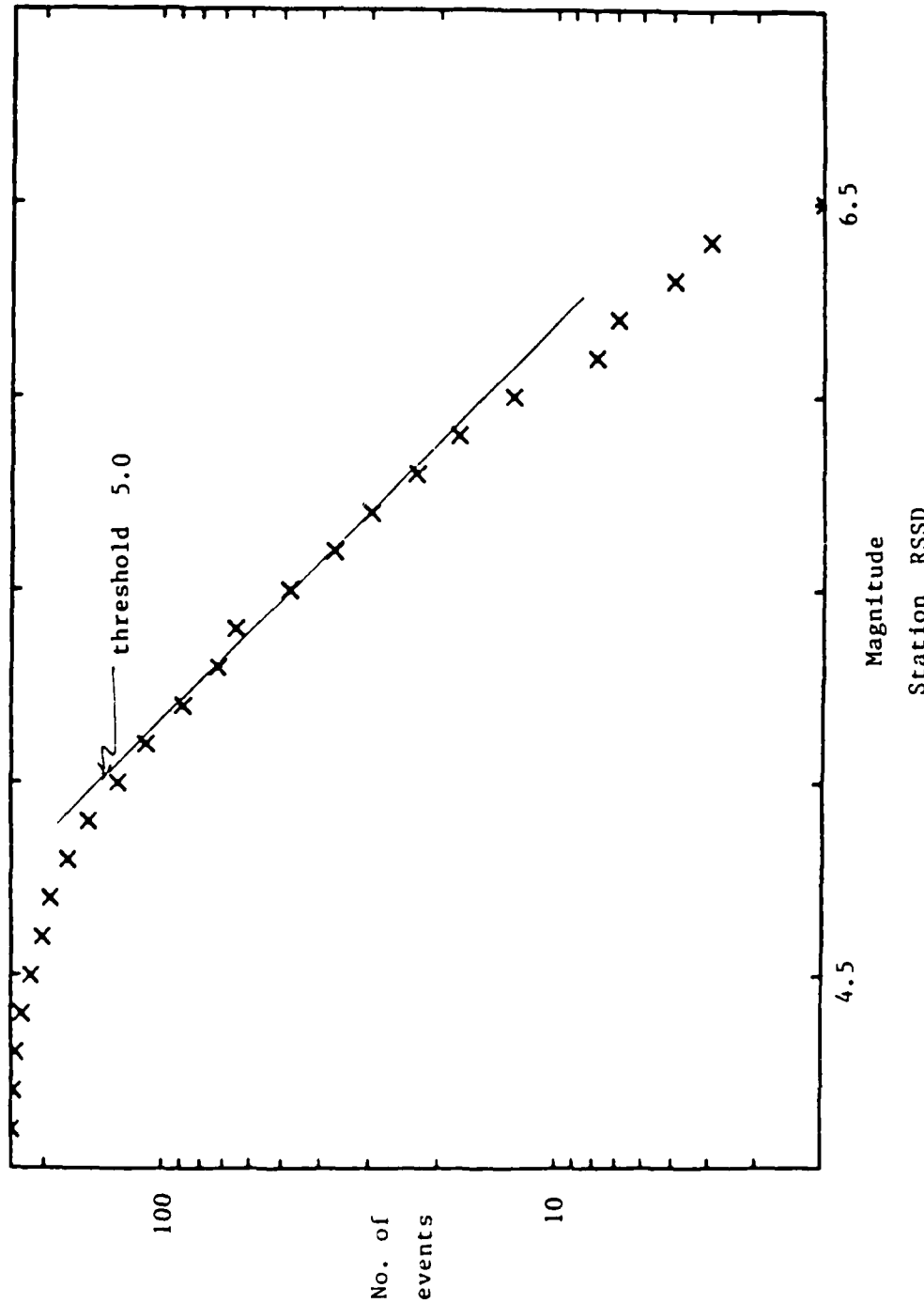


Figure 1. Magnitude threshold for participating RSTN station (RSSD).

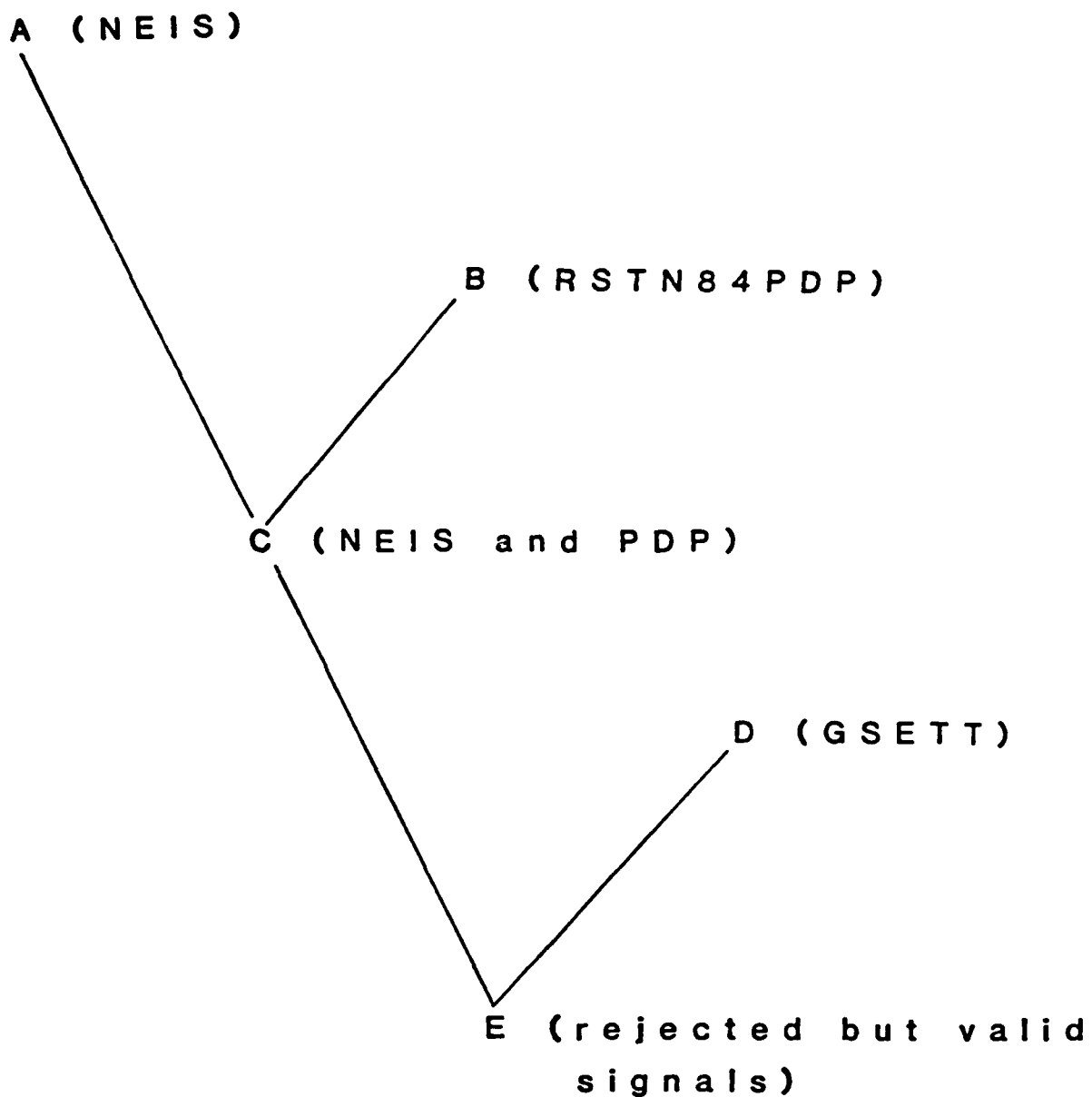


Figure 2. Schematic diagram of database comparisons.

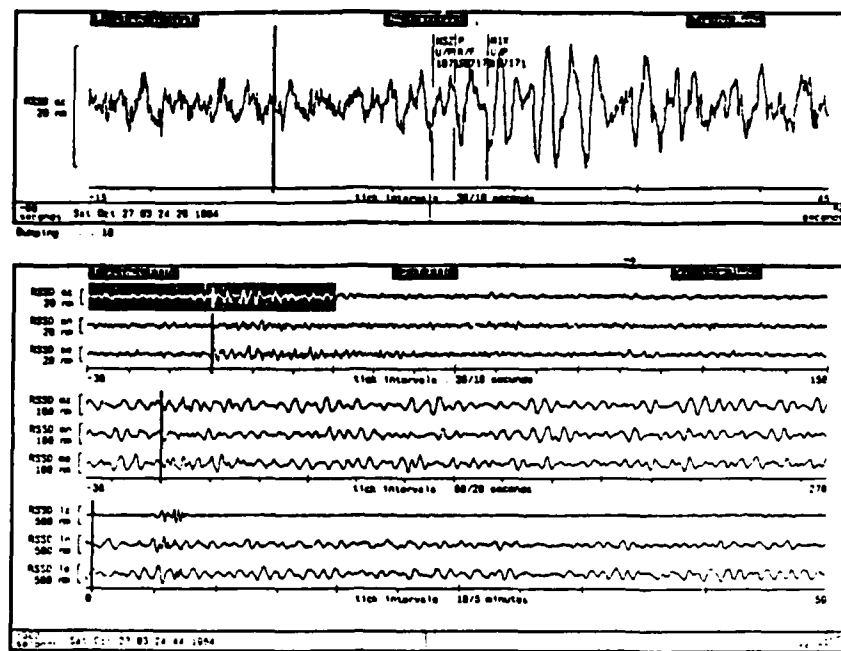


Figure 3. Erroneously rejected signal lat. 43.98° , long. -127.84° ; depth 10 km; mb 4.1; dist. 17.11°.

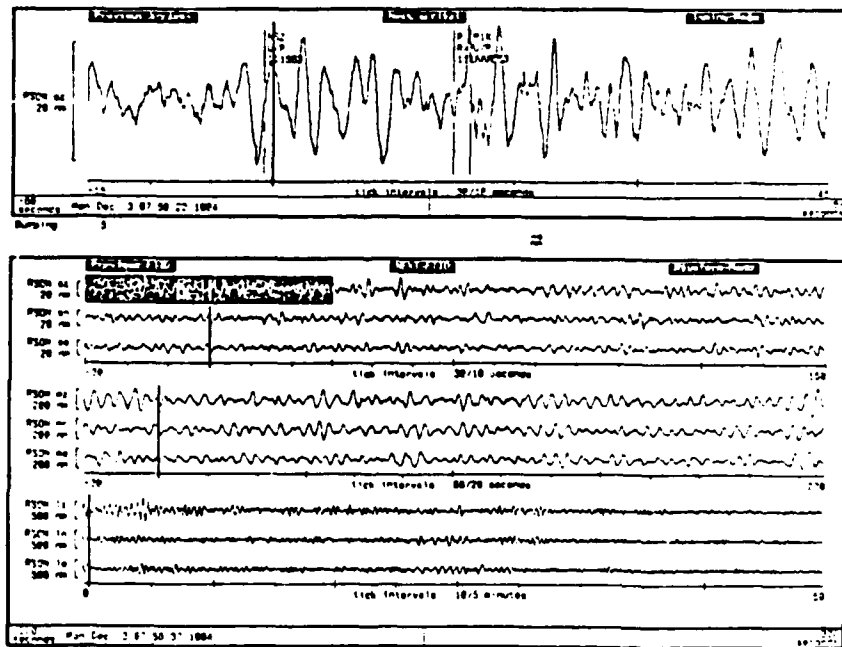


Figure 4. Questionable signal (below quality reporting level) lat. 37.97° , long. 43.15° ; depth 36 km; mb 4.7; dist. 83.77°.

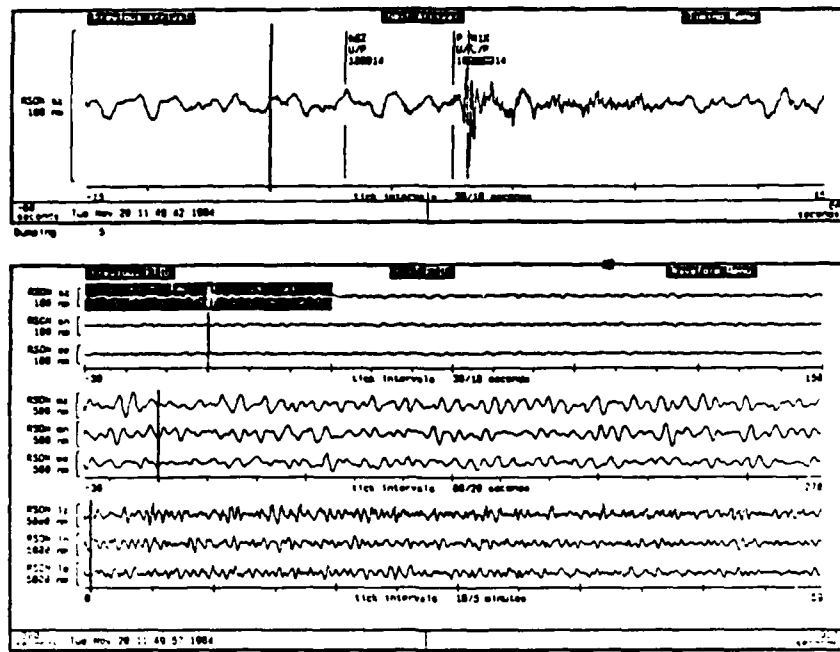


Figure 5. Interference (teleseism obscured by local) lat. 5.17° , long. 125.29° ; depth 212 km; mb 5.2; dist. 114.92° .

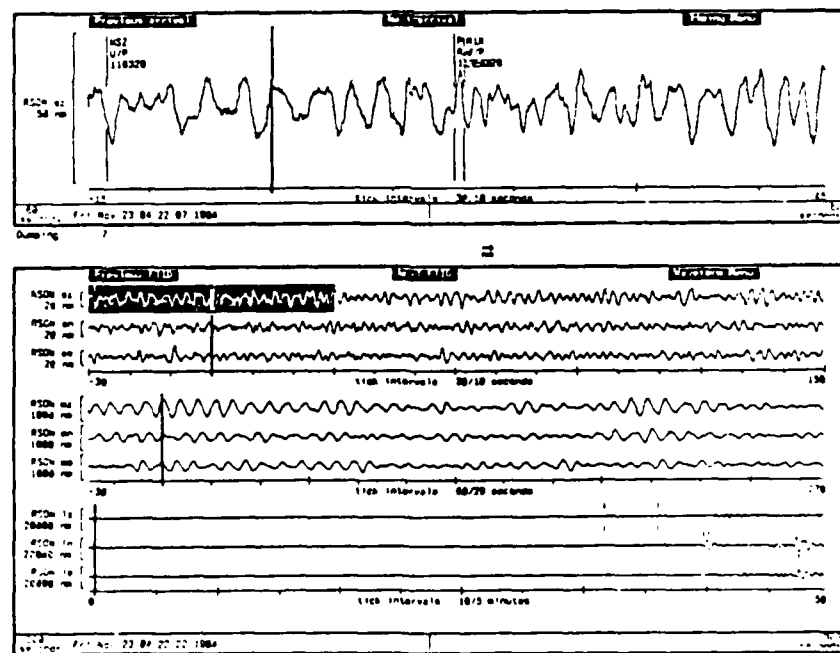


Figure 6. Noise (no reasonable signal) lat. 2.89° , long. -95.14° ; depth 10 km; mb 4.6; dist. 47.81° .

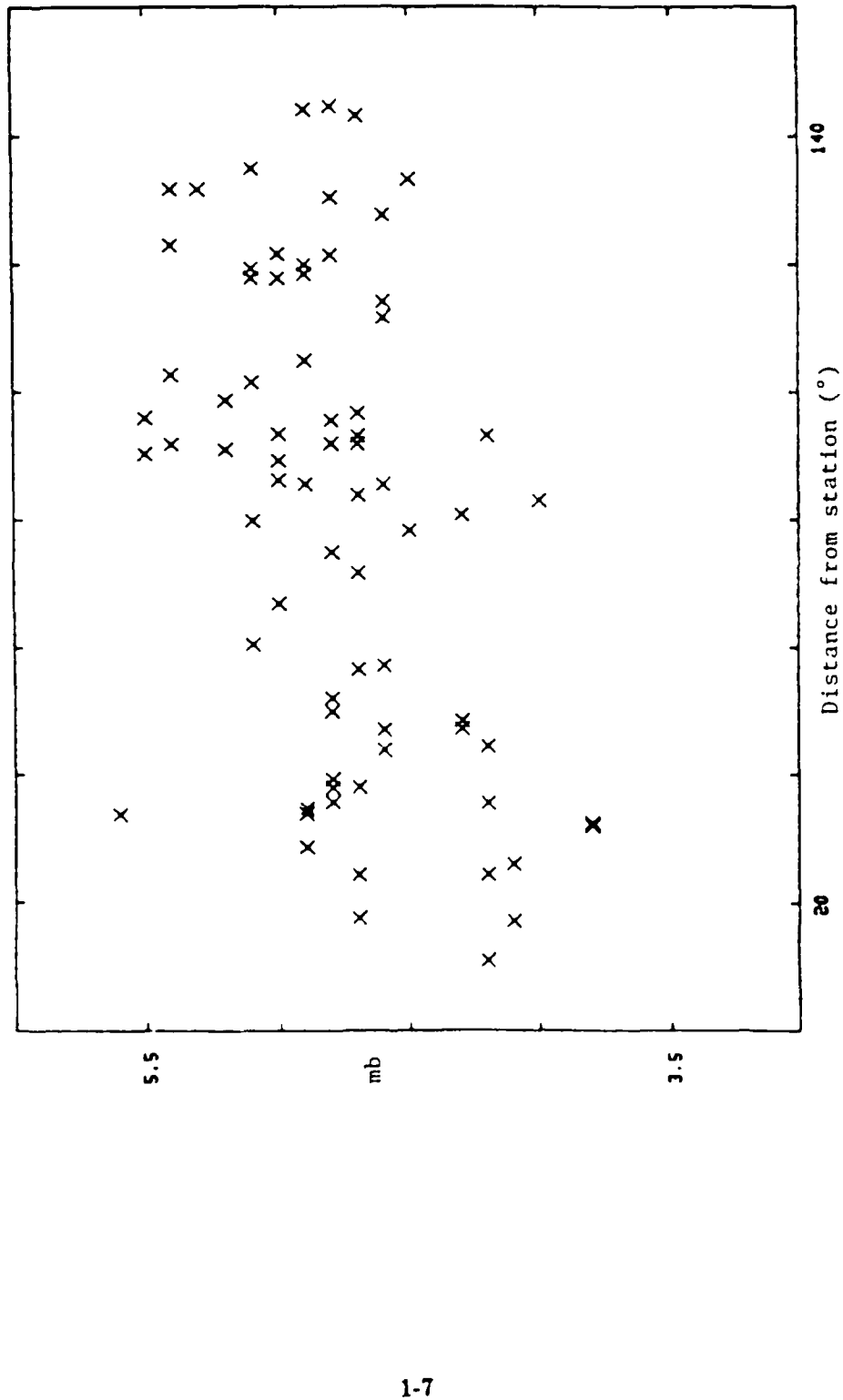


Figure 7. Valid signals rejected during GSE Technical Test. Participating RSTN stations (RSNY, RSNO, RSSD) with defined NEIS magnitudes.

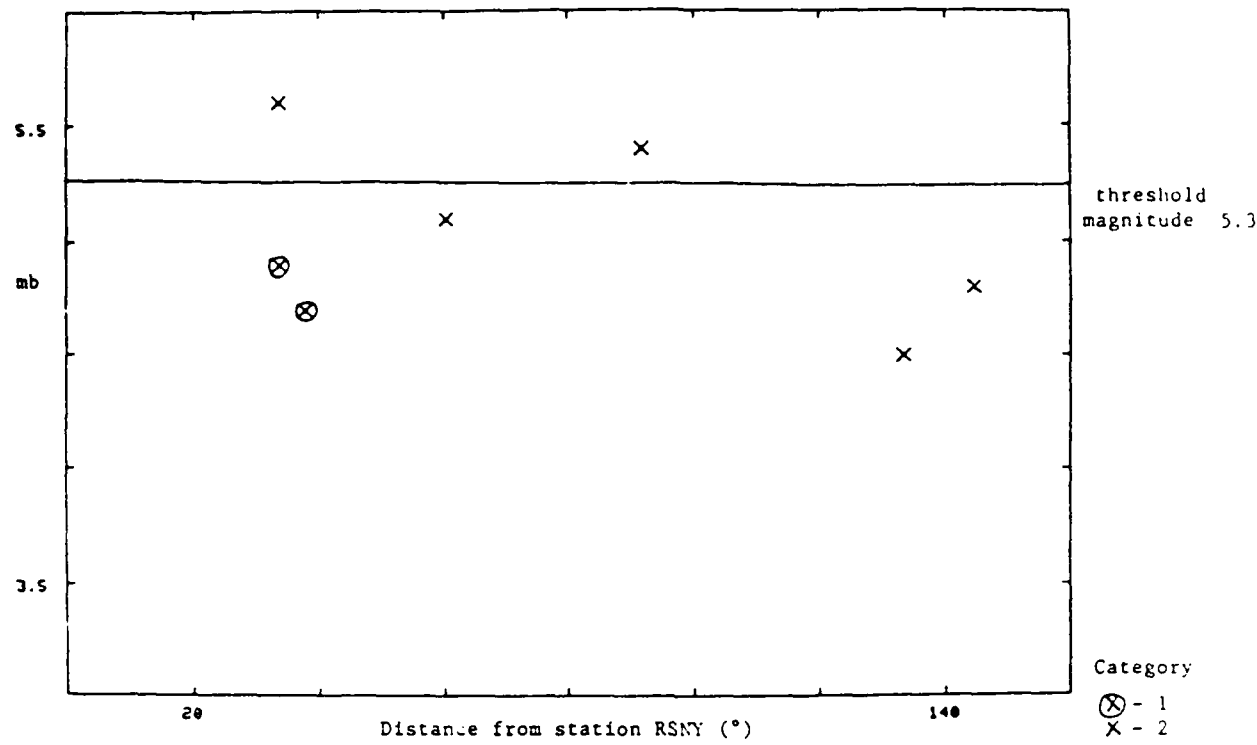


Figure 8. Valid signals rejected during GSE Technical Test for station RSNY.

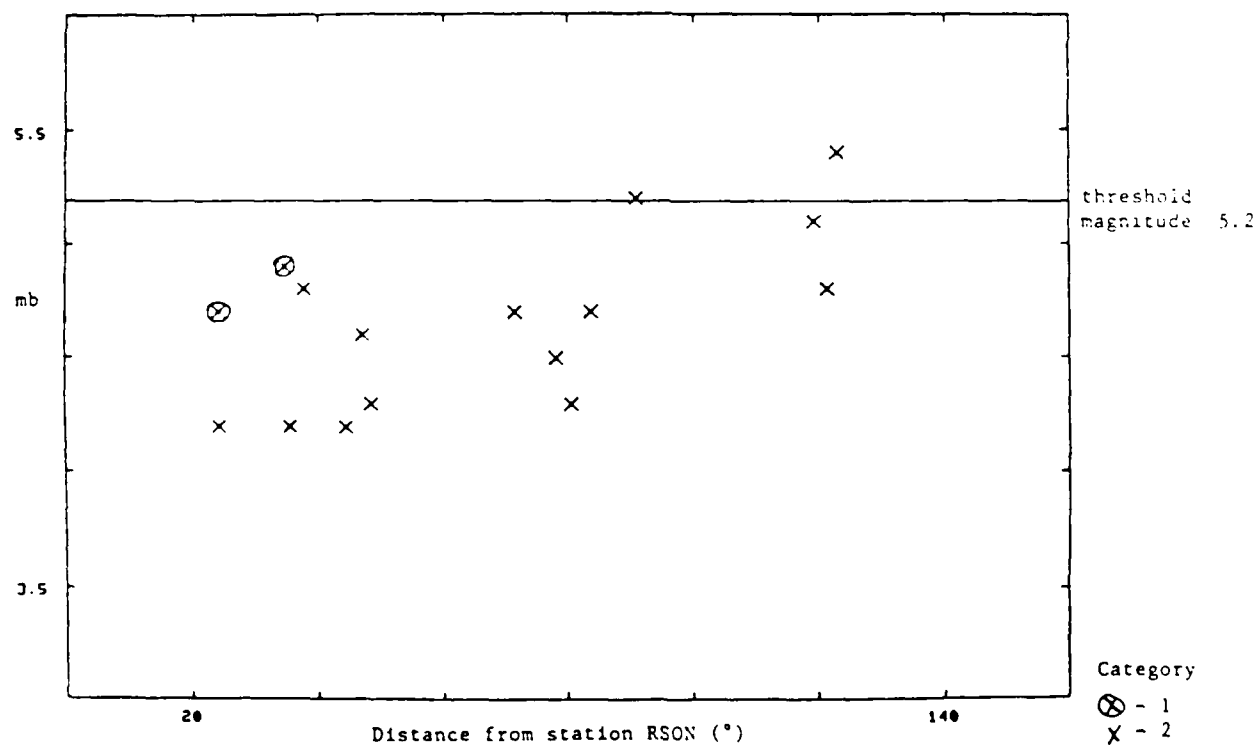


Figure 9. Valid signals rejected during GSE Technical Test for station RSON.

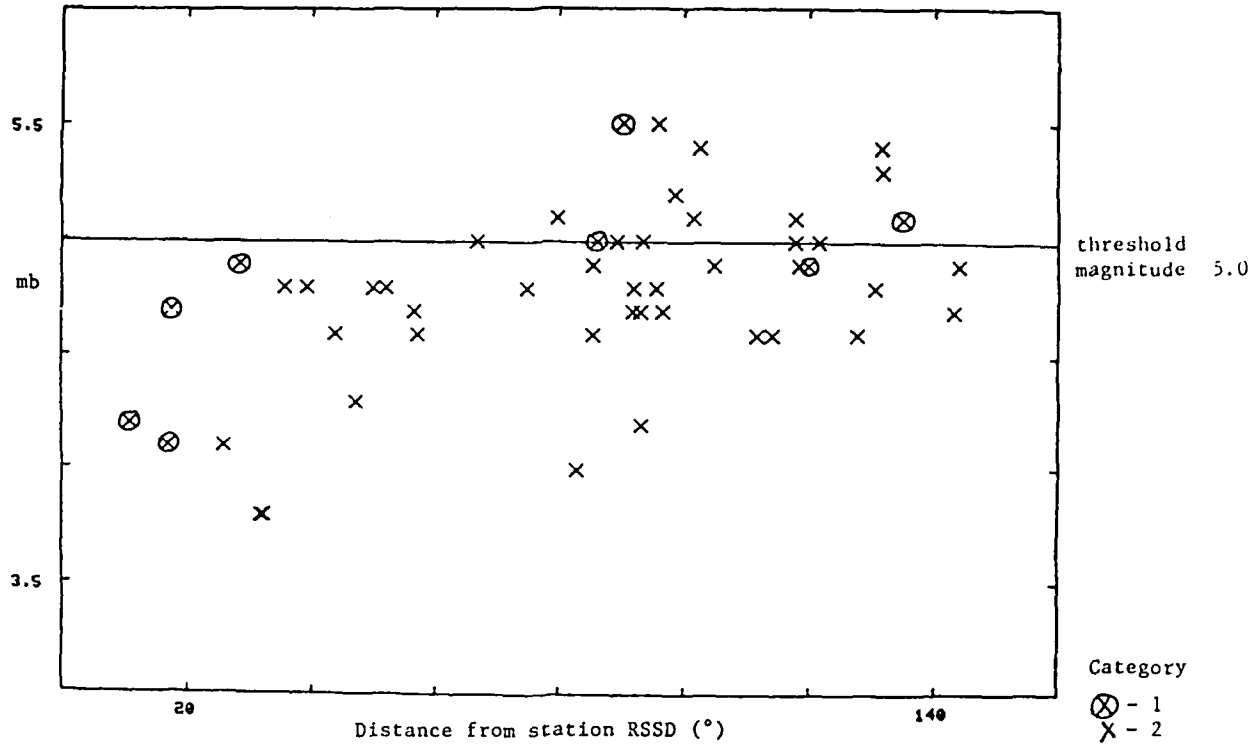


Figure 10. Valid signals rejected during GSE Technical Test for station RSSD.

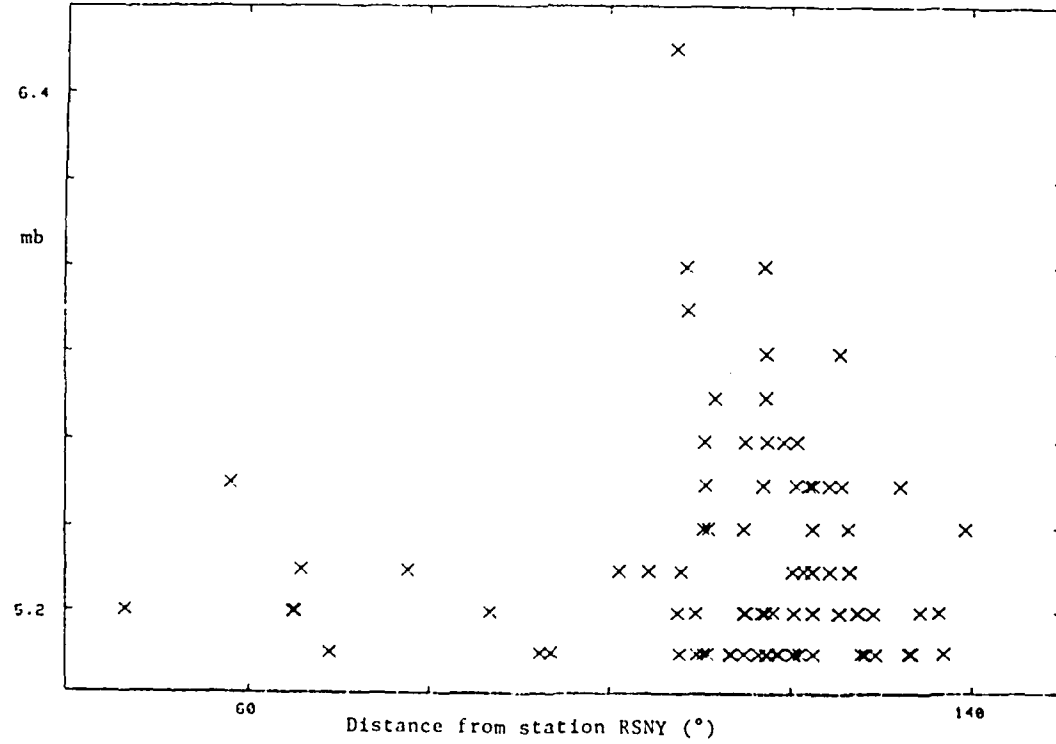


Figure 11. Predicted signals not detected during GSE Technical Test for station RSNY.

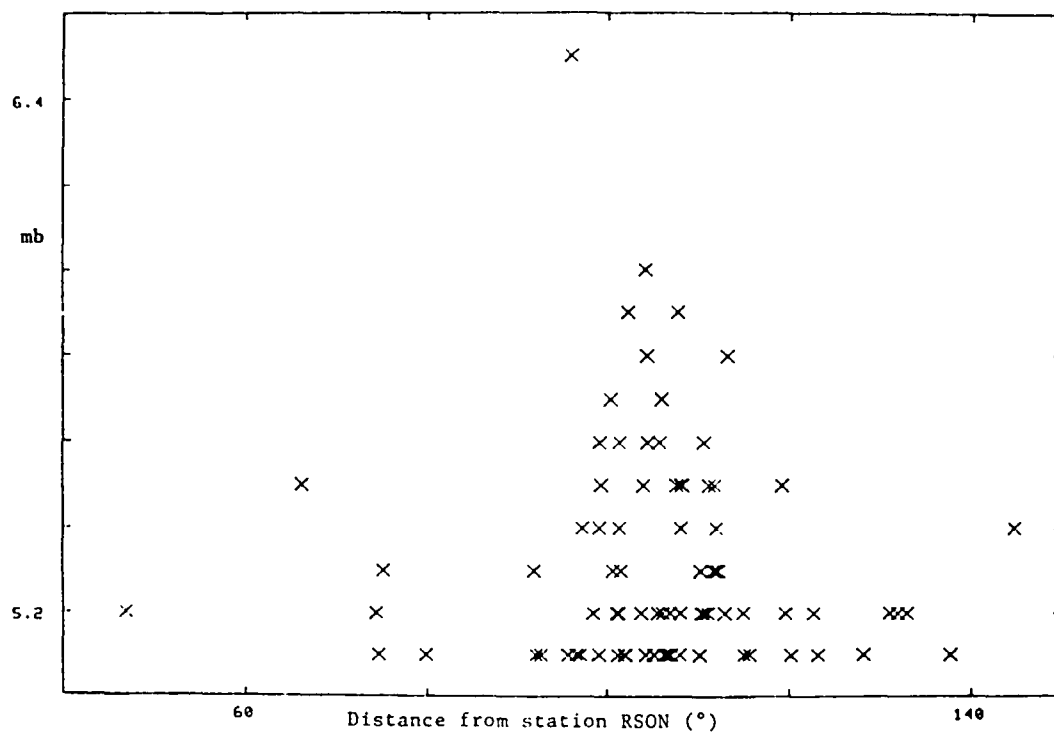


Figure 12. Predicted signals not detected during GSE Technical Test for station RSON.

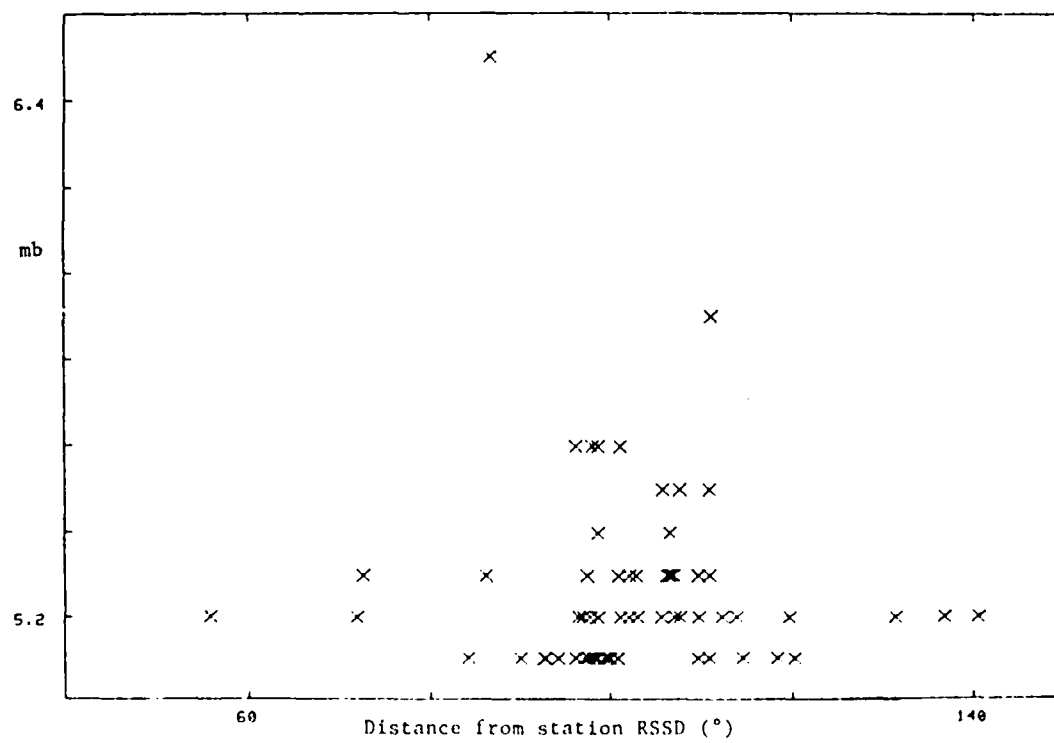


Figure 13. Predicted signals not detected during GSE Technical Test for station RSSD.

Station RSNY has very few Category 1 erroneous rejections (Table II, *Figure 8*). The two erroneously rejected events are below the station's magnitude threshold of 5.3 and have a signal-to-noise ratio of approximately 2.5. These two events appeared to the analyst to be emergent Lg phases. *Figure 8* indicates that there are two events with questionable signals that have magnitudes above the threshold. RSNY recordings of events in the distance range 35° to 90° may have had low signal-to-noise ratio. About two-thirds of the confirmed or questionable detections were at distances between 16° and 103°. Those corresponding to shadow zone and larger distances comprised a third of the rejected detections. Magnitudes of events corresponding to these rejected but valid events ranged from 4.4 to 5.6.

TABLE II

	RSTN Station	Category			
		1	2	3	4
No Magnitude Reported by NEIS	RSNY	0	1	1	5
	RSON	0	3	1	4
	RSSD	0	10	3	5
Magnitude Given by NEIS	RSNY	2	5	0	5
	RSON	2	14	4	12
	RSSD	8	43	1	23

RSON has a magnitude threshold of about 5.2. *Figure 9* shows that all but one confirmed or questionable detection rejected by the analyst falls below this threshold. Two events were erroneously rejected at distances of 24° and 35°, with magnitudes of 4.7 and 4.9, respectively. The signal-to-noise ratio for these events is low, roughly 2.5. As distance increases, so does magnitude. Three-fourths of the rejected signals were for events in the distance range of 16° - 103°. The remaining 25% were at distances larger than 103°. Magnitudes of these rejected events range from 4.2 to 5.4, while the magnitude threshold for RSON is 5.2.

Rejected but valid events for station RSSD exhibit a behavior of lower magnitudes at closer distances (*Figure 10*). Five events were erroneously rejected. Magnitudes of these events fell below the magnitude threshold of 5.0 except detections arriving from 90° and 135°. Again, the signal-to-noise ratio for these events is low, around three. A large number of rejected but valid detections were in the 80° to 90° range, at varying magnitudes. 71% of the rejected but valid detections recorded on RSSD were for distances of 16° - 103° from the station. One event with a magnitude of 4.2 had a distance of 10°. 28% of the rejected detections corresponded to event distance larger than 103°. Magnitudes ranged from 3.8 to 5.5. Magnitude threshold for RSSD is 5.0.

A total of 94 events of magnitude greater than 5.0 that were reported by NEIS did not trigger the automatic detector. After reviewing the predicted time these signals were to arrive, several aspects became evident. Approximately 10% of these signals arrived during data dropouts on the short period vertical (SPZ) channel. This was the only channel on which the power level detector was run. The remaining events were not evident on the SPZ channel. 4% of the events occurred at distances of less than 85° from the respective RSTN stations (*Figures 11-19*). The remaining 96% were at distances greater than 85°. The short period signal may not have had power within the specified passband. Several of the events that were not evident on the short period channels were evident on the long period channels, especially at core shadow distances. It was also possible that the event did not have a long enough duration on the short period. One event was not detected because it was in the coda of another event, so the detector did not have time to reset.

Results from this study show that the Center ran a very sensitive power level detector during the GSE Technical Test of 1984. Over 50% of the detections were rejected, most of which were false alarms. Signals reported by NEIS and not detected automatically were not evident on the short period channel predominantly due to the distance between the epicenter and the station.

Automatically detected, but erroneously rejected, signals (Category 1) were 0.19% of the total detections. One station (RSSD) had the largest number of signals that fell into this category. The signal-to-noise ratio of these events was greatest at this station but so was the number of detections and the chance that an event could be misinterpreted.

Antoinette Campanella

REFERENCES:

Swindell, W. H. and Snell, N. S., 1977. "Station Processor Automatic Signal Detection System. Phase 1: Final Report, Station Processor Software Development," *Texas Instruments Report No. ALEX(01)-FR-77-01*, AFTAC Contract No. F08606-76-C-0025, Texas Instruments, Incorporated, Dallas, Texas.

1.2. A NOTE ON COMPUTATIONAL EXPERIMENTS WITH AUTOMATIC ASSOCIATION OF GSETT DATA

1.2.1. Introduction

A computer program for automatic association and location of seismic events (AA) based on the general principles of seismic event association established in the GSE reports, was used at the EIDC in Washington during the GSETT.

This note summarizes results from some computational experiments that were carried out in the light of experience gained in operating the program during the GSETT. Apart from association of short-period arrival times and location of seismic events, these experiments also included association of surface waves, a function that was not tested during the GSETT at the EIDC in Washington. Attempts were made to improve the performance of the event association by tuning the values of some of the computational parameters that drive this AA-program. Moreover, an extended input data base of station arrival times was used in the computations.

1.2.2. Comparison Between EIDC Versions

Event bulletins produced at the EIDC's during the GSETT show differences, which have been attributed to differences in input data, in computer programs, and in computers.

Computers and programs used at the EIDCs in Stockholm and Washington were, however, quite similar. The two programs were independently installed from an original IBM main frame version into a VAX/750 (under VMS) and a VAX/780 (under Unix), respectively. Slightly different library routines were used for the part of the AA-program that check the amplitude consistency (both NAG and IMSL routines were used at Stockholm and only IMSL routines were used at Washington). Some of the computational parameters for the amplitude consistency check procedure were also different. These differences consisted in noise amplitudes for some of the GSETT stations, and in minimum plausibility values for acceptance of events and of station detections. (SMEVS= -3.0 and -9.9, SMSTS= 0.01 and 0.00 for Stockholm and Washington, respectively). Moreover, slowness values and azimuths reported by array stations were used only at Washington for event locations.

Differences in input data consisted of differences of actually received seismological messages, differences in stations used, and different parsing programs that translate the seismological messages into arrival data input files for the AA-programs.

Because of the difficulty in determining to what extent the differences in the EIDC event bulletins were due to differences in input data, in association programs or in computers, suggestions have been made for comparative computational experiments, in which the same input data is processed with the same program but on different computers.

Such a test was carried out with the version of the AA-program described in the GSE working paper GSE/SG5/8 (A Program for Automatic Association of Seismic Events). A copy of this program, originally installed to run on a VAX/750 (under VMS), was implemented on the VAX/780 at the Center for Seismic Studies. This implemented version at the Center differs from the one used at Center during the GSETT, which was installed from an IBM main frame version. This "VAX/750" implemented version was run on a test example provided with the program itself. This example covers 11 days of data (November 1-11, 1981) and the solution as provided on a log file includes 45 events. The processed results at the Center gave exactly the same numbers of events and only in two instances could differences in event source parameters be noted. For one event there was a difference in origin time of 0.1s, and for another event a depth difference of 1 km (486 and 487 km, respectively) was obtained.

1.2.3. Computer Runs

The AA-program described in the GSE working paper GSE/SG5/8 is driven by a number of computational parameters, the values of which have to be set by the user. A set of standard values were listed in the GSE/SG5/8, and these were largely used during the GSETT.

The computational experiments here consisted mainly of runs with various parameter settings and in some instances changes were also made in the code itself, however, without changing the logics or basic algorithms of the AA procedure. The most significant changes are summarized below.

- Deviations of Slowness Residuals

As the AA-program iterates in the epicenter location process it removes observations (arrival times and slowness vectors) with residuals 1.5 times greater than assumed *a priori* standard deviations, and for events based on a small number of defining observations the event itself may be rejected when such observations are truncated. For example, it was noticed during the GSETT that a small presumed explosion (October 18, 1984, in Eastern Kazakh) would have been rejected in this way, since the residual of the slowness vector (difference between observed and calculated, S_{obs} , and S_{calc} -values) reported by one array was too large, i.e.,

$$|S_{obs} - S_{calc}| \geq 1.5\sigma$$

In the list of standard values in GSE/SG5/8 the *a priori* standard deviation for array slowness, σ , is assumed to be 1.5 and 3.0 for epicentral distances greater than and smaller than 25 degrees, respectively. The error in slowness determinations vary from array to array and depend partly on array aperture and to what extent corrections are applied. It would, therefore, be appropriate to have *a priori* standard deviations that depend

on the particular array, rather than one single value for all array stations of a network. For the computational experiments here a large value of σ for the slowness vector was used (5.0) in order to accommodate large errors.

- **Event and Station Plausibilities**

For a given processed event, the amplitude consistency check procedure is carried out in two steps: (1) individual station plausibilities and, (2) total event plausibility (Elvers, 1980). The station plausibility is defined as the probability that the station detects the event with the estimated magnitude at the estimated epicenter. Possible values for the station plausibility thus range between 0.0 to 1.0. The individual station plausibilities are compared with a minimum acceptable value (0.01) and stations with values below this value are automatically removed. The event plausibility is defined in a more complicated way (Elvers, 1980) and is designed to show if the pattern of detections, non-detections, and recorded station amplitudes is likely or if the event is spurious. The value of the event plausibility is not on a probability scale, but can be any real number. Large negative values indicate spuriousness, and an event with a total plausibility below a certain minimum is automatically rejected. This minimum value was increased during the re-runs from -9.9 used during the GSETT to -3.5, which is equal to the value suggested in GSE/SG5/8.

- **Amplitude Attenuation Curve**

Measured signal amplitudes and station noise amplitudes are compared with amplitudes calculated from the magnitude formula in the amplitude consistency check. The standard amplitude attenuation curve in the program uses a constant correction for distances beyond 100 degrees (equal the value at 90 degrees). This constant value was replaced in some of the calculations here with the so called NORSTAR curve beyond 100 degrees. This curve is similar to curves derived from broader set of observations (Blandford, 1973). The value of the standard deviation of the signal amplitudes, σ_s , in this distance range was also reduced from 1.50 to 0.40.

- **Station Noise Amplitudes**

Station noise levels in both the short and long period frequency bands were based on measurements during the GSETT instead of the provisional values compiled prior to the test.

- **Extended Data Base**

The average number of stations for which data were available for the final GSETT bulletin was 48.6 and this number was increased by about ten to 53.8 percent for the re-run experiments discussed here. The additional data was obtained from data collected at the EIDC in Stockholm.

Results from runs with two parameter set ups are summarized in the following sections of this report: (1) standard values with the changes above except for the amplitude attenuation beyond 100 degrees (for the entire period of GSETT, October 15-December 14, 1984); (2) standard values including all changes above (for the reconciliation period only, i.e., December 1-14).

The values of the parameter set as compared to those used during the GSETT differ mainly for parameters that are used in the amplitude consistency check procedure. During the GSETT only provisional station noise amplitudes were available and the parameter values were set to "maximize the probability of defining events", an objective laid down by the GSE for event association and location. This, however, also meant that a fairly large number of spurious events were generated, that had to be rejected by an analyst reviewing the automatically calculated event lists.

1.2.4. Associated and Located Events

As mentioned above the list of events automatically generated by the AA-program has to be reviewed by an analyst in order to reject spurious events. The results of the computer runs here are analyzed with regard to events that had to be rejected. In addition, the computed hypocentral co-ordinates are compared with determinations of the monthly bulletins of the NEIS.

1.2.5. Accepted and Rejected Events

In order to facilitate comparisons between the re-run and the GSETT, the review was carried out in a consistent manner, so that events that were rejected or accepted during the GSETT, were also rejected or accepted for the re-run even if an independent analysis of the events automatically generated during the re-run would have arrived at different conclusions.

The following table summarizes a comparison of numbers accepted and rejected events during the GSETT and the re-runs:

Data -	Period -	No. of events/day		Total No. of Events	
		Accepted	Rejected	Accepted	Rejected
GSETT	Total	15.0	4.3	915	262
Re-run 1	Total	15.6	3.4	952	207
GSETT	Recon	15.6	4.9	218	69
Re-run 1	Recon	15.3	3.2	214	45
Re-run 2	Recon	14.6	2.6	204	36

The period "Recon" in the table refers to the reconciliation period, which covered the last two weeks of the test, December 1-14.

The numbers for accepted events in the table show that there is no significant improvement in capability to define and locate events by using the revised parameters during the re-run.

It is clear, however, that the events accepted during the re-run have larger total event plausibility values than those accepted during the GSETT as shown by the comparison in *Figure 1*. The data in the figure represent plausibility values for events with six or less defining stations. In fact, a significant number of the events accepted during the GSETT did not have values above the minimum plausibility of -3.5 used here.

It is also clear that the numbers of events that had to be rejected is reduced and that this reduction is almost a factor of two for the parameter setting used during "re-run 2," which was applied only for the reconciliation period.

Most of the rejected events fall into four categories: multiple association, split events, inconsistencies between reported and associated arrivals, and poor location control of defining stations. About 75 percent of the rejected events fall in the category of multiple associations.

Figure 2 compares the plausibility values and estimated epicentral errors (as defined below in Section 4.3) of events accepted (upper diagram) and rejected (lower diagram) during the re-run. These estimated errors indicate the location control. Again, only events with six or less defining stations have been included in the diagrams. It is difficult to see any difference between the two types of events and hence the event plausibility or estimated epicentral error does not seem to provide an obvious criterion for rejection. Most of the data points for rejected events, i.e., in the lower diagram of *Figure 2*, represent events with multiple associations. For accepted events it is also difficult to see any correlation between event plausibility and epicentral error, even if the data indicate that events with the largest event plausibility values (greater than -1.0 or so) have relatively small estimated errors (less than one degree or so).

A high value of the minimum acceptable event plausibility reduces the numbers of events that have to be rejected, but it also increases the risk of rejecting real events.

1.2.6. Station Noise and Plausibilities

The association program computes station plausibilities for detecting and non-detecting stations for each event that it defines and locates. As mentioned above, defining stations with plausibilities below a pre-set minimum (0.01) are automatically truncated during the processing. As a test of the internal consistency provided by the revised station noise amplitudes used in the re-run, the distribution of station plausibilities obtained by the AA-program is compared with "theoretical" values computed from the following simple model. Assume that the incremental detection probability, p_j , for station j , as a function of magnitude, m , can be written as:

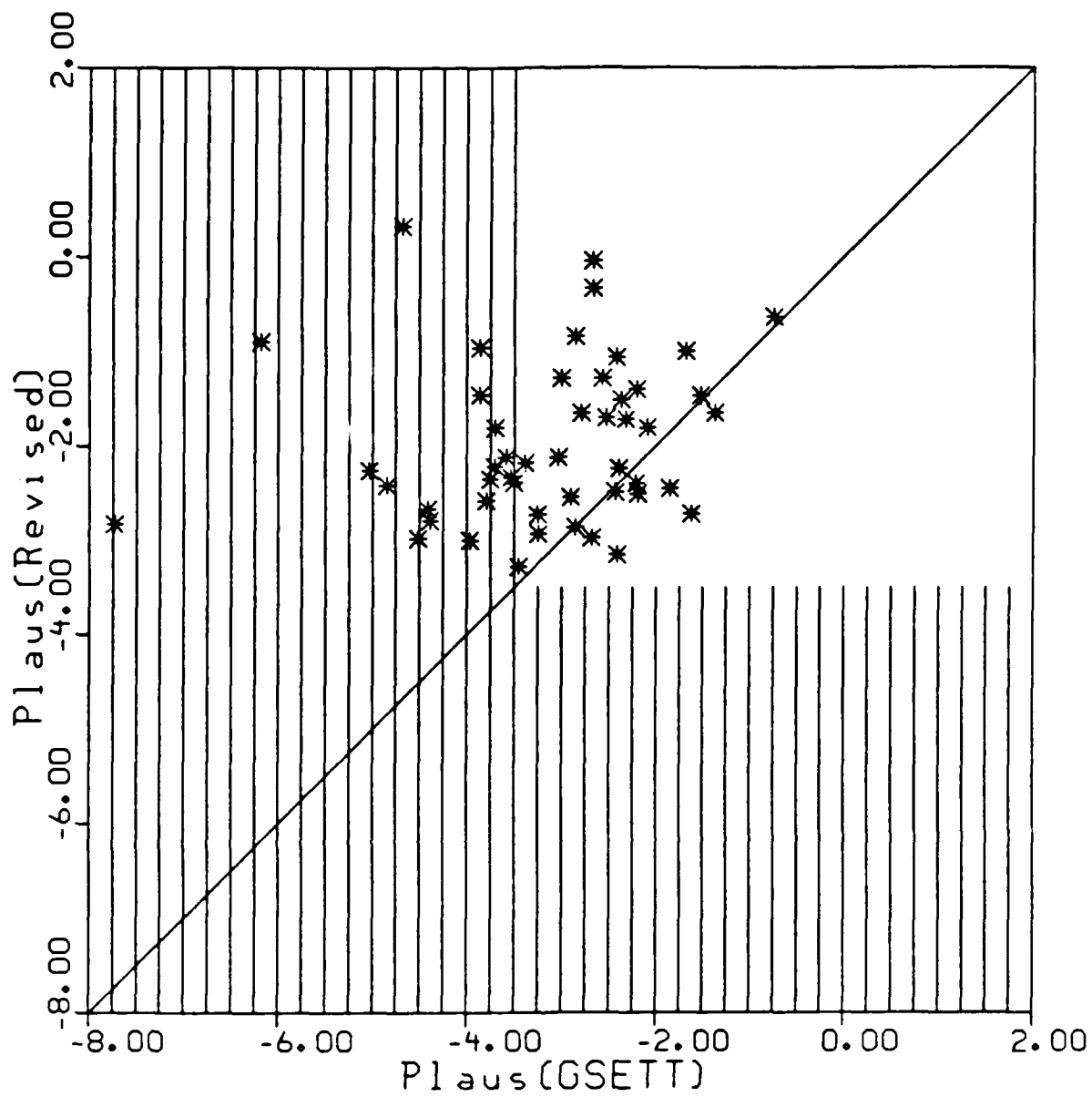


Figure 1. Comparison between event plausibilities obtained during the GSETT and the revised computations here. Revision of computational parameters as described in the text were used in the re-run. The data in the figure cover events with six or less defining stations for the reconciliation period during the GSETT, i.e., December 1-14, 1984. Note that the event plausibility as defined here can take both negative and positive values and that large negative values indicate spuriousness. The straight sloping (at 45 percent) line represents equal plausibility values for the GSETT and the re-run.

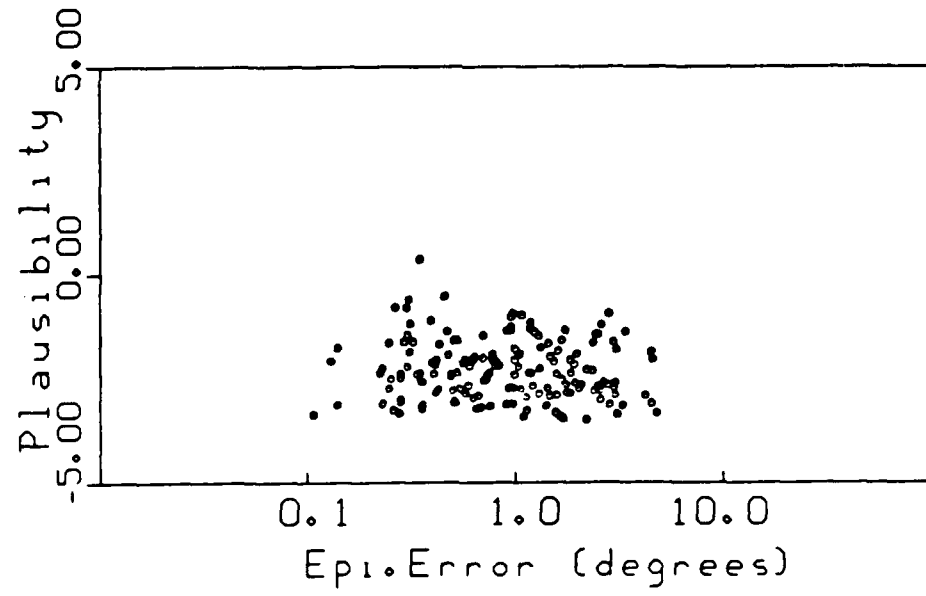
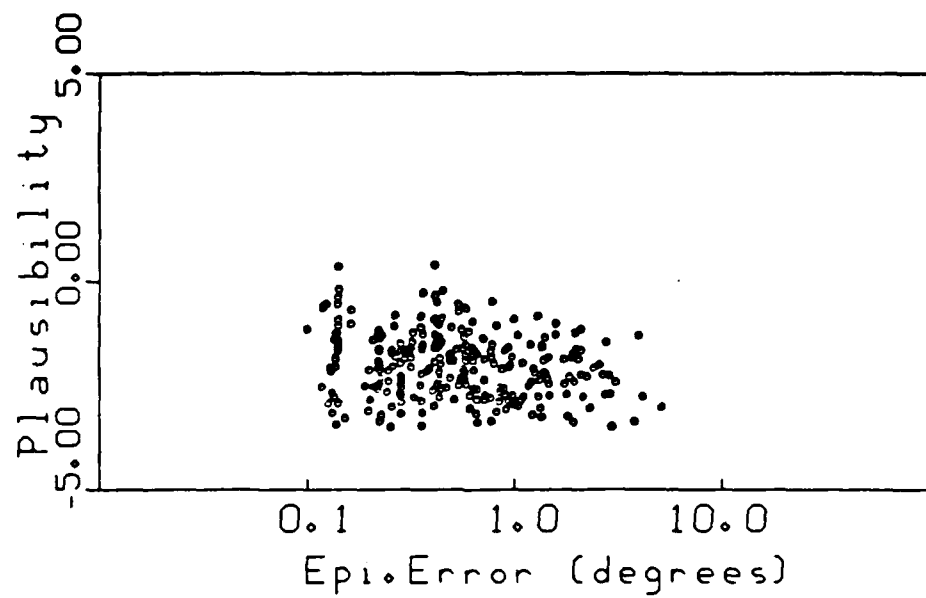


Figure 2. Event plausibility and estimated location errors for accepted (upper diagram) and rejected (lower diagram) events with six or less defining stations during the re-run. Note that the event plausibility as defined here can take both negative and positive values and that large negative values indicate spuriousness.

$$p_j(m) = \Phi\left(\frac{m - m_j}{\sigma_j}\right)$$

with Φ being a normalized distribution function, and m_j , σ_j , being the station magnitude threshold and associated standard deviation, respectively.

The numbers of events (i.e., earthquakes) detected by the network can be written in the form:

$$N(m) \approx \Phi\left(\frac{m - m_0}{\sigma_0}\right) \cdot e^{-\beta m}$$

with m_0 , σ_0 being the network magnitude threshold and associated standard deviation (4.35 and 0.25, respectively, used here). The exponential factor with exponent β account for the magnitude distribution of the earthquakes. The numbers of events as a function of probability, p , can then be written as:

$$\log_{10}(N(p)) = \log_{10}\left(\Phi\left(\frac{m_j - m_0}{\sigma_0} + \frac{\sigma_j}{\sigma_0} \Phi^{-1}(p)\right)\right) - \log_{10}(e) \beta \Phi^{-1}(p)$$

The calculated relative numbers of events as a function of probability, p , is compared with the empirical frequency distribution of the plausibility values in *Figure 3*, for some stations with different magnitude thresholds, m_j , which have been estimated from noise and P-amplitude data reported during the GSETT. Stations with low magnitude thresholds have their distributions of plausibility values peaked at high values (around 0.60 for NB2 in the figure), whereas, stations with high thresholds have their distribution peaked at low values (around 0.10 for RSON in the figure). There is reasonable agreement between the calculated curves and the observed values in *Figure 3*. Hence, the revised station noise values provide station plausibility value distributions which are reasonably consistent with the observed distributions being a result of the overall AA procedure.

1.2.7. P-Observations beyond 100 degrees

A large percent of the events that were rejected in the analyst's review during the GSETT (about 35 percent for the reconciliation period) was based on defining stations at epicentral distances beyond 100 degrees without being in the PKP caustic window.

Figure 4 shows the distribution of the station plausibility values for defining stations as a function of epicentral distance for standard values (given in GSE/SG5/8) of the amplitude attenuation parameters (upper diagram). The station plausibility is equal to pro-

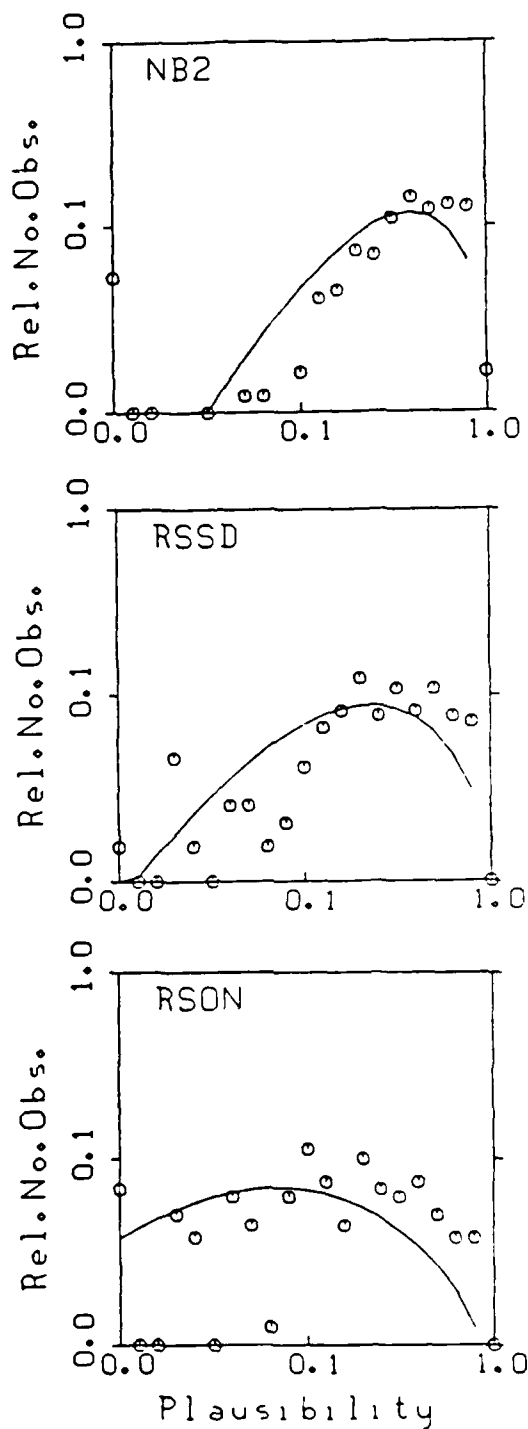


Figure 9. Comparison of empirical frequency density functions (circles, given as a function of relative numbers of events) for station plausibilities compared with calculated functions (curves, also as a function of relative numbers of events) from the model described in the text. The comparison is made for three stations, NB2, RSON, RSSD. The empirical data is limited to observations at epicentral distances less than 100 degrees and covers the whole period of the GSETT.

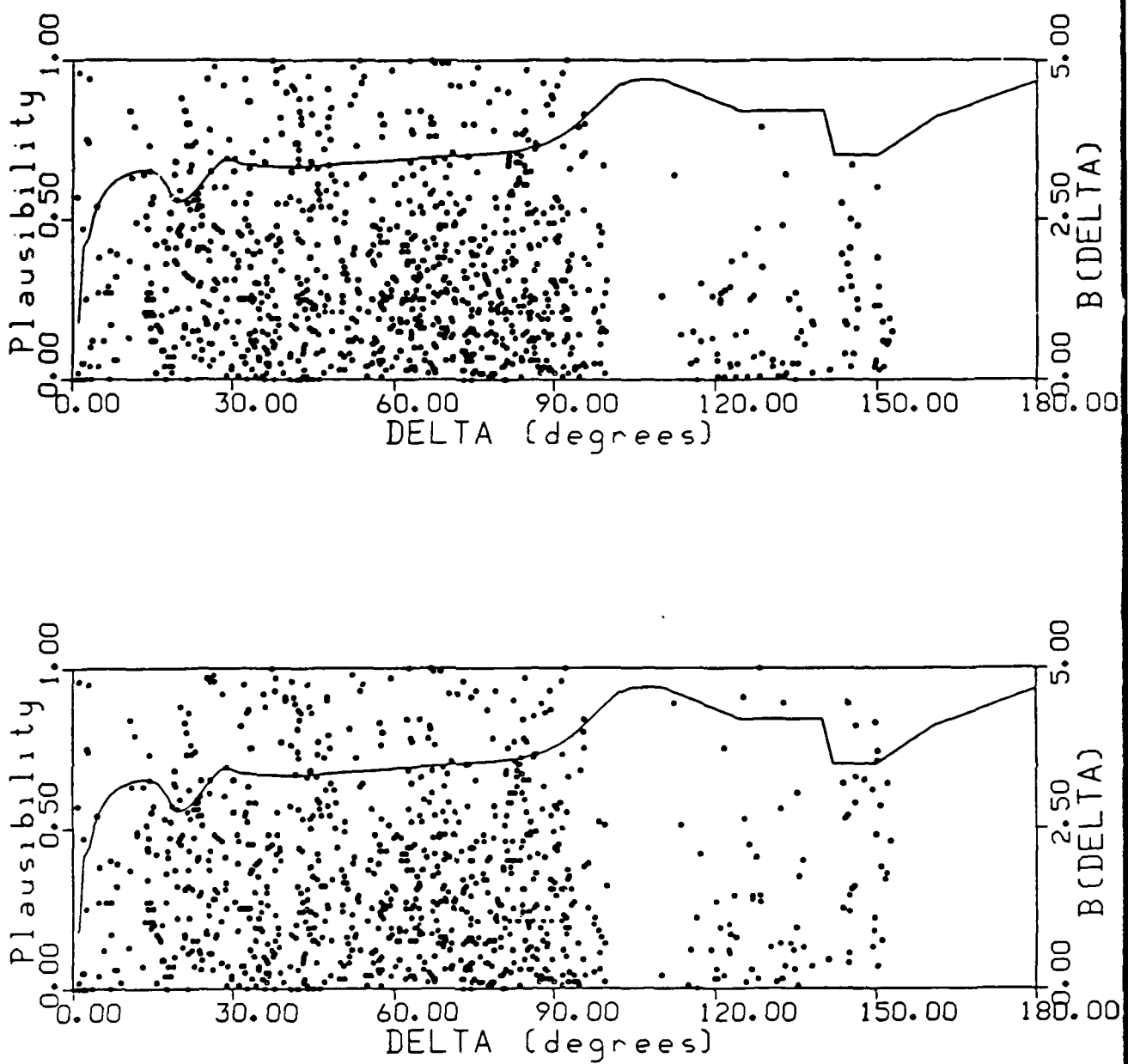


Figure 4. Station plausibilities as a function of epicentral distance for standard (upper diagram) and revised (lower diagram) parameters for P-amplitude attenuation at distances beyond 100. Note that the station plausibility is defined as a detection probability, and thus range between zero and one (scale on left vertical axis). The Veith-Clawson amplitude attenuation curve for zero focal depth extended beyond 100 degrees with the NORSTAR amplitude distance curve is drawn in the diagrams for comparison (scale on right vertical axis).

bility of detecting a P-wave. There is clear difference between the values less than and greater than 100 degrees. At distances greater than 100 degrees the values tend to be systematically lower.

The equivalent scatter diagram between epicentral distance and station plausibility values is shown for events defined using a revised P-amplitude attenuation curve and signal standard deviation (0.4) (lower diagram in *Figure 4*). This gives a more uniform distribution as a function of epicentral distance. In other words the revised P attenuation curve with associated standard deviation gives not only a reduced number of rejected events as mentioned in Section 4.1, but also increased station plausibilities for distances larger than 100 degrees.

1.2.8. Location Accuracy

The location capability of the GSETT network is subject of a separate study and here only a comparison is made between the GSETT epicenters and the determinations reported in the NEIS Monthly Bulletins.

The epicentral error estimates provided by the location algorithm of the AA-program are equal to the formally estimated standard deviations from the location equations linearized around the final hypocenters. That is to say that the standard deviations are obtained from the diagonal elements of the covariance matrix, and with *a priori* standard deviations of the observational errors.

The error estimates are given as errors in latitude, *dlat*, and longitude, *dlon*, and for the purpose here, the estimated epicentral error, *e*, is defined by:

$$e^2 = dlon^2 \cdot \cos^2(lat) + dlat^2$$

The estimated epicentral errors are compared in *Figure 5* (left diagram) with the distance between epicenters obtained here and those reported by the NEIS, which was using about ten times the number of seismological stations for their locations. The comparison is made for about 700 common events with epicenters within 15 degrees. The GSETT epicenters and associated error estimates were only given to 0.1 degree of a latitude and longitude, which gives somewhat limited resolution for events with small estimated errors and small distances. The estimated errors, as defined here, are all less than five degrees, whereas, the distance between the two kinds of epicenter estimates exceed ten degrees in several instances. The data in *Figure 5* (left diagram) scatter in a triangular area for distances less than one degree and the data indicate that events with small estimated errors (say less than 0.1 degree) can indeed have large epicentral differences (more than one degree). Moreover, events with large estimated errors (more than one degree) can have epicentral differences less than one degree, even if these differences are usually larger. Finally, events with small epicentral differences (less than 0.01 degree) usually have small estimated errors (less than 0.05 degrees).

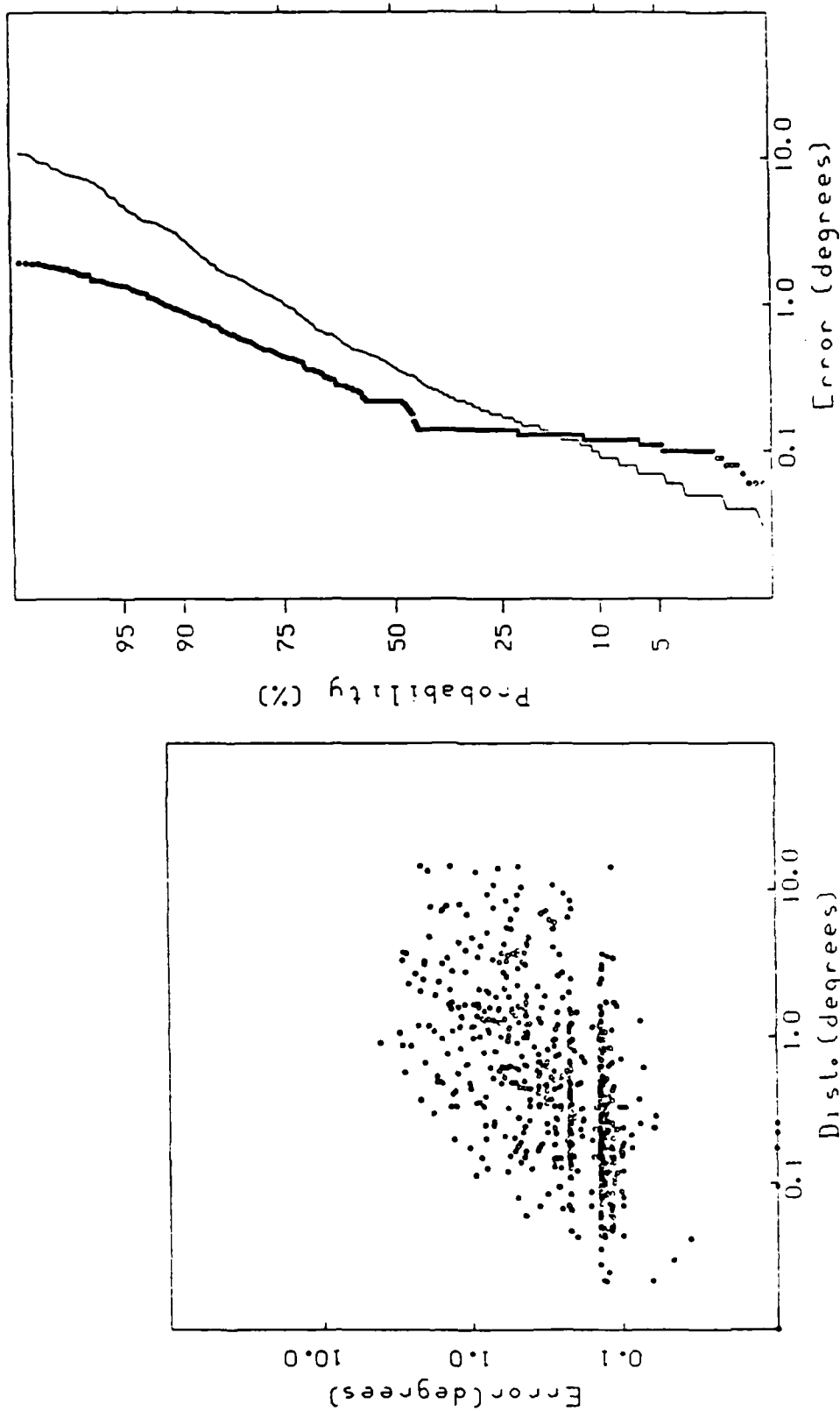


Figure 5. Comparison of estimated epicentral location errors and distances between epicenters obtained here and by the NEIS (left diagram). The diagram to the right compares empirical distribution functions for the estimated errors (shown as dots) and for epicentral differences between GSETT and NEIS (shown as thin line). The vertical scaling in the diagram to the left makes empirical distributions that are exactly normal appear as straight lines.

Figure 5 (right diagram) also shows the empirical distribution functions of the estimated errors and the epicentral differences. The curves follow approximately normal distributions above 0.1 degree, and have about the same standard deviation (i.e., about the same slope). The curve for the estimated errors has, however, a mean value about a factor 2.8 or so smaller than that for the epicentral differences. If the estimated errors were multiplied by this factor the two curves would roughly coincide. In other words, the distribution of the estimated errors at a 92 percent confidence level approximately agrees with the distribution of the epicentral differences.

1.2.9. Depth Estimates

The depth estimation capability of the GSETT network is subject of a separate study and here only a comparison is made between the GSETT depths and those reported in the NEIS Monthly Bulletins.

Error estimates of GSETT depth determinations are obtained in the same way as those for the epicentral coordinates. The depth estimates obtained by the AA-program are based on least squares fitting of first arrival times and depth phases. For the re-run, 365 events (or about 40 percent) of the events had their depth estimates based on depth phases. Estimates based on depth phases usually have small estimated errors and can, for a given station, be based on only a depth phase and no first arrival time from that station. For events based on a few detecting stations this frequently occurs. In such cases the depth phases may be incorrectly identified first arrival phases, and the estimated uncertainties do not take this phase identification uncertainty into account.

The estimated depth errors are compared with the difference of the depths obtained by the program here and those reported by the NEIS, which are not restricted to 33 km. As mentioned above the estimated errors for depths based on depth phases are usually quite small, and the comparison is, therefore, made for events based on depth phases as well as events without depth phases.

The comparison is summarized by the empirical distribution functions in *Figure 6*, which shows that the distribution for the estimated errors is similar to that of the depth differences for those events that are not based on depth phases (right diagram), whereas, there is a large difference for events based on depth phases (left diagram). The distribution for the differences are however quite similar in both cases. It is concluded that the estimated errors for events based on depth phases are much too small.

1.2.10. Surface Wave Associations

The procedure for association of long period Rayleigh waves has earlier been described in detail,(GSE, 1984) and for the purpose of the experiments here standard values of the computational parameters that drive the program were used throughout the computations. This means that Rayleigh wave detections at two stations were considered sufficient to determine a surface wave magnitude, M_s .

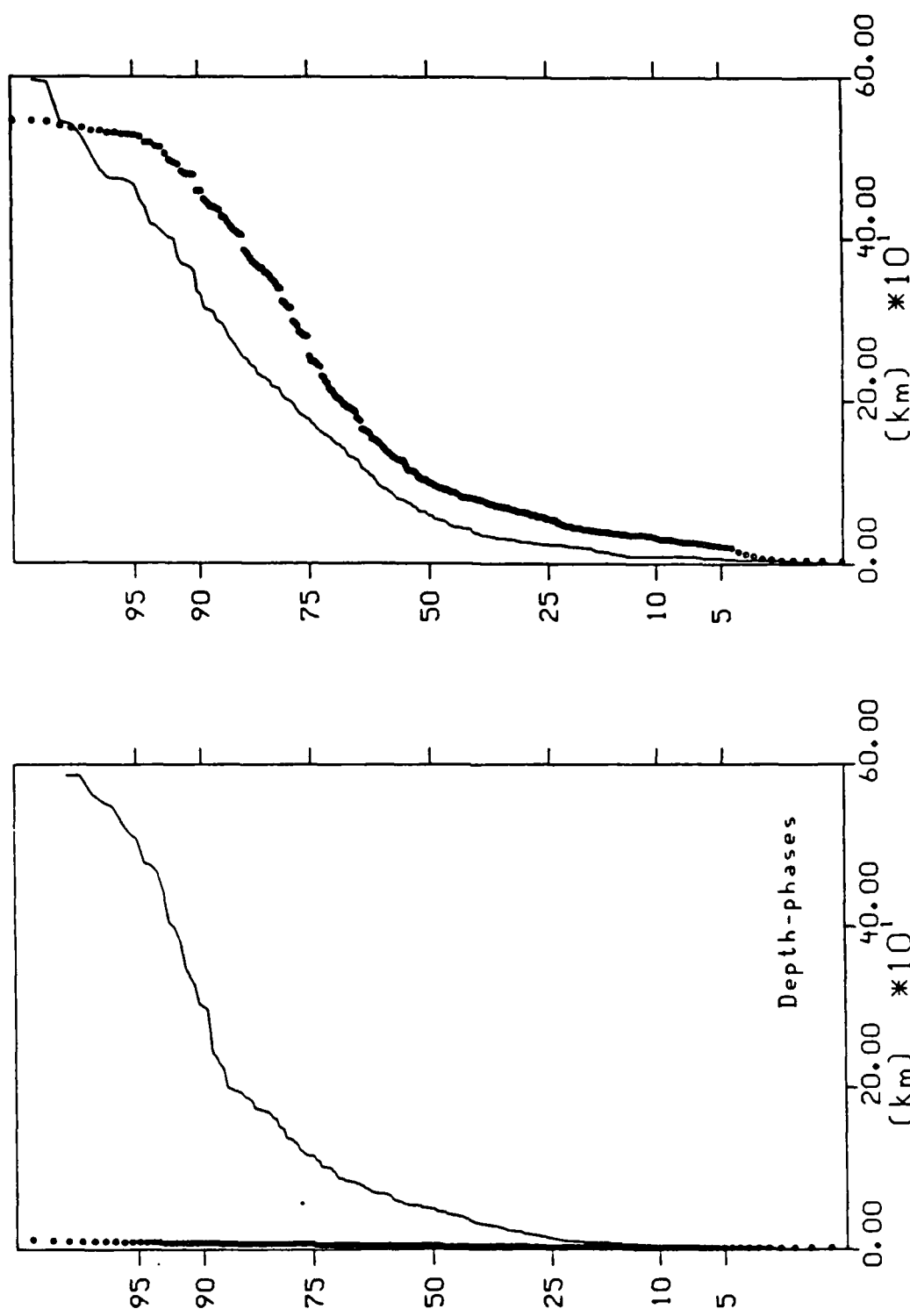


Figure 6. Comparison of empirical distribution functions for estimated depth errors (shown as dots) and differences between depths obtained here and by the NEIS (shown as thin lines). GSETT depths based on depth phases (left) and based on no depth phases (right) are shown separately.

Long period surface wave data were available for a total of 41 of the GSETT stations at the EIDC in Washington. Average station noise amplitudes were computed for these stations on the basis of reported data and used in the amplitude consistency check and the magnitude estimation.

Surface wave magnitudes could be calculated for 243 events (about 25 percent of the total number of detected events), which is about twice the number obtained by the EIDC's during the GSETT. This number is also somewhat larger than the numbers of events for which determinations of M_b was reported by the NEIS (175) for the GSETT period.

The M_b -values reported by the NEIS and those obtained here are compared in Figure 7, which shows general agreement. The maximum likelihood estimation technique employed here gives values similar to the straight averages compiled by the NEIS also at lower magnitudes.

The numbers of events, for which determinations could be made as a function of m_b , is plotted in Figure 8, and the figure shows that the difference in capability to define and locate events and to determine surface wave magnitudes is about 0.7 magnitude units for the GSETT network.

The capability of the GSETT stations to determine M_b has also been calculated as a function of geographical location in Figure 9 from the station noise amplitudes by the called "Networth" method. The 90 percent threshold varies with more than one magnitude unit with region.

The surface wave magnitude data have been plotted in Figure 10 against m_b for shallow earthquakes, i.e., earthquakes, for which NEIS has reported a depth less than 30 km. A linear relation : $m_b = 0.64 \cdot M_b + 1.71$ obtained from linear regression is also drawn for comparison in the scatter diagram. This is in reasonable agreement with relations obtained earlier for much larger event samples (e.g., $0.63 \cdot M_b + 2.03$) (Weichert, 1973).

The determinations for m_b as well as M_b are made without depth corrections. The effect of depth on the $m_b(M_b)$ -relation is shown in Figure 11 and is compared with a relation obtained from the magnitude formulas as a function of depth for m_b ($dm_b/dh \approx -0.0016$) and M_b ($dM_b/dh = 0.008$) for earthquakes (Veith and Marshall, 1972).

A comparison of $m_b(M_b)$ -data for explosions and earthquakes are shown in Figure 12, where all observations have been plotted regardless of estimated focal depth and source type. The five earthquakes in the figure, with m_b -values between five and six and which are among or close to the presumed explosions have depths estimated by the NEIS to be 92 km or larger.

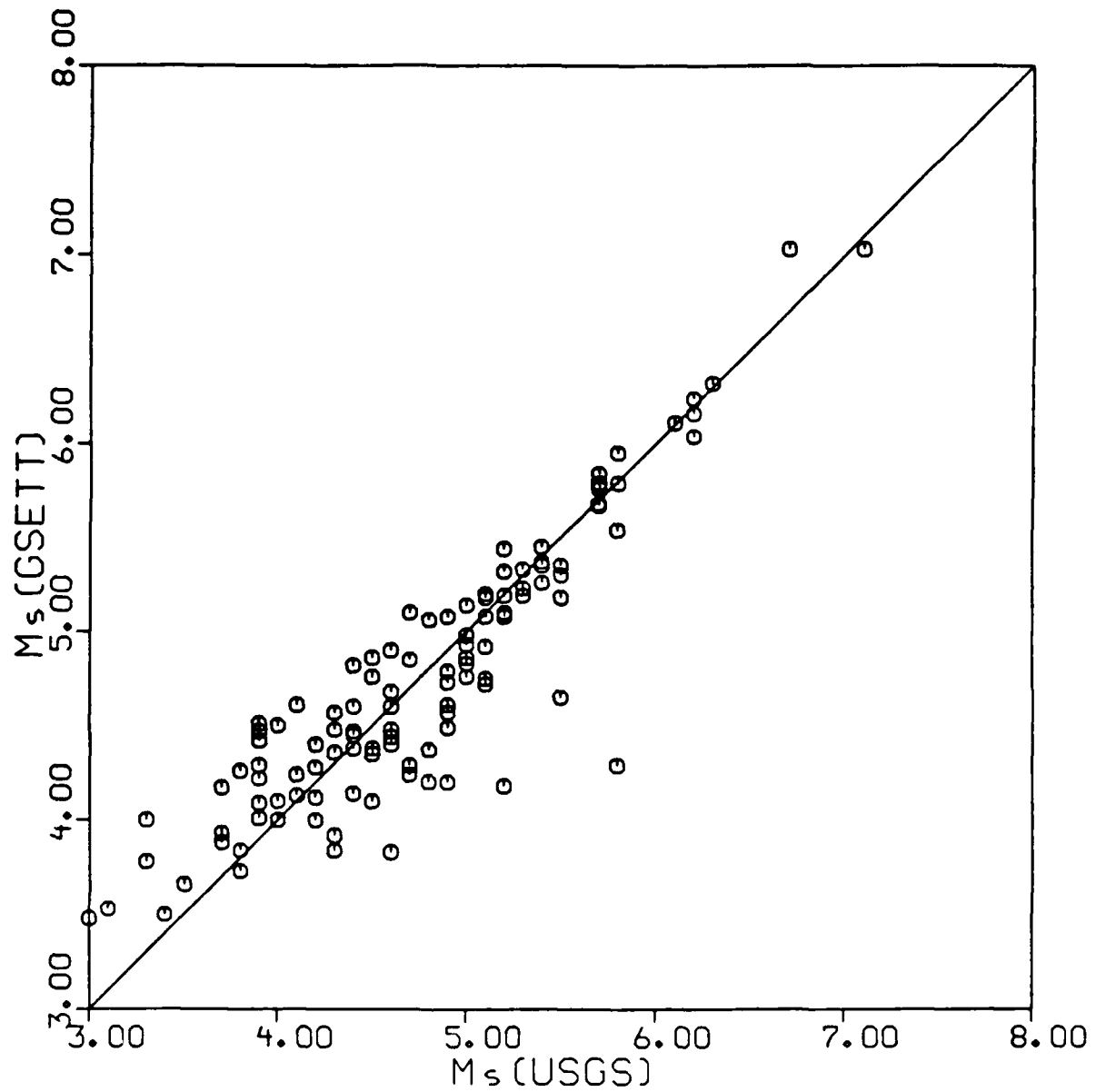


Figure 7. Comparison of surface wave magnitudes determined by the NEIS and the procedure used here.

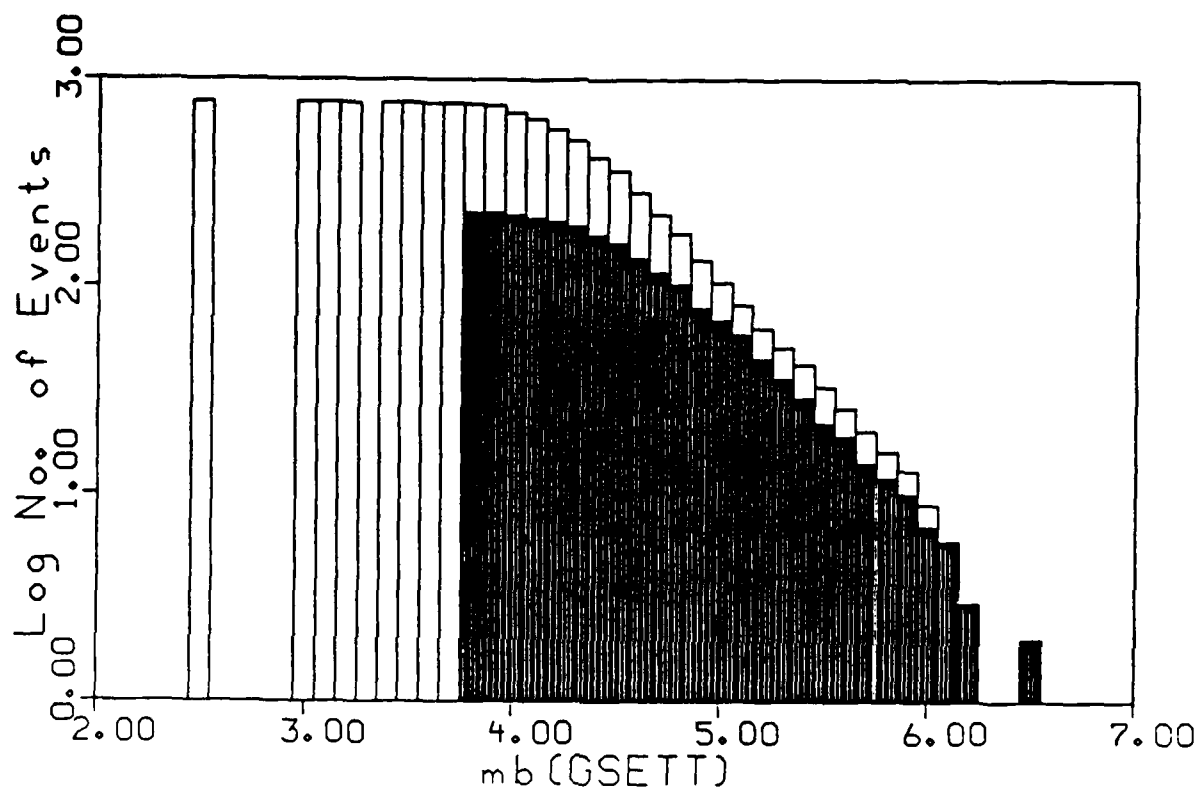


Figure 8. Distribution of body wave magnitudes (m_b (GSETT)) for events for which M_b (GSETT) determinations could be made shown as filled bars. The unfilled bars represent all events detected and located by the AA-program and common with events reported by the NEIS.

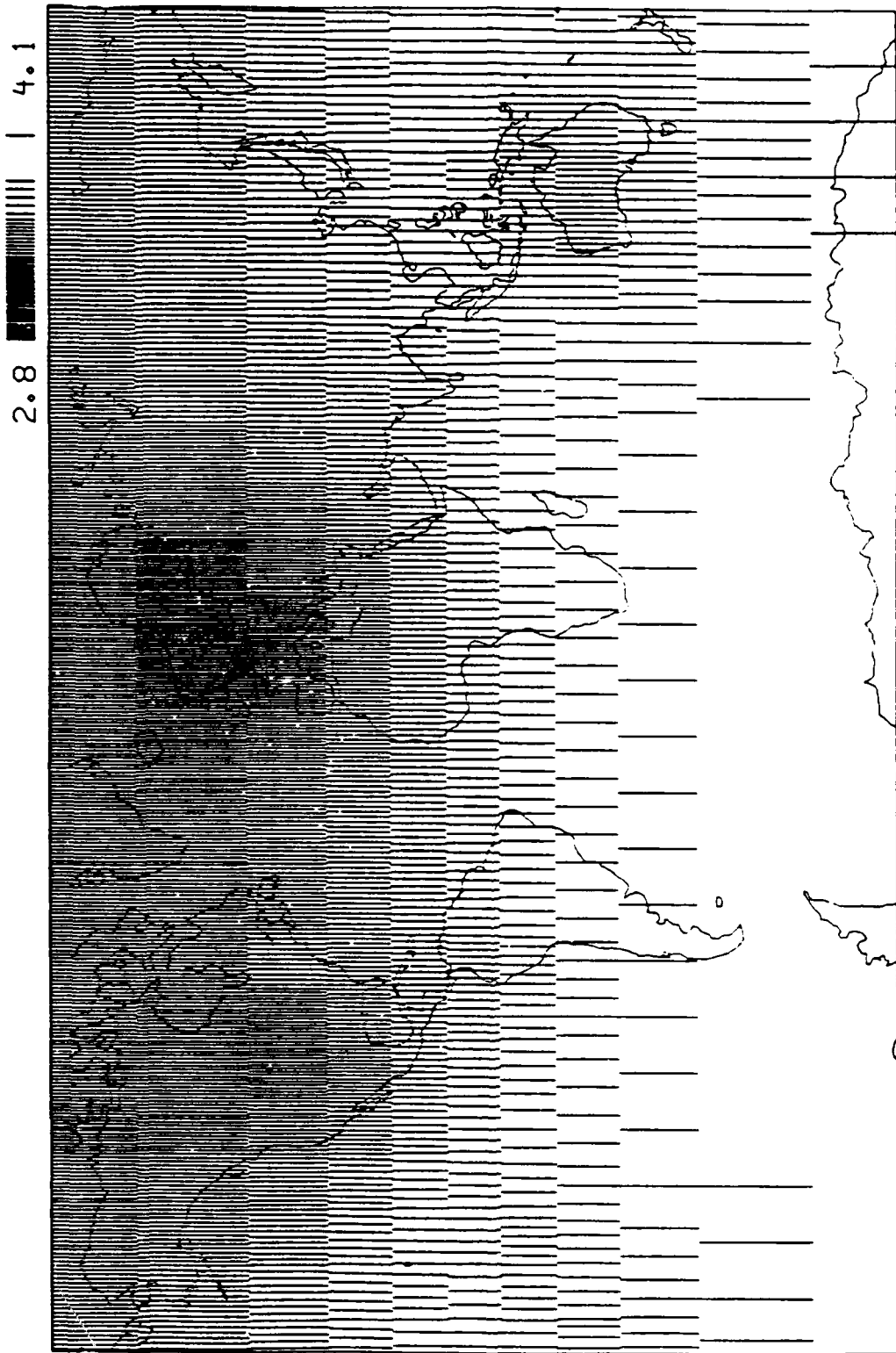


Figure 9. Map showing the 90 percent thresholds (M_s) to determine surface wave magnitudes. The thresholds have been obtained using the so called "Networth" approach, and detections at two or more stations with a minimum signal-to-noise ratio of 1.5 was assumed to be sufficient to define a surface wave magnitude.

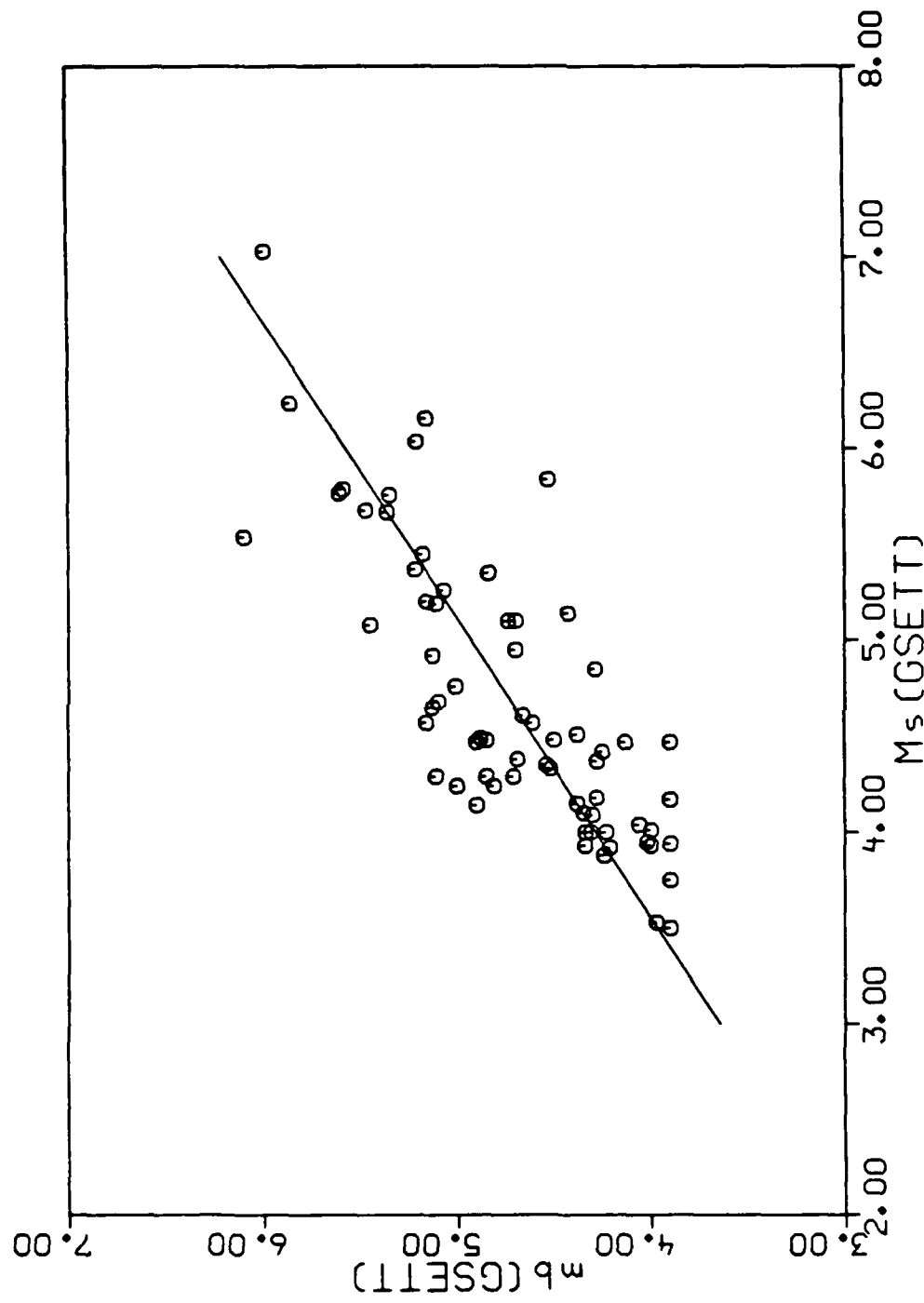


Figure 10. Body wave magnitude against surface wave magnitude for shallow earthquakes (depth less than 30 km by NEIS) during the GSETT. The linear relation $m_b = 0.64 \cdot M_s + 1.71$ obtained by linear regression is shown for comparison.

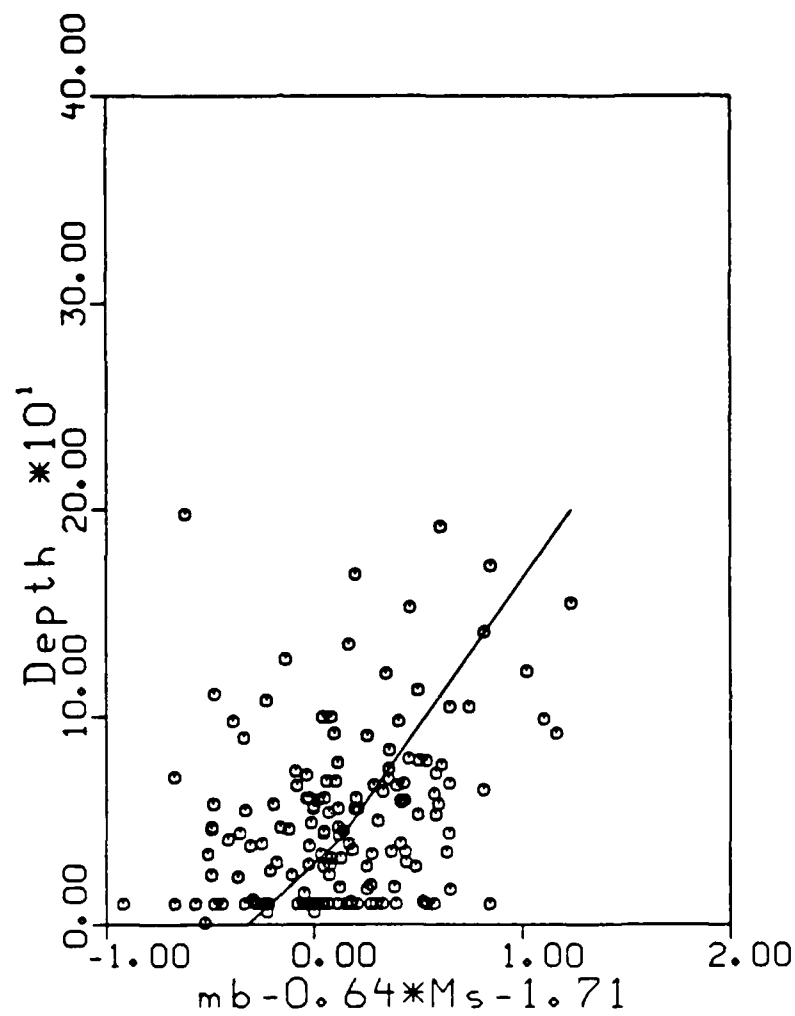


Figure 11. Magnitude difference, $m_b - 0.64 \cdot M_s - 1.71$, as a function of focal depth estimated by NEIS. The curve represents this difference if depth corrections are applied normalized to a depth of 30 km, as described in the text.

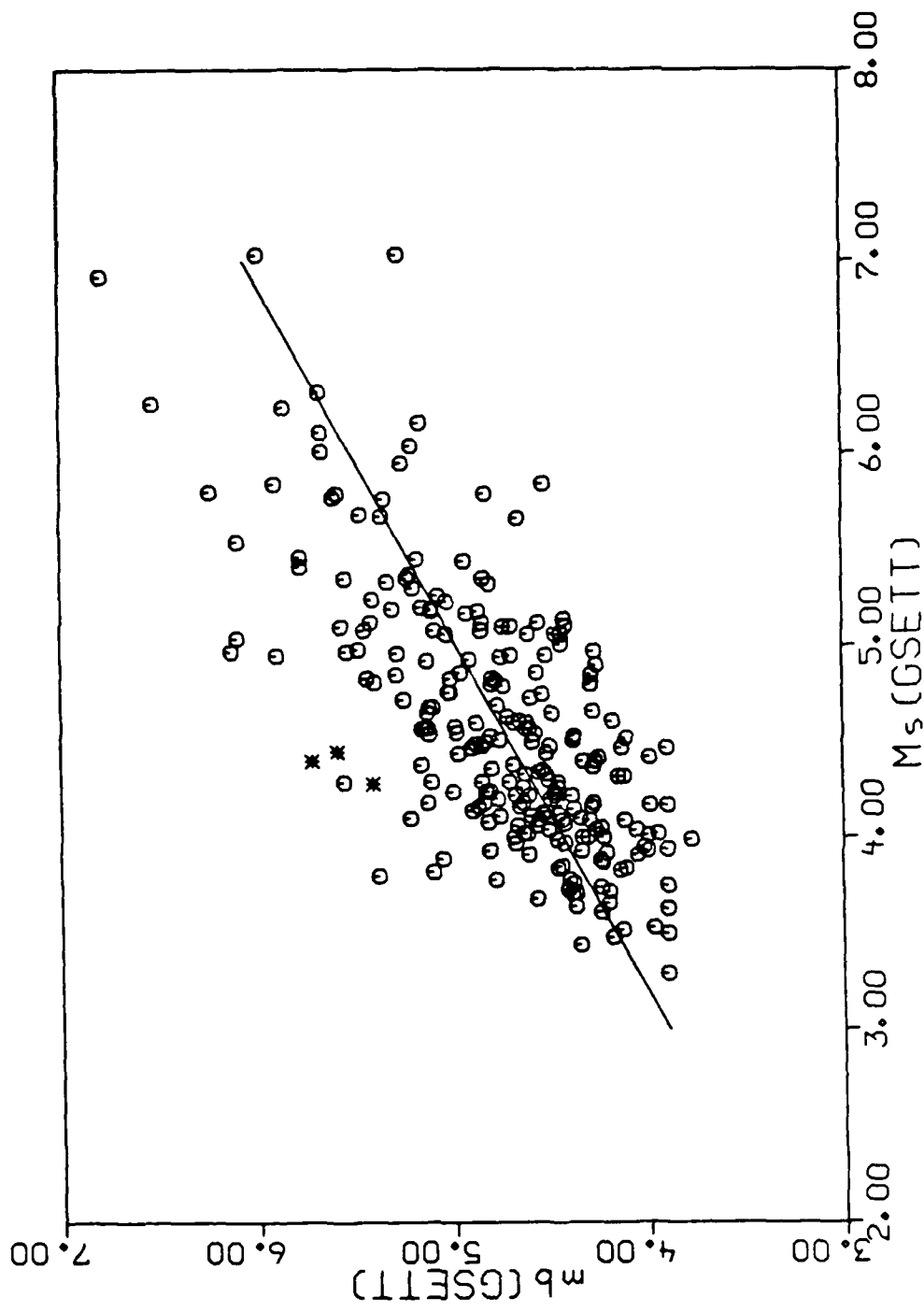


Figure 12. Body wave magnitude as a function of surface wave magnitude for all events during the GSETT regardless of depth. Explosions are indicated by asterisks and earthquakes by open circles.

1.2.11. Concluding Remarks

The computer program for automatic association and location of events gave virtually identical results for test runs on similar but different computers.

Experimental computer runs with the AA-program suggest that the numbers of events that were rejected manually during the GSETT can be reduced by about a factor of two if updated station noise amplitudes are used and some computational parameters of the amplitude consistency check procedure are modified. These computational parameters include description of P-amplitude attenuation at distances beyond 100 degrees.

Use of updated station noise amplitudes and some computational parameters does, however, not dramatically increase the numbers of detected events, even if the defined events generally get larger plausibility values. Neither does additional station data (about ten percent more stations) significantly increase the numbers of detected events.

The epicenter determinations of the GSETT are compared with those of the NEIS. It is concluded that the distribution of the estimated location errors (at a confidence level of between 90-95 percent) is in reasonable agreement with the distribution of the epicentral differences.

A comparison is also made of depths estimated by the GSETT and NEIS. It appears that GSETT depth determinations based on depth phases and a small number of detecting stations do often not agree with those reported by the NEIS, and that the estimated depth errors are underestimated in these cases.

Association of long period Rayleigh wave data made it possible to determine surface wave magnitudes for more than 200 events which is about twice the number of determinations during the GSETT. The capability of determining surface wave magnitudes is still significantly lower (between 0.5-1.0 m_b units) than the capability to detect and locate events by the GSETT station network.

The $m_b(M_s)$ data separate explosions and shallow earthquakes reasonably well for this particular set of events.

Hans Israelsson

REFERENCES

- Elvers, E., 1980. "International Seismological Data Center: Procedures to Check Events through Dynamic Information and to Estimate Magnitudes," *National Defense Research Institute, Stockholm, Sweden, FOA Report, C 20368-71.*
- Blandford, R. R. and Sweetser, E. I., 1973. "Seismic distance amplitude relations for short-period P, Pdiff, PP, and compressional core phases," *Teledyne Geotech, Alexandria, VA, Report SDAC-TR-73-9.*
- GSE/SG5/8, 1984. "A Program for Automatic Association and Location of Seismic Events," *Study Group Working Paper, GSE Conference of Disarmament.*
- Weichert, D. H. and Basham, P. W., 1973. "Deterrence and False Alarm in Seismic Discrimination," *Bull. Seism. Soc. Am.*, 63: 1119-1132
- Veith, K. F. and Clawson, G. E., 1972. "Magnitude from short-period P-wave data," *Bull. Seism. Soc. Am.*, 62: 435-452.
- Marshall, P. D. and Basham, P. W., 1972. "Discrimination between earthquakes and underground explosions employing and improved Ms scale," *Geophys. J. Roy. Astr. Soc.*, 28: 431-458.

2. RESEARCH TO IMPROVE ANALYSIS OF SEISMIC DATA

2.1. USE OF POLARIZATION FILTERING TO ENHANCE DEPTH PHASES IN P-CODA

2.1.1. Introduction

Polarization processing has been applied to P-coda waves of a presumed underground nuclear explosion recorded on the RSTN network. In a previous study, Jurkevics (1986) demonstrated how polarization analysis can be used to identify and isolate ground particle motions with specific polarization signatures. In this application, the same methodology will be applied to teleseismic P-coda in an attempt to separate secondary phases generated in the crust near source from those generated near the receiver. Secondary crustal pulses originating near the source and traveling as P-waves should be polarized much like the direct P-wave. Near-receiver phases, on the other hand, have a higher probability of being differently polarized. The objective of this experiment is to determine the polarization characteristics of the P-coda as a function of time and frequency, and to isolate ground motions which are rectilinearly polarized in the same direction as the direct P-wave. Elimination of the secondary near-receiver phases should facilitate identification of near-source depth phases like pP.

The analysis is performed on RSTN short-period three-component recordings of a presumed underground nuclear explosion in East Kazakh. This event occurred on December 2 (day 337), 1984, and was located at 50.1 North, 79.2 East in the Semipalatinsk region of East Kazakh S.S.R. This was a very shallow event with a body-wave magnitude of 5.2. *Figure 1* shows 15 seconds of the short-period recordings of the initial P-wave codas at four RSTN stations. All the observed signals are well above the noise in the band .5 - 6 Hz. The relative amplitudes of the vertical and horizontal components indicate that the signals are mostly vertically incident P-waves. Even though the signals at these four stations have similar take-off angles and propagation paths through the mantle, *Figure 1* indicates a marked difference between the individual waveforms. One explanation for this difference is that crustal inhomogeneities beneath the receivers, which are different from station to station, generate reflections, conversions and scattered energy arriving shortly after the main P-phase. This will be a dominant factor to the extent that the signals leaving the source to the four stations are identical and propagation effects through the mantle can be ignored.

2.1.2. Preprocessing

The amplitude and phase responses of the recording instrument, earth attenuation and source function were removed from the data before polarization processing was applied. The reasons for this were to improve the time resolution by flattening the amplitude spectra and to remove the phase contributions. The instrument, attenuation and source all have one-sided, causal response functions which tend to overlap and obscure small seismic pulses immediately following larger ones. If the phase responses are removed first, i.e., converted to zero phase, then each seismic arrival should have a symmetric time response. Consequently, adjacent pulses should be identified more easily.

84. 337 RSTN sp recordings

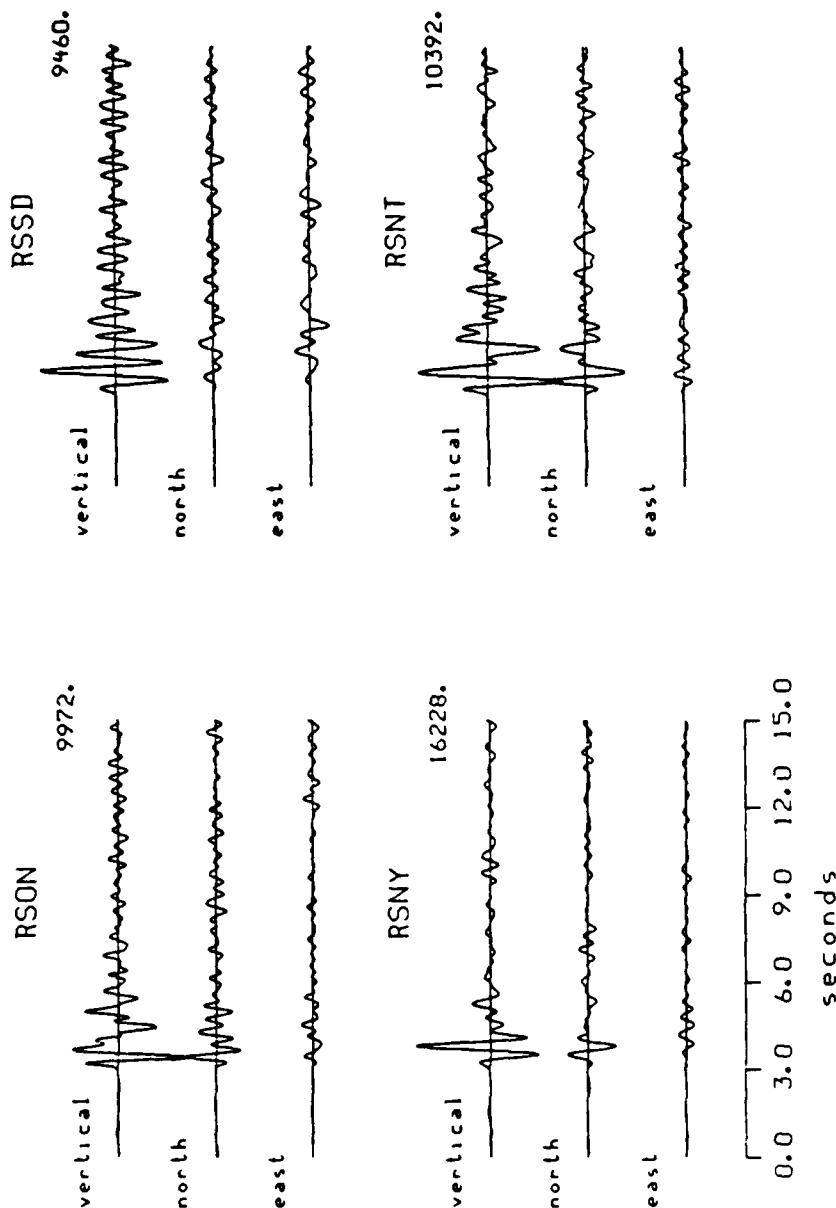


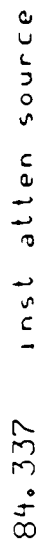
Figure 1. Observed three-component short-period P-wave signals at four RSTN stations for the presumed explosion on day 337 of 1984. The three traces at each station are plotted on the same amplitude scale.

The RSTN short-period instrument displacement response was obtained from Breding (1983). The source function removed was the von-Seggern-Blandford (1972) explosion source model with a corner frequency of 1 Hz and an overshoot parameter of $B = 0.5$. The earth attenuation term was computed using a constant-Q model with a minimum-phase spectrum calculated using the Kolmogorov method (Claerbout, 1976). The attenuation values used for each station were: RSON; $t^* = .2$, RSNY; $t^* = .25$, RSSD; $t^* = .3$ and RSNT; $t^* = .25$ seconds. These values are based on studies of Der, et al., (1984). The source and attenuation corrections were chosen as approximate values which would remove the gross contributions to the amplitude and phase spectra and leave details associated with secondary arrivals intact. Inspection of the corrected amplitude spectra showed that the energy at high frequencies was still deficient, so that the data were in fact under-corrected in this case. Possibly using different source parameters or larger attenuation values would be appropriate for these data. Removing the instrument response greatly amplifies low frequency spectral components associated with noise and windowing. Consequently, a zero-phase high-pass filter was applied in order to remove this low-frequency noise. The corner frequency of this filter was .5 Hz. The analysis itself was limited to frequencies below about 6 Hz because the ambient noise level crosses the signal level beyond about 6 Hz for these recordings. Consequently, a zero-phase low-pass filter with a corner frequency of 7 Hz was applied to remove any high-frequency noise amplified by the attenuation correction. Figure 2 shows the three-component seismograms after removing the instrument, attenuation and source responses, and after bandpass filtering. The long-period non-causal sidelobes associated with the zero-phase high-pass filter are clearly evident prior to the main P-wave arrival.

TABLE I			
Theoretical P-waves at RSTN for event 84.337			
Station	Distance degrees	Azimuth degrees	Incidence degrees
RSON	79	185	23
RSNY	83	197	22
RSSD	86	178	21
RSNT	67	170	27

2.1.3. Results

Table I shows the theoretical orientations of the direct P-wave particle motions for the four stations. The distance and azimuth values in Table I were computed from the station and source locations. The incidence angles (measured from vertical) were deduced from a Herrin-68 velocity model excluding crustal effects, i.e., at the base of the crust. The polarization processor computed estimates of the particle motions as a function of frequency and time. Results showed that the ground motions at the time of the direct P-waves are very rectilinear at all four stations. However, the particle-motion orientation at this time is a strong function of frequency in all cases. The estimated polarizations of the initial P-waves are given in Table II.



The figure displays four sets of seismograms, each consisting of three horizontal traces representing different directions: vertical, north, and east. The stations are labeled as follows:

- RSSD**: Vertical trace shows a prominent initial pulse followed by high-frequency noise. North and east traces show low-amplitude continuous waves.
- RSNT**: Vertical trace shows a sharp initial pulse and some low-frequency noise. North and east traces show low-amplitude continuous waves.
- RSON**: Vertical trace shows a sharp initial pulse. North and east traces show low-amplitude continuous waves.
- RSNY**: Vertical trace shows a sharp initial pulse. North and east traces show low-amplitude continuous waves.

Below the seismograms, a scale bar indicates time in seconds, ranging from 0.0 to 15.0 with major tick marks every 3.0 units.

Figure 2. Seismograms after removing the amplitude and phase responses of the recording instrument, the earth attenuation and an explosion source term. The data have also been zero-phase bandpass filtered between .5 and 6 Hz, which causes the sidelobes prior to the main arrival.

TABLE II			
Observed P-waves at RSTN for event 84.337			
Station	Azimuth <3.5 Hz	Incidence <3.5 Hz	Incidence 3.5-6 Hz
RSON	202	20	13
RSNY	191	22	6
RSSD	230*	30*	4**
RSNT	170	28	10

* RSSD: <1 Hz

** RSSD: >1 Hz

For stations RSON, RSNY and RSNT the energy above approximately 3.5 Hz is polarized at a much steeper incidence angle than the energy below 3.5 Hz. This transition occurs at about 1 Hz for RSSD. With the exception of station RSSD, the computed incidence angles at the lower frequencies are consistent theoretical values in Table I. The computed azimuths for stations RSNY and RSNT are also close to the theoretical values. There is a 17-degree discrepancy between the observed and theoretical azimuths at RSON, and station RSSD had an even larger discrepancy. Azimuth estimates for the near-vertically propagating energy are not reliable and are omitted from Table II.

Station RSSD has polarization characteristics which are anomalous relative to the other stations. The energy below approximately 1 Hz is incident at 30 degrees, while the higher frequency energy is almost vertically incident. Taylor (1982) has discovered a strong frequency-dependent S_V interference effect on the short-period horizontal components at RSSD which causes an apparent delay of the horizontal components relative to the verticals at the lower frequencies. This effect was not observed at the other RSTN stations. The reason for the change in incidence angle with frequency for the other RSTN stations as observed in this study is not clear at this time. One explanation is the interference effect of the surface phase P_p . The instruments are all 100 meters below the surface and the delay time of P_p-P is constant, so the apparent interference effect of this phase should be a function of frequency. Further investigations are required to clarify this point.

Figure 9 shows the outputs of polarization filtering applied to the corrected traces in Figure 2. Only particle motions which are rectilinearly polarized in the same direction as the initial P-waves are passed. Two different cases corresponding to the two dominant initial P-wave particle motions are plotted for each station. The azimuths and incidence angles used to pass the motions in the polarization processor are those listed in Table II and specified on the left side of each trace. The aperture setting used in the polarization algorithm was quite narrow; $n=80$. The results in Figure 9 show that the high frequencies are more vertically polarized than the low frequencies. Station RSSD is anomalous; except for the very low frequencies, most of the energy is almost vertically polarized.

81°. 337 P polarized

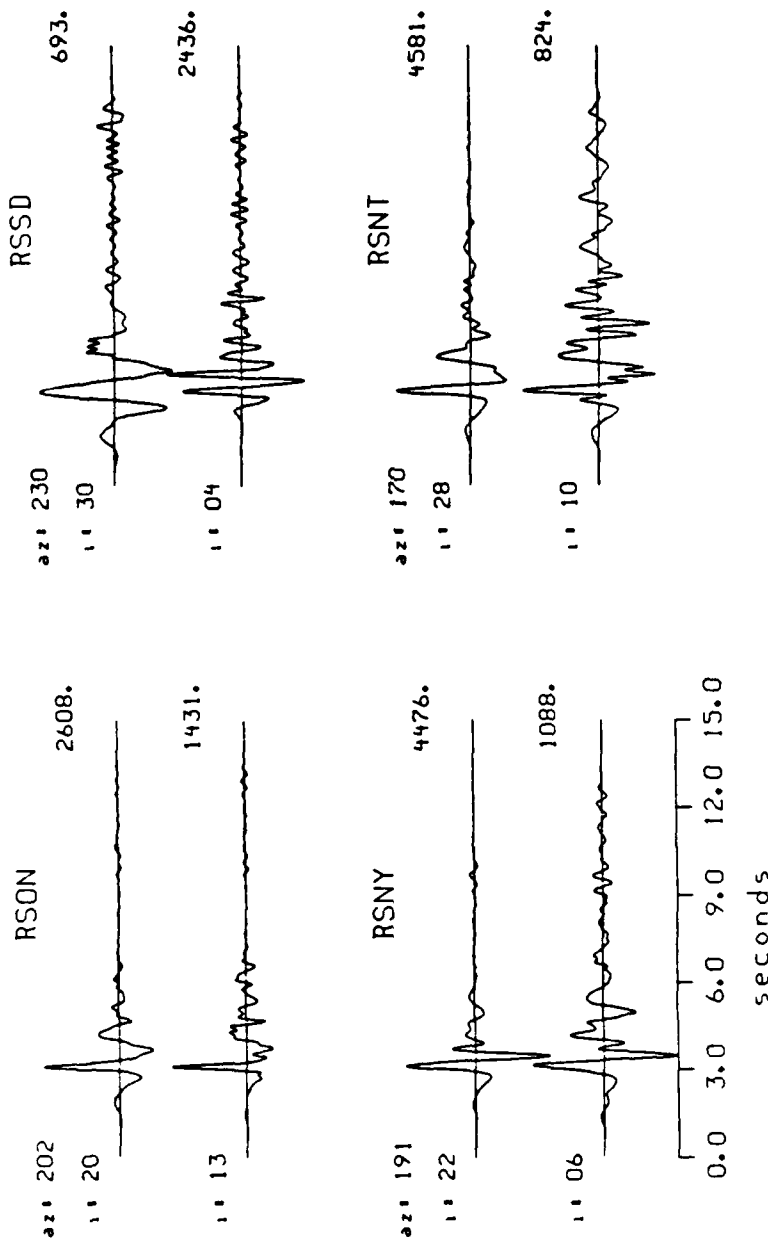


Figure 3. Polarization filtering applied to the signals in **Figure 2**. Rectilinear particle motions with two different orientations are passed for each station; αz values are the azimuths and i values are the angles of incidence. The high-frequency energy is more vertically oriented than the low frequency, and polarization filtering has attenuated much of the energy in the coda following the direct wave.

Because of the deterministic phase corrections and the zero-phase filters applied prior to and during the polarization processing, an isolated seismic pulse should appear as a symmetric zero-phase wavelet in the output. The processed waveforms in *Figure 9* are not zero phase and the energy trailing out behind the direct P-wave pulse indicates the presence of secondary pulses. The time resolution of the polarization filter is determined by the window length and is inversely proportional to frequency (Jurkevics, 1986). A window length of 3 cycles of each passband center frequency was used here. The processing algorithm assumes that the particle motion is purely elliptically polarized over several cycles of its duration. Consequently, the time resolution increases with frequency and is about .5 seconds at 6 Hz for a window length of 3 cycles. In order to resolve time intervals of the order .2-.5 seconds typical for pP-P delay times of scaled-depth explosions, a .5-second time resolution is barely adequate. *Figure 9* shows that polarization filtering attenuates much of the coda energy at the larger incidence angles. After processing, the near-vertically incident energy at RSNY looks quite similar to the waveforms at RSON and RSNT. A common feature is the low-frequency negative lobe immediately following the main pulse. Station RSSD is an exception; it obviously has very strong near-receiver effects and most of the energy above 1 Hz is polarized vertically.

2.1.4. SYNOPSIS

Three-component recordings of P-waves from a presumed underground nuclear explosion have been analyzed by polarization processing to enhance possible depth phases. The instrument, earth attenuation and source effects were removed first in order to flatten the amplitude spectra and remove phase effects. These three terms have noncausal one-sided signatures which can overlap and mask smaller reflections immediately following larger ones. The objective here was to make first-order corrections to the amplitude and phase spectra but to leave details associated with secondary phases intact.

The polarization processing results showed that the direct P-waves pulses have rectilinear particle motions. However, the particle motion orientation is a strong function of frequency, with the higher frequencies oriented more steeply than the low frequencies. These local crustal effects were found to be strongly station dependent.

The basic assumption made in this analysis was that the P-coda contains may closely-spaced pulses, some of which originate in the source area and propagate directly to the receiver as P-waves, and some of which are reflected, converted and scattered in the crust near the receiver. The polarization filtered outputs indicated that this is a good assumption for stations RSON, RSNY and RSNT but not RSSD. The RSSD signal is rectilinear and almost vertical for frequencies above 1 Hz and seems to be caused by crustal resonances as opposed to a scattering-type phenomena. Polarization filtering attenuated much of the coda energy at the other stations. The similarities between the waveforms after polarization filtering suggests that much of the remaining signal may be due to near-source phenomena. The asymmetric forms of the signals at RSON, RSNY and RSNT indicate the presence of negative reflection coefficients within one second of the main arrival. This particular analysis has been constrained by the time resolution of the

polarization algorithm and the limited signal bandwidth, and higher frequency recordings should improve the results. Deterministic corrections for the crustal responses at the individual stations would also benefit. An analysis of this nature using three-component array recordings of events at regional distances and including deterministic crustal corrections will be carried out in the near future.

Andy Jurkevics

REFERENCES

Breding, D., 1983. "User's Guide for the Regional Seismic Test Network (RSTN)," *Sandia National Laboratories Report, SAND82-2935*.

Claerbout, J. F., 1976. "Fundamentals of Geophysical Data Processing: With Applications to Petroleum Prospecting," *McGraw-Hill, Inc.*

Der, Z., McElfresh, T., Wagner, R., and Burnetti, J., 1984. "Spectral Characteristics of P-waves from Nuclear Explosions and Yield Estimation," paper submitted to *Bull. Seism. Soc. Am.*

Jurkevics, A., 1986. "A Polarization Processing Algorithm with Applications to RSTN Data," *SAIC Quarterly Technical Reports for July-September and October-December 1985, Technical Report C86-05.*

Taylor, S. R., 1982. "The Nature of P-Waves at the RSTN station RSSD," *Lawrance Livermore Laboratory Report, UCID-19504.*

von-Seggern, D. and Blandford, R., 1972. "Source Time Functions and Spectra of Underground Nuclear Explosions," *Geophys. Jour. R.A.S, Vol. 31.*

2.2. CORRELATION OF P-CODA TO DETECT DEPTH PHASES: APPLICATIONS TO RSTN DATA

2.2.1. Introduction

A simple correlation technique, similar to cepstral stacking was applied to multi-station and single-station RSTN data to determine the delay time and polarity of presumed pP depth phases. P-coda were analyzed from short-period recordings of two nuclear explosions which occurred on October 27, 1984 ($mb = 6.1$) and December 2, 1984 ($mb = 5.2$) at the East Kasakh test site. The analysis indicates that both recordings contain secondary arrivals with delay times and polarities appropriate for pP phases for events in this region. In addition, the use of polarization filtering to enhance depth phases is illustrated for the December 2 event.

The ability to detect depth phases on short-period seismograms is influenced by many variables, most fundamental of which are the bandwidth of the recorded seismic signals and the coherence between the direct and the surface-reflected phase. Depth phases such as pP, with typical delay times between 0.2 and 0.5 seconds for explosions, cannot be separated clearly from the direct arrival when signals are not recorded above frequencies at which these two arrivals interfere (2-5 hz). Coherence between P and pP, which has been shown to be a marginal assumption (e.g., Day *et al.*, 1982; 1983), is necessary to recognize the delayed arrival as a multiple. But even when high frequencies are recorded with adequate signal-to-noise ratio and the assumption of coherence is valid, spectral amplitudes may be biased by directivity, source multiplicity, path attenuation or site response. In particular, a strong site response can produce multiple arrivals which are unrelated to the source.

In cases where the characteristics of the source and the transmission path are well known, these effects can be removed deterministically. However, in most conventional source studies some station averaging is done to reduce the effects of the path and receiver. The same approach is taken here in correlating P-coda for one event across an array of stations. By performing the analysis in the zero-phase cepstral domain, the cross-correlation operator is transformed to a summation at which stage different averages and weighting schemes can be applied. For single station recordings, an autocorrelation can be performed by computing the power cepstrum.

2.2.2. Data Processing

Figure 1 shows the unprocessed data for two nuclear explosions recorded at four RSTN stations at epicentral distances ranging from 7500 to 9500 km. The P-wave and coda on each trace were windowed using a 20% cosine taper and corrected for the RSTN short-period instrument response. Window lengths between five and ten seconds were chosen to avoid the inclusion of other scattered phases. *Figure 2* contains signal and noise

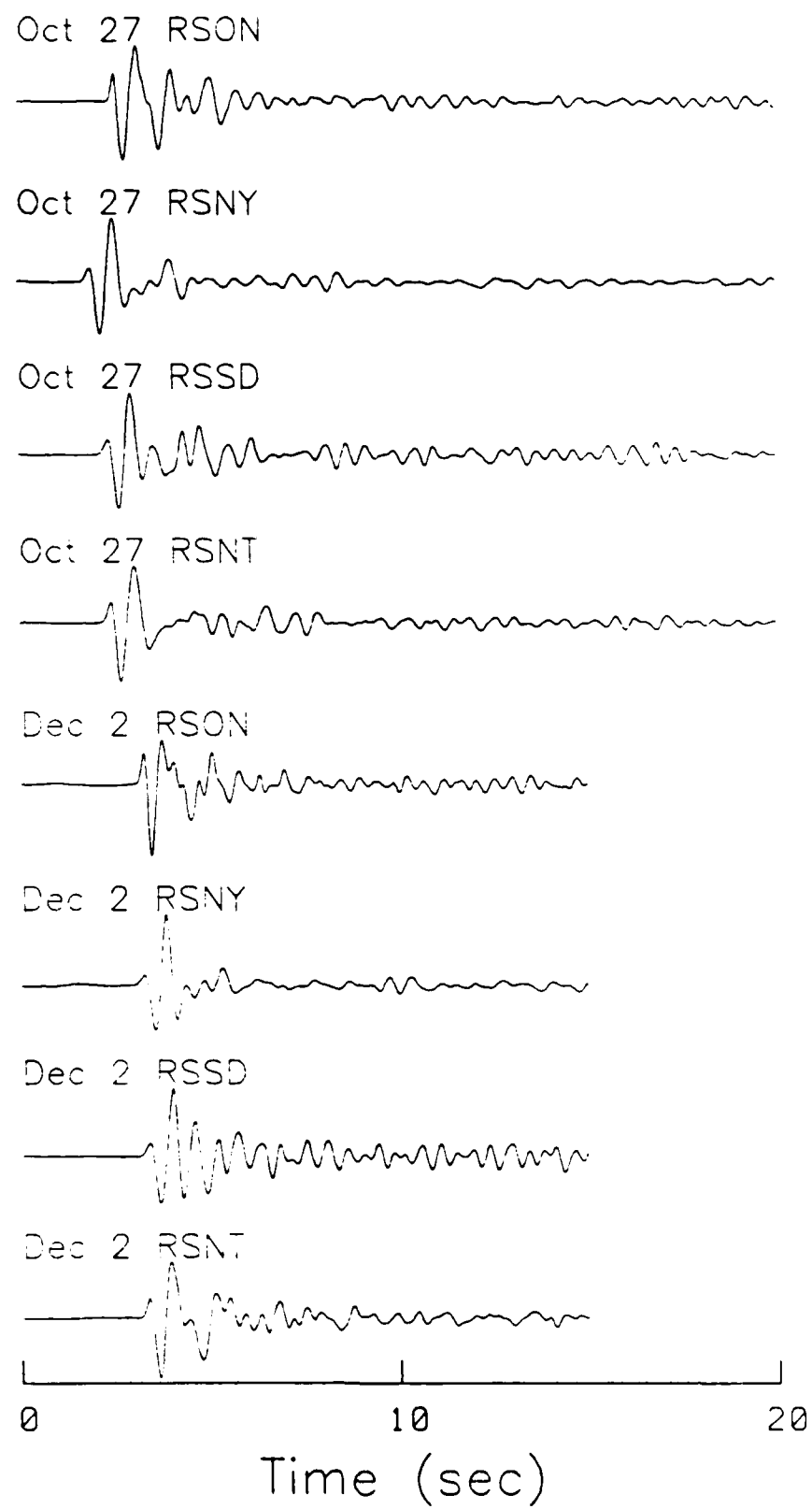


Figure 1. Vertical short-period data for the October 27, 1984 and December 2, 1984 explosions recorded at four RSTN stations.

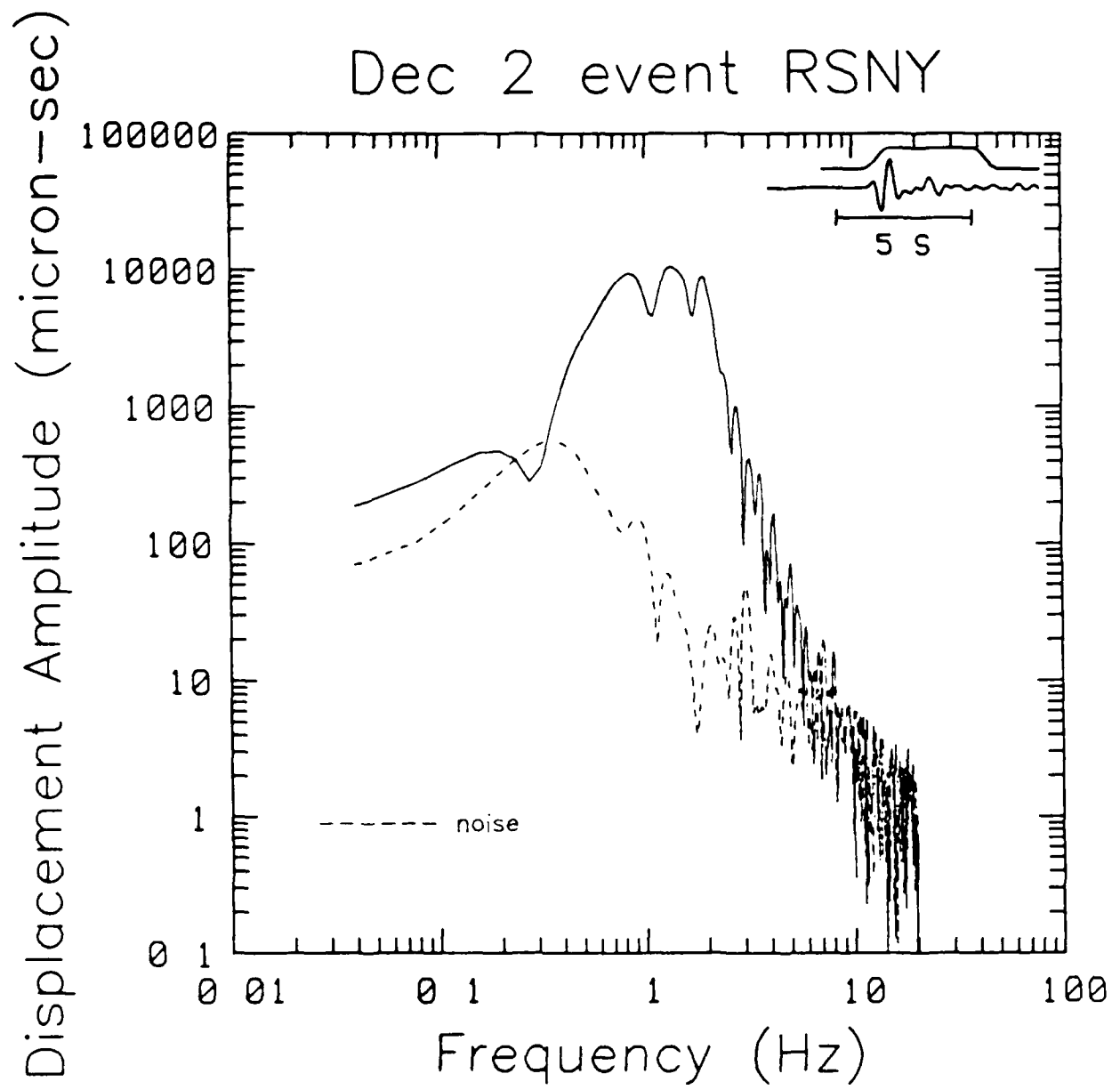


Figure 2. Signal and noise spectra for the December 2 event recorded at RSNY.

spectra for the December 2 event recorded at RSNY; these spectra are representative of those at other sites as well. The signal-to-noise ratio appears to be good up to about 5 hz.

The displacement amplitude spectrum was computed for each trace, and the spectra were preconditioned for the subsequent log operation by adding a static value of one to all amplitudes. The purpose of adding one to the amplitude spectrum before taking the log is to avoid the occurrence of large negative values in the log-spectrum outside the signal band. The addition of one to the amplitude spectrum has a negligible effect on the relatively large amplitudes within the signal band of interest (2-5 hz), and for smaller events the spectrum can be renormalized before this operation. The log-spectrum was then computed to enhance the high-frequency amplitudes and an inverse-transform was made to the cepstral domain where the data can be correlated by summation. Finally, the data were stacked by averaging the amplitudes at all the stations as either a median, mean or weighted mean. A value between zero and one used to weight the mean was derived from the sample variance given by the equation:

$$S^2 = \frac{\sum x^2 - (\sum x)^2/n}{\sum x^2}$$
$$\text{weight} = 1 - S^2$$

2.2.3. Results

Figures 3-5 show the individual and station-averaged cepstra for the two explosions in this study. The variance is displayed at the bottom of each plot. The mean and median averages are not displayed since there is no discernible difference among the three averages for either event due to the small number of stations. The weighted mean average for the October 27 event (Figure 3) reveals the presence of a negative multiple delayed by about 0.3 seconds from the direct P-arrival. The relative amplitude of the secondary arrival is difficult to determine in general due to the 1/n decay of the cepstrum. Note that the variance is lowest in the time interval where the suspected pP phase is chosen.

Figures 4 and 5 show the results from the December 2 event. The waveforms for this event as shown in Figure 1 have a very different appearance at each of the four RSTN stations, as opposed to the October 27 explosion which has a more consistent wave shape across the network. The smaller December 2 event appears to be more strongly affected by the near-receiver response. For this event, a four-station average was not sufficient to resolve the delay time and polarity of the suspected Pp phase. To reduce the effect of the station site, the data for this event have been filtered in two different directions of rectilinear motion (Jurkevics, 1986). Figures 4 and 5 both show the presence of the negative secondary arrival at about 0.3 seconds.

Oct 27 event

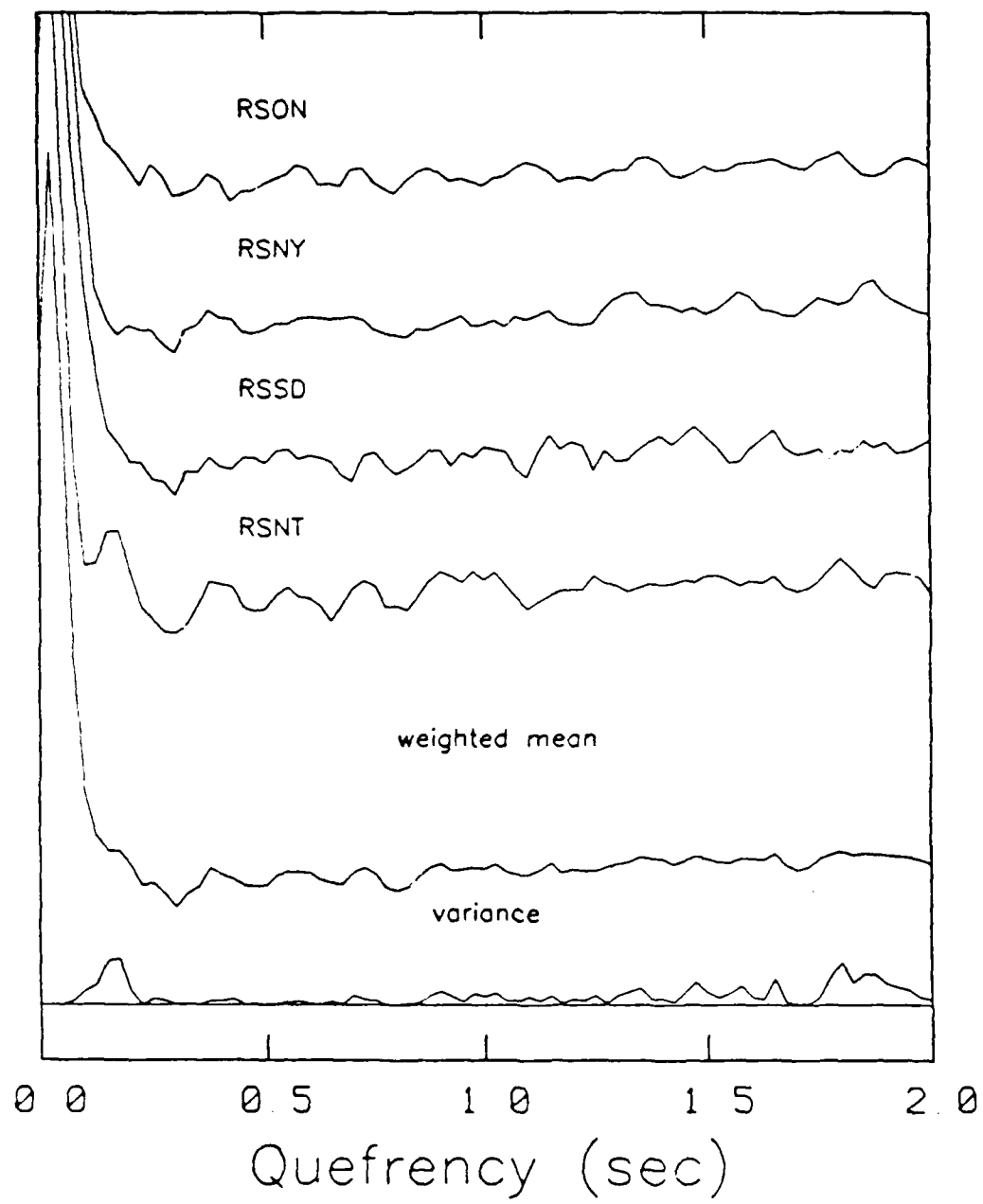


Figure 9. Weighted mean average and individual cepstra for the October 27 explosion.

Dec 2 event Polarfilt1

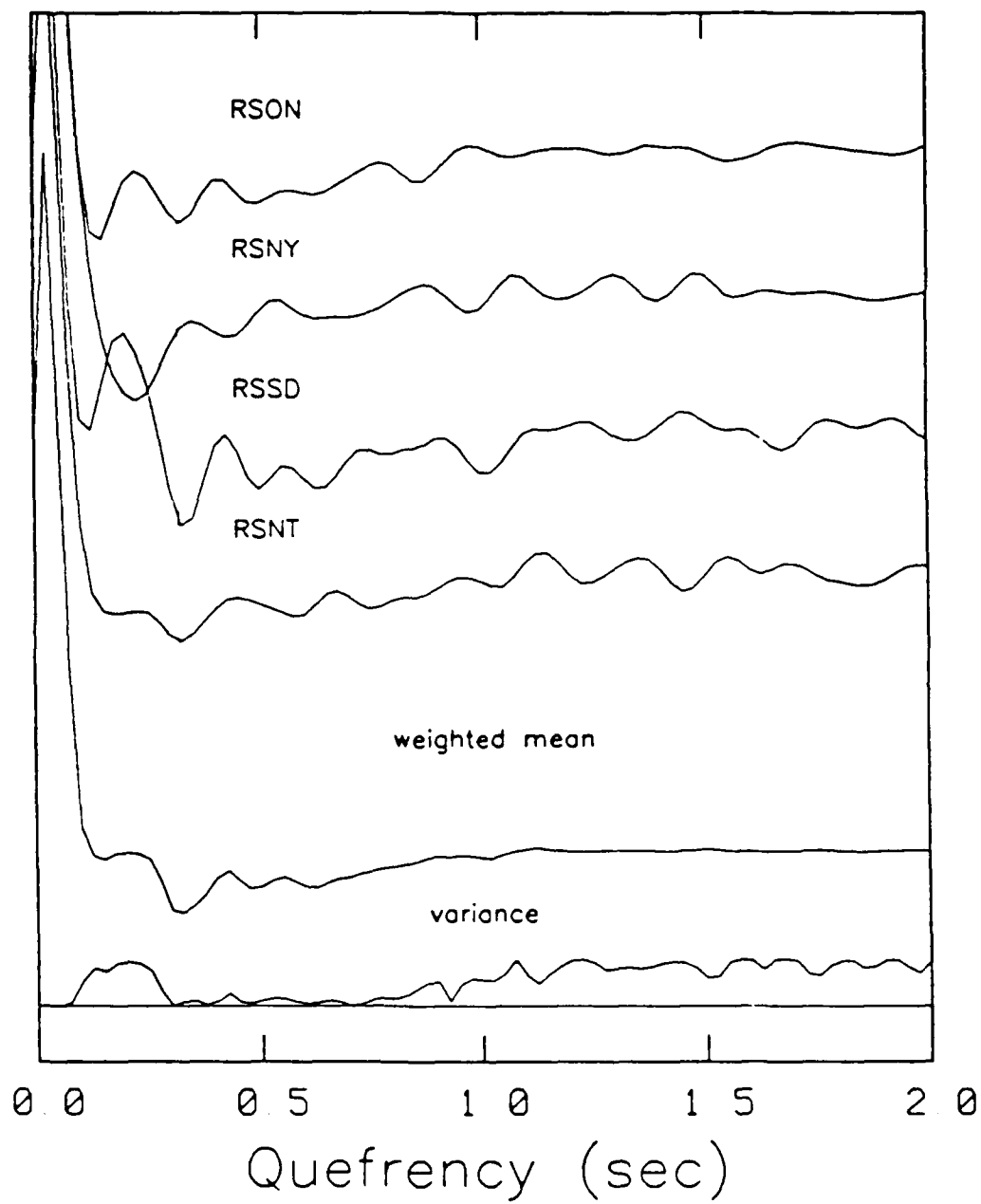


Figure 4. Weighted mean averages of the December 2 event after polarization filtering at 22 degrees incidence angle.

Dec 2 event Polarfilt2

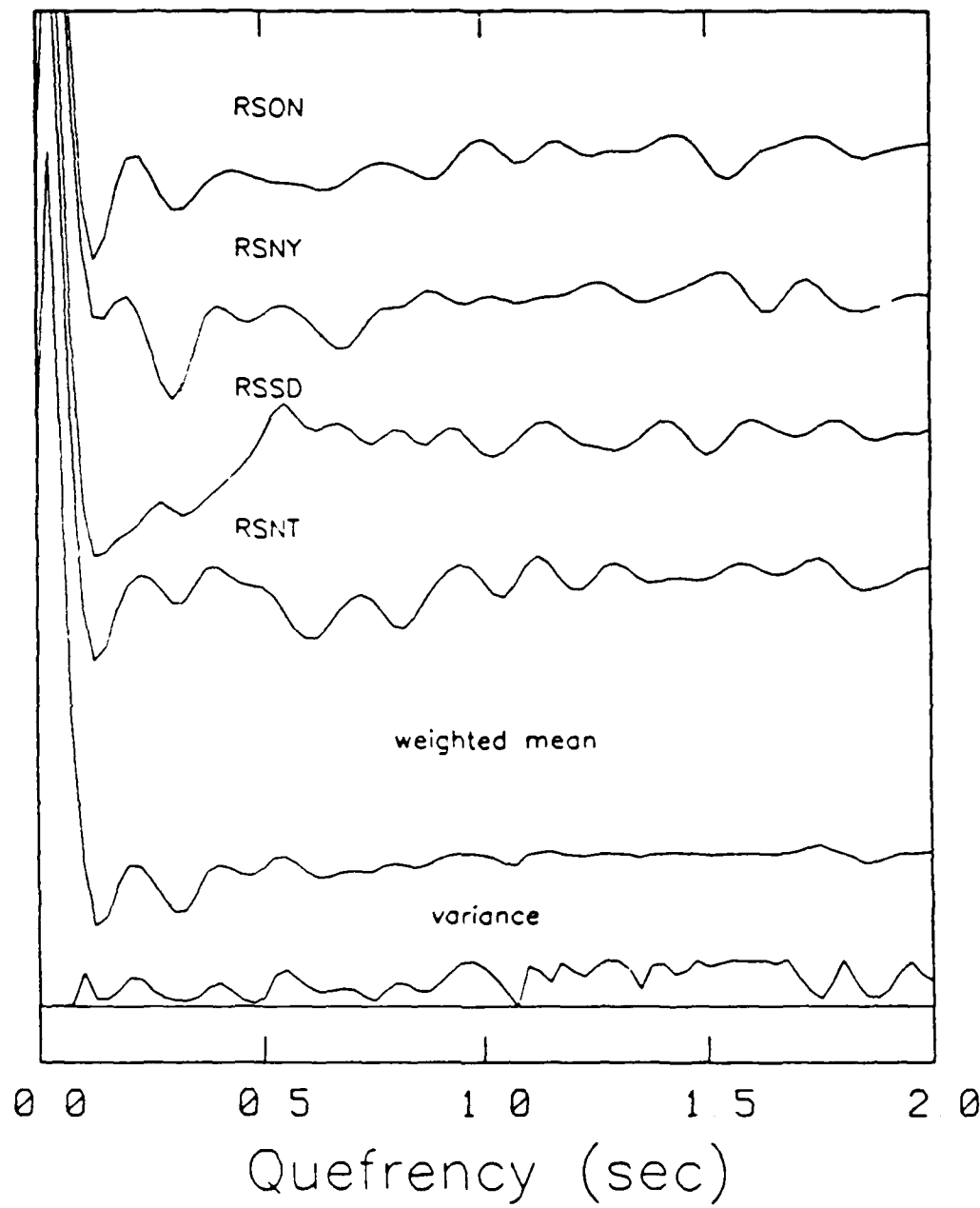


Figure 5. Weighted mean averages of the December 2 event after polarization filtering at six degrees incidence angle.

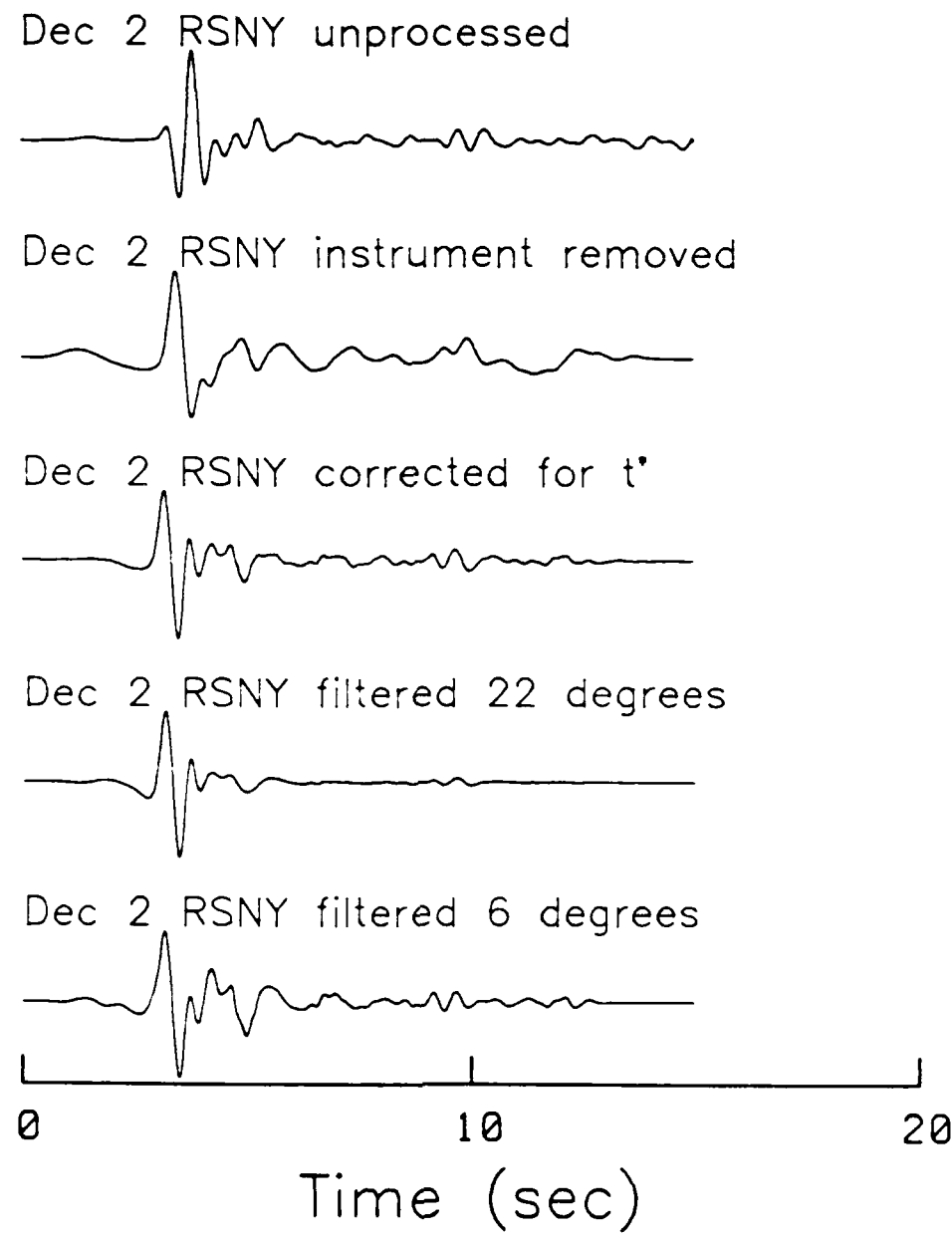


Figure 6. Data recorded at RSNY after each processing step.

Dec 2 explosion RSNY

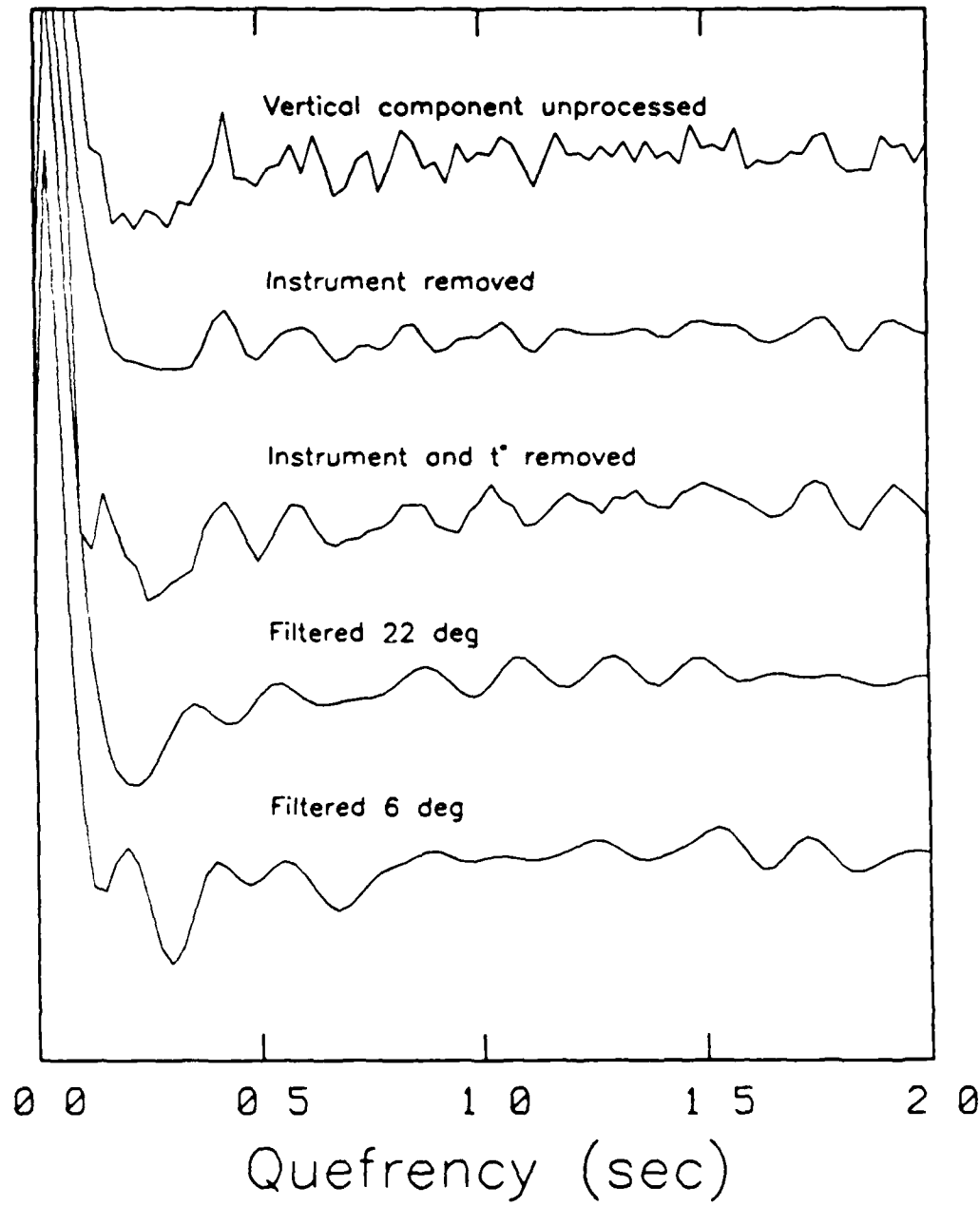


Figure 7. Power cepstra of the December 2 event at RSNY after each processing step shown in Figure 6.

Figure 7 shows power cepstra of the December 2 event at RSNY displayed at three steps in the processing, i.e., instrument removal, attenuation correction and polarization filtering. The cepstra are generally improved by the polarization filtering which suggests that the site response has been effectively removed. In particular, the cepstrum in *Figure 7* after polarization filtering at six degrees shows a strongly coherent multiple with a negative polarity. This angle of emergence, which was shown to have a strong frequency dependence, was chosen to pass the highest frequencies in the data. As demonstrated in *Figure 6*, the same processed data displayed in the time domain does not reveal the delayed arrival, although the deterministic removal of an assumed source and t_0 , and the use of polarization filtering has improved resolution.

2.2.4. DISCUSSION

In many cases the frequencies necessary to resolve the depth phase are near the corner where a host of path and receiver effects can bias spectral amplitudes. The phase characteristics of the direct P and pP phases are not expected to be strongly coherent due to nonlinear effects at the source of shallow explosions (Day *et al.*, 1982; 1983). In spite of these difficulties, cepstral analysis has been used successfully by several researchers to detect depth phases contained in some teleseismic and regional data (e.g., Kemerait and Sutton, 1982; Cohen, 1970). However, methods used in the past have suffered from many of the problems traditionally encountered in cepstral analysis. For example, the stacking of complex cepstra is subject to errors due to the misalignment of data traces and the instabilities associated with phase unwrapping and detrending (e.g., Jin and Eisner, 1984). The averaging of spectra from a number of stations done by other authors appears to obscure information about the polarity of the secondary arrival which is an important diagnostic of the Pp phase.

There are several advantages in analyzing seismic depth phases using the method described here. The summation of zero-phase cepstra represents a true correlation and retains the polarity of the multiple. In addition, traces need not be perfectly aligned and the procedure can be made more robust by using different ensemble averages and weighting schemes.

Although the results given here are encouraging, the signal bandwidth of these data is only marginally adequate to detect multiples delayed by only 0.2 to 0.5 seconds. These results and their interpretation could be improved by the use of higher frequency data and a number of stations sufficient to obtain a significant median or mean average.

Paul Dysart

REFERENCES

- Cohen, T. J., 1970. "Source-depth determination using spectral, pseudo-autocorrelation and cepstral analysis," *Geophys. J. R. Astr. Soc.*, 20: 223-231.
- Day, S. M., Rimer, N. and Cherry, J. T., 1983. "Surface waves from underground explosions with spall: analysis of elastic and nonlinear source models," *Bull. Seismol. Soc. Amer.*, 73: 247-264.
- Day, S. M., Rimer, N., Cherry, J. T., and Stevens, J. L., 1982. "Nonlinear modeling of tectonic release from underground explosions," *S-Cubed Report*, SSS-R-82-5555, La Jolla, California.
- Jurkevics, A., 1986. "Use of polarization filtering to enhance depth phases in P-coda," this report.
- Jin, D. J. and Eisner, E., 1984. "A review of Homomorphic deconvolution," *Rev. Geophys. and Space Physics*, 22: 255-263.
- Kemerait, R. C. and Sutton, A. F., 1982. "A multidimensional approach to seismic event depth estimation," *Geoezploration*, 20: 113-130.

2.3. APPLICATION OF POLARIZATION PROCESSING TO NORESS AND RSTN RECORDINGS OF TWO EVENTS IN WEST KAZAKH S.S.R.

On October 27 and 28, 1985 (days 300 and 301) two events were reported, both with origin times 12:00:14 GMT on their respective days and located at 46.5N and 64.5E near the Aral Sea in West Kazakh S.S.R. The m_b of the first event was established as 4.35 from six stations worldwide, and the second one was at least .3 magnitude units smaller. These events were unusual, occurring in an aseismic region at 4 p.m. local time on successive days and having complex signatures on NORESS, which suggested the possibility that they might be multiple explosions.

This report describes the application of three-component polarization filtering to short-period recordings of these two events. The low signal-to-noise levels made clear identification of P phases difficult, and polarization filtering was applied in an attempt to isolate the energy polarized in the incident P-wave direction and improve the signal-to-noise level. Recordings were analyzed from two three-component instruments located at the NORESS array and at the RSTN stations RSSD, RSON, and RSNY. Several vertical recordings from NORSAR were also bandpass filtered and examined. The NORESS array was not operating at the time of the event on day 301 and no three-component instruments were operating during this period at NORSAR.

Due to the small magnitudes of these events, clear signals were observed above the background noise at the predicted P-wave arrival times only for the event on day 300 at station RSSD above 2 Hz and a few of the array beams at NORSAR. The polarization analysis indicated that the signal at RSSD is rectilinearly polarized in the near-vertical direction. The NORESS and NORSAR recordings showed a long, complicated wave train above the ambient noise for frequencies above 2 Hz. This wave train began shortly after the predicted P-wave time and continued on for at least two minutes. Polarization processing of the three-component NORESS records showed that this energy is mostly randomly polarized with several rectilinearly polarized bursts in the direction of the theoretical P-wave motion. The strongest rectilinear signal occurs more than 60 seconds after the P-wave arrival time. The event on day 301 was smaller than that on day 300 and did not have a signal significantly above the noise at any of the sites.

2.3.1. Polarization Filtering Algorithm

The algorithm used in the polarization processing has been described in detail by Jurkevics (1986). The underlying idea is to decompose each of the three orthogonal components of motion using a bank of narrow-band filters and short overlapping time windows. The polarization ellipse is then computed as a function of time in each passband. The time resolution or window length used is a function of frequency. The polarization analysis is carried out entirely in the time domain which obviates some of the spectral estimation problems encountered by frequency-domain methods.

Tests carried out to determine the behavior of the polarization filter under conditions of increasing random noise indicated that the algorithm performs very well until a signal-to-noise ratio of about two or four is reached. Increasing the noise level further quickly increases the variance of the polarization estimates. When the algorithm is applied to purely random uncorrelated noise on all three components, the noise does, occasionally, and at random instances, appear rectilinearly polarized in a given direction. This is because even random noise is correlated to some degree over the relatively short time windows used in the procedure. While using longer windows would help suppress the effects of noise, the time resolution of the filter would be lost since different seismic waves arriving at close intervals can have different polarization states. Thus, a compromise is necessary. This trade-off between resolution and variance is well understood, for example, in the field of spectral estimation. With regard to the two events analyzed in this report, the necessary signal-to-noise level for a stable estimate of signal polarization was achieved only in certain frequency bands and at certain stations. Of all the recordings analyzed, results will be shown only for those cases where the signals were sufficiently above the noise for the polarization processor to yield stable results.

2.3.2. Data Analysis

The NORESS array was in operation during the event on day 300 but not on day 301. NORSAR was operating both days but was not recording three components. The observed vertical signals at all the NORSAR sub-arrays, including NORESS, were similar except that the signals were stronger at some sites than others. *Figure 1* shows 180 seconds of short-period data at NORESS stations NRA0 and NRC7 for the event on day 300. The predicted P-wave arrival time is at 60 seconds. No instrument corrections or bandpass filtering have been applied in this case. Each trace has been scaled to its peak value, which is given on the right-hand side of the plot.

The polarization filter was set to pass rectilinear motion in the theoretical emergence direction of the direct P-wave. For the specified origin this phase should emerge at NORESS at an azimuth of approximately 289 degrees and apparent incidence angle of 32 degrees. The apparent incidence angle was determined using a Herrin 68 model (von Seggern and Marshall, 1982) and a distance of 33.5 degrees from the origin. *Figure 2* shows the polarization-filtered results for the event on day 300 at NRA0 and NRC7. The upper three traces are the zero-phase bandpass-filtered components of ground motion. The dominant feature in the filtered three-component seismograms is the long wave train following the predicted P-wave arrival and continuing on for at least two minutes. The polarization filtered output in the fourth trace shows several bursts of rectilinear P-wave motion at the theoretical orientation within this wave train. A careful examination of the polarized outputs for stations NRA0 and NRC7 shows that several of these bursts are correlated between the two stations. This implies that the particle-motion orientation within the wave train has some stationarity across the array. The strongest signal, however, occurs more than 60 seconds after the direct P-wave time.

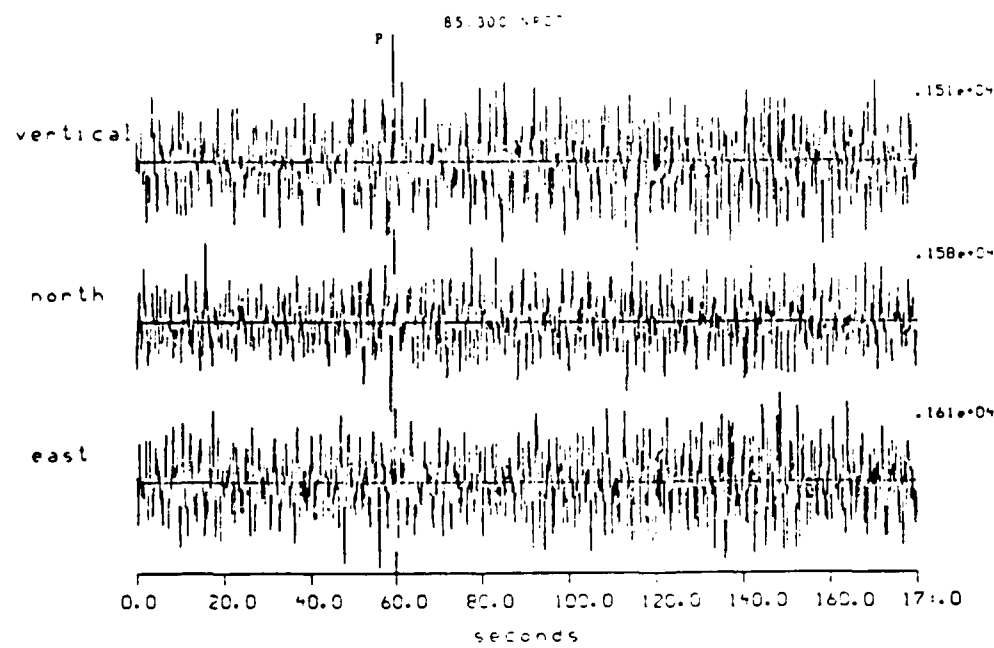
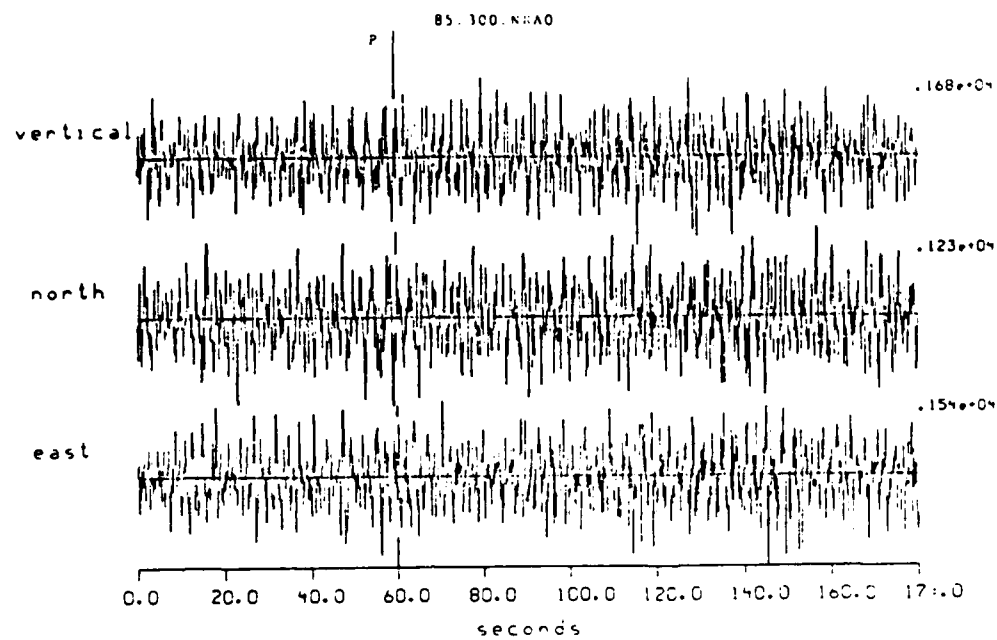


Figure 1. Three short-period components of motion recorded at the NORESS sites NRAO and NRC7 during the event on day 300. The predicted P-wave arrival time is at 60 seconds. These traces have been individually scaled with the peak amplitude of each trace given on the right side.

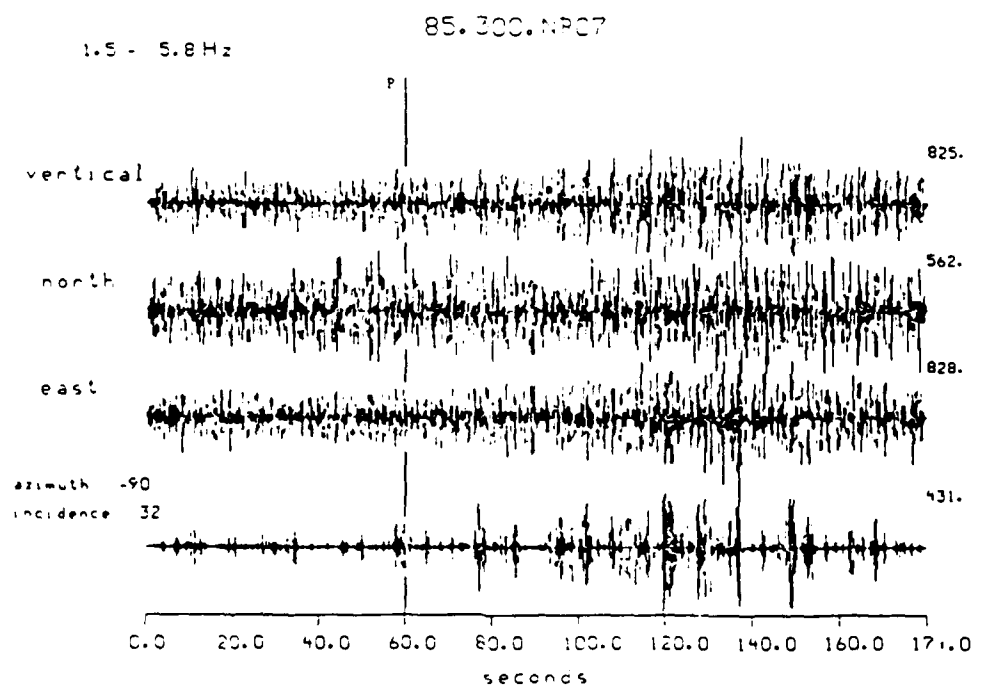
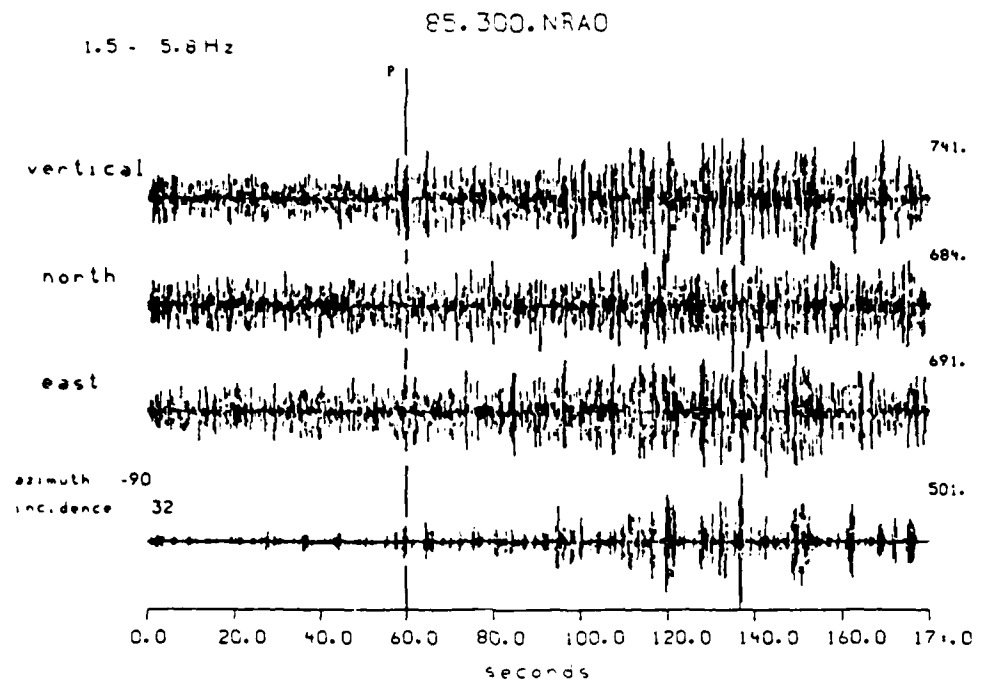


Figure 2. Polarization filtering applied to the event on day 300 at NRAO and NRC7 in the passband 1.5-5.8 Hz. The upper three traces are the input. The bottom trace shows energy polarized with an azimuth of -90 degrees and an apparent incidence angle of 32 degrees from vertical. This is the theoretical orientation of the direct P-wave.

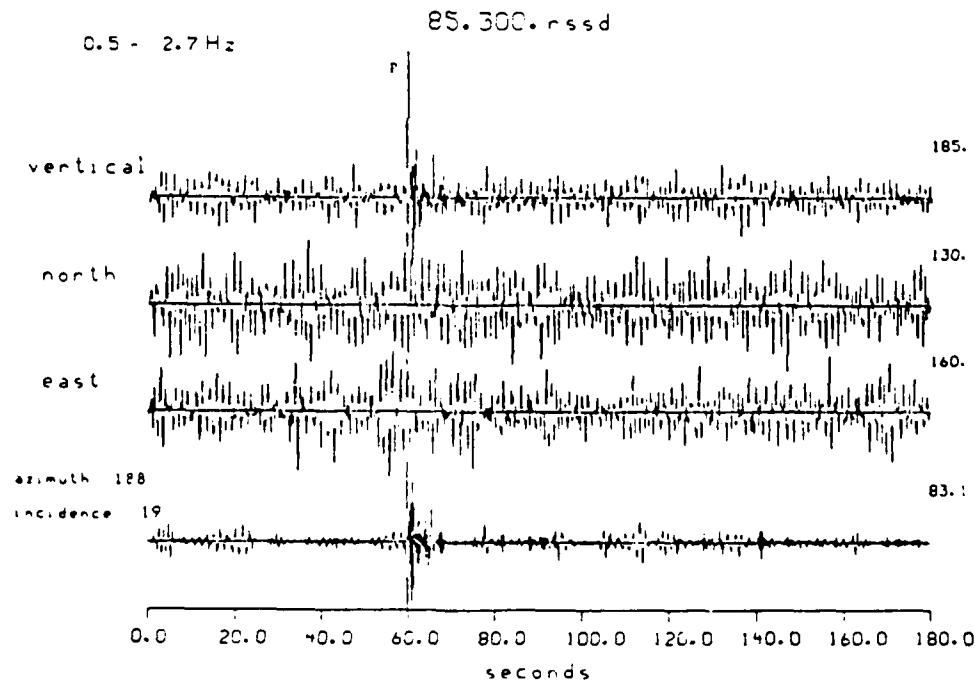
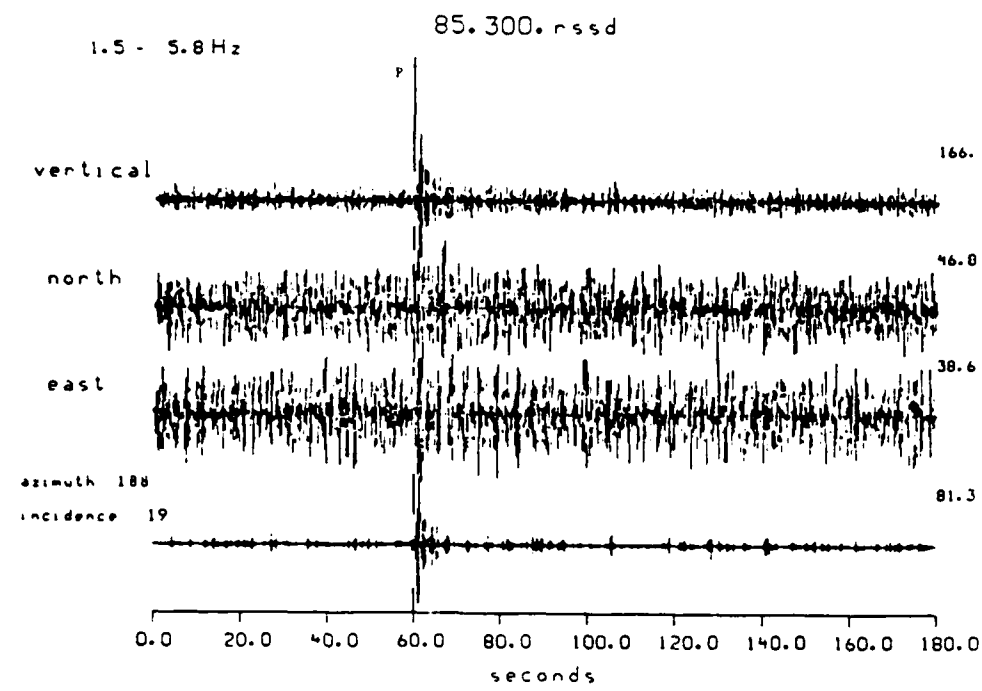


Figure 9. Polarization filtering applied to the event on day 300 recorded at RSSD in the passbands 1.5-5.8 Hz and 0.5-2.7 Hz. Outputs of polarization filtering are also shown. Energy rectilinearly polarized with an azimuth of 188 degrees and apparent incidence angle of 19 degrees is passed.

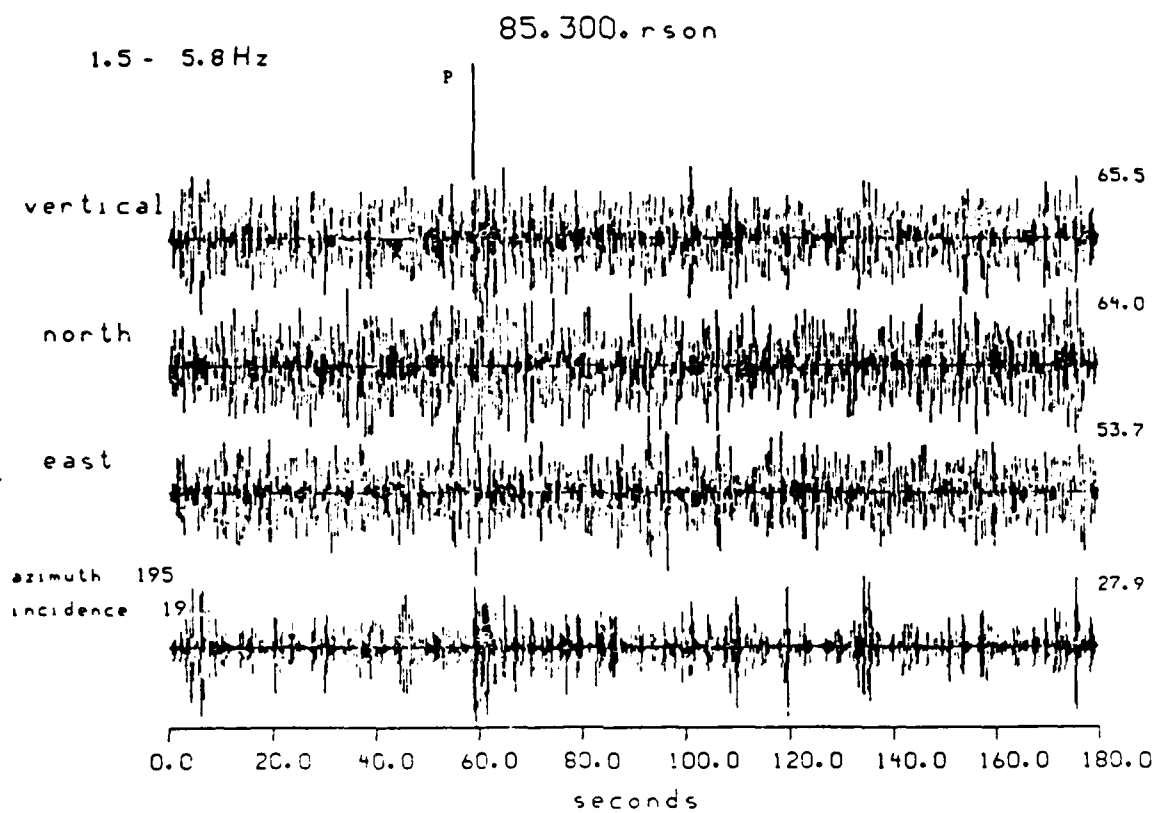


Figure 4. Polarization filtering applied to the short-period seismograms recorded at RSON during the event on day 300. The frequency band is 1.5-5.8 Hz. The signal is barely recognizable above the noise at the predicted arrival time. Polarization filtering shows this signal to be quite rectilinear, but the noise train also contains several bursts of apparently rectilinear particle motion.

On the RSTN network, clearly identifiable signals at the predicted P-wave times were present only for the event on day 300 recorded at RSSD and RSON. *Figure 3* shows band passed short-period components recorded at RSSD. The predicted P-wave arrival time is at 60 seconds. The results of polarization filtering within the passbands .5-2.7 and 1.5-5.8 are also shown in *Figure 3*. The theoretical azimuth of the P-wave motion is 188 degrees and the apparent incidence angle is 19 degrees. The lower frequencies at RSSD did not show a strong signal or any rectilinear polarization at the predicted P-wave time or following it. However, above 1.7 Hz there is a strongly polarized signal at the predicted time. This particle motion is rectilinear and almost vertical. *Figure 3* shows the filtered outputs with the rectilinear pass direction oriented in the theoretical incidence angle of 19 degrees. The filtered signal has a reduced amplitude due to the aperture function which passes motion, which is close to, but not exactly, in the pass orientation. The filtered coda decays to the noise level within ten seconds. Because of the near-vertical orientation of motion at RSSD, a reliable azimuth estimate is not possible from the data.

The results for station RSON are shown in *Figure 4*. There is only a hint of a signal at the predicted arrival time at RSON in the band 1.5-5.8 Hz. A distinct burst of rectilinearly polarized energy is apparent at the predicted arrival time of 60 seconds. However, the noise level is such that no other arrivals on this record can be clearly identified as P-waves.

2.3.3. Summary

Polarization filtering has been applied to three-component short-period recordings of two events on days 300 and 301 of 1985 located in West Kazakh S.S.R. Recordings of the event on day 300 at NORESS and NORSAR showed a long complicated wave train beginning at approximately the P-wave arrival time and continuing for at least 120 seconds. Polarization filtering was applied in order to determine the particle motion polarization of recordings of these events and enhance the signals by isolating rectilinearly polarized motion in the direct P-wave direction. In most cases, the signal-to-noise level was too low to clearly isolate polarized signals from noise. Results showed, however, that the event on day 300 recorded at RSSD contains a strongly-polarized signal at the predicted P-wave arrival time but not later in the coda. Analysis of NORESS recordings of the same event showed the long complicated wave train following the direct P-wave time to be randomly polarized with both time and frequency, with several bursts of energy polarized in the direction of the theoretical P-wave. This characteristic of the NORESS signals, together with the simple form of the RSSD signal, suggests that the signal at NORESS is not associated with a multiple source. This conclusion is based on the assumption that the dominant signal on the RSSD record in the band 1.5 - 5.5 Hz at the predicted time on day 300 is indeed the seismic signature of the event in question.

Andy Jurkevics

REFERENCES

Baumstark, R., provided the magnitude estimates and waveforms of these events.

Jurkevics, A., 1986. "A Polarization Processing Algorithm with Applications to RSTN Data" in *SAIC Quarterly Technical Reports for July-September and October-December 1985*, Technical Report C86-05.

von Seggern, D., and Marshall, M., 1982. "Definition of Seismic Signal Parameters by Particle Motion Processing," *Teledyne Geotech Report*, VSC-TR-82-10.

2.4. EXPANDED USE OF COMPUTERS IN REGIONAL SEISMIC DATA ANALYSIS

In the previous Quarterly Report (Technical Report C86-05) we outlined our motivation for incorporating heuristic and interpretational techniques in the automated analysis of regional seismic data. Basically, we wish to tap, and then apply, the type of knowledge and pattern recognition skills that an experienced data analyst develops after examining a vast amount of seismic data for a given seismic region or recording station. In this first application of our ideas, we have been concentrating on the analysis of regional events at the NORESS seismic array in southern Norway. NORESS is located near areas of active microseismicity (magnitudes less than 4.5) and frequent chemical explosions associated with mining operations. This situation provides us with the opportunity to study the differences in the waveforms produced by these two types of sources from the point of view of an analyst attempting identification of the source.

Experienced analysts are often able to discriminate between tectonic events and chemical explosions simply from experience. They recognize the signature of a waveform from a chemical explosion in a given area. However, their experience must inevitably be based on quantifiable differences in the seismic signatures of events. The analyst somehow "skips" this conscious quantification of the signals and simply proceeds from memory. Our goal here is to delve first into the quantification of the signals for a specific suite of events, then to the clustering of our quantifications, and finally to the development of classification "rules" which could then be automatically applied by a computer to new data from the same source area.

For this study, we have selected two sets of events for comparison and classification. The first is a set of chemical explosions from the Titania Mine in southern Norway. The second is a set of presumed earthquakes off the western coast of southern Norway. The events from both areas are all of similar magnitude (2.0 to 2.5) and the distances to the NORESS array are approximately 3.7 degrees in both cases. Focal depth information for the tectonic events is not currently available.

Figure 1 shows two short-period vertical seismograms recorded at NORESS site A0. The seismograms have been bandpass filtered between 8 and 16 Hz. The upper seismogram is for an earthquake from our dataset and the lower seismogram is for a chemical explosion at the Titania Mine. Analysts often look at this frequency band when discriminating between earthquakes and explosions, drawing on the experience that explosions commonly produce seismograms of higher frequency than natural events. Since the data are highly compressed in these figures, differences in the frequency content are not readily apparent, but the envelopes of the data do show differences. In particular, the earthquake is devoid of Lg waves in this frequency band. And the character of the Pn waves is also somewhat different. The Pn waves for the earthquake appear to arrive in one group, whereas, the Pn waves for the chemical explosion arrive and then decay in a long coda. Let us take a closer look at the Pn waves generated by these two events.

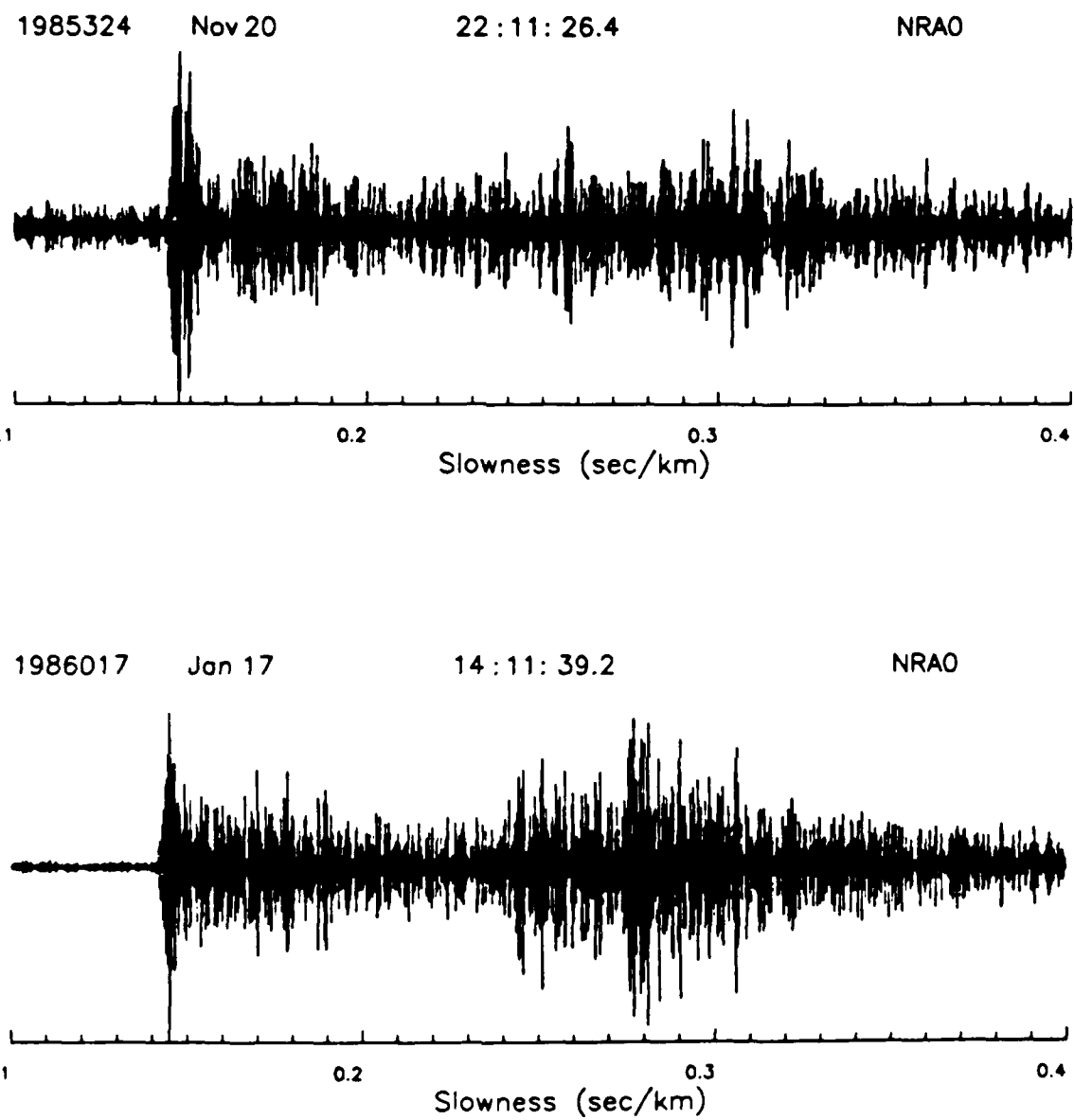


Figure 1. NORESS seismograms for an earthquake off the coast of southern Norway (upper trace) and for a chemical explosion at the Titania Mine (lower trace). The seismograms have been bandpass filtered between 8 and 16 Hz.

Figure 2 shows nine second windows of the Pn waveforms. Cursory examination shows that the predominant frequency of the Pn for the tectonic earthquake is lower than that of the Pn for the chemical explosion. We now need a way of emphasizing the differences in these two Pn signals and testing whether or not the differences are consistent for other events. Clearly, we have to start with a spectral representation of the signals.

Seismologists tend to display seismic spectra in terms of the logarithm of the ground displacement versus the logarithm of frequency, the so-called Brune spectral representation. Of course, this is because the Brune spectra emphasizes the three most widely quoted spectral source parameters: the seismic moment (proportional to the low frequency, flat portion of the spectrum), the corner frequency (indicative of the source duration), and the high frequency decay (generally proportional to f^{-2} or f^{-3}). (Spectral smoothing is also often applied.) This type of representation compresses, or de-emphasizes the variations in the spectrum in order to facilitate the determination of the three source parameters. However, in our case, we are not concerned with the Brune source parameters but are interested in emphasizing the peak spectral contributions to the seismic signal, including spectral peaks that may result from the specific path from the source area to the NORESS array. To accomplish this task, we will examine the seismic spectrum in terms of linear velocity power versus linear frequency. Working in the velocity domain allows us to examine what the human analyst actually sees on a seismogram, since the NORESS (and most short-period) instruments are essentially velocity sensors at high frequencies. It will also eliminate the artificial buildup of low frequency contributions to the spectra as would happen when one integrates from velocity to displacement. The use of the power rather than the amplitude serves to emphasize the peak spectral contributions (i.e., observable contributions) to the signal. And working in the linear domain serves the purpose of easily displaying these peak spectral contributions.

All of the signals and power spectra shown in this report have been high pass filtered above 2.0 Hz. The short period data recorded at NORESS is particularly noisy below 2 Hz. *Figure 3* shows the velocity power spectrum for a 5.0 second interval of noise at site A0 on November 8, 1985. The character of this noise sample is very typical for all of the days examined so far in this study.

Figure 4 shows the power spectra for the Pn waves shown in *Figure 2*. The power spectral representation shows that the earthquake has a spectral peak near 4 Hz, with additional smaller peaks near 7 and 10 Hz. On the other hand, the chemical explosion is devoid of the 4 Hz spectral peak, and has most of its power between 5 and 9 Hz. The differences in the power spectra for these events could be due to a number of factors, including both source and path effects. One explanation would be the shorter source time function for the chemical explosions. This would result in a higher corner frequency, which in a simplified representation of the source spectrum would show up as the peak in our power spectra. Path effects could also play a role, including the effect of presumably greater focal depth for the tectonic events.

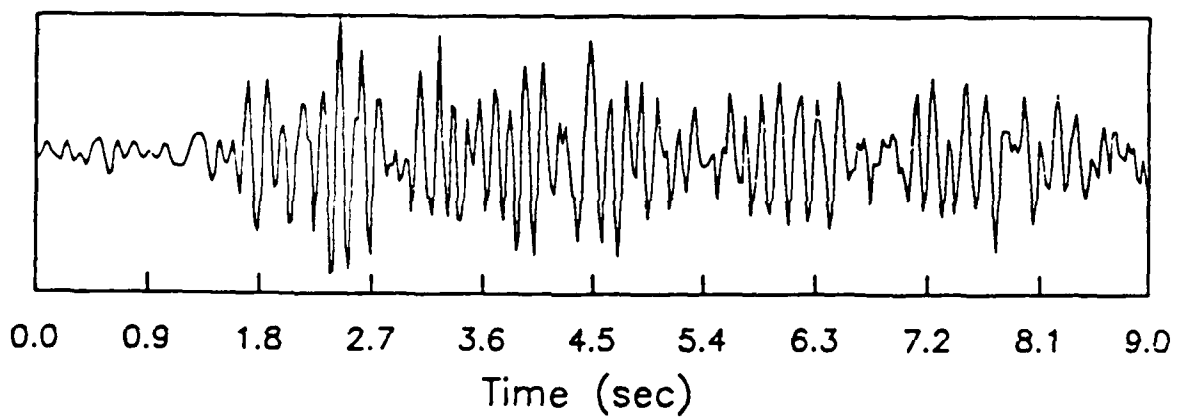
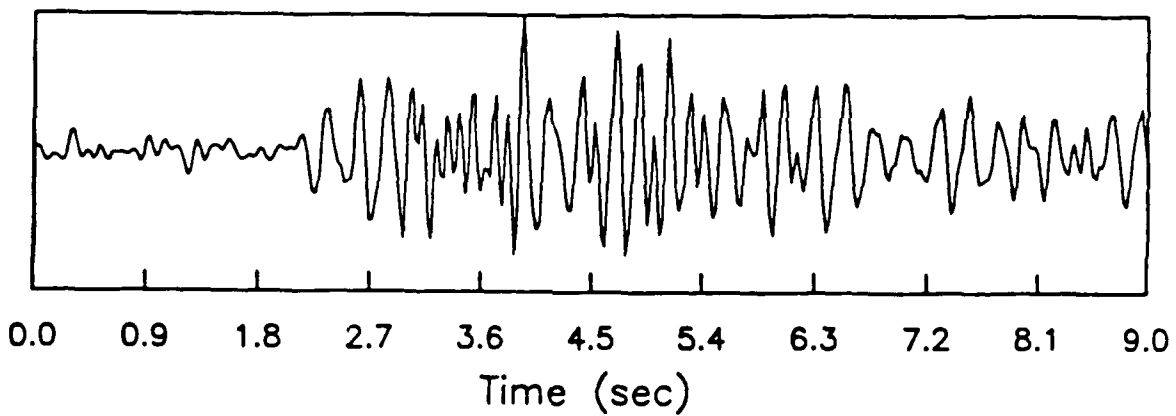


Figure 2. Pn waveforms from an earthquake (upper trace) and a chemical explosion (lower trace).

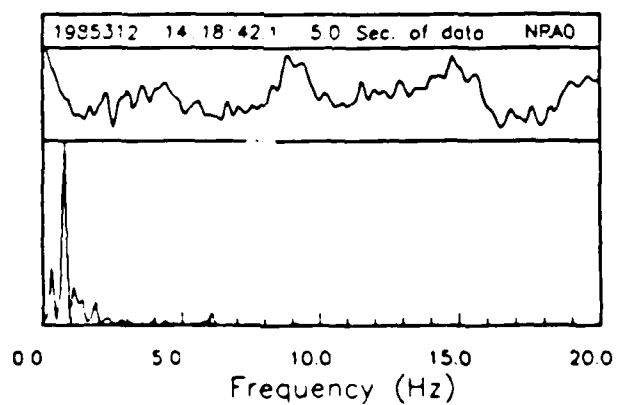


Figure 3. Typical power spectrum of noise at NORESS.

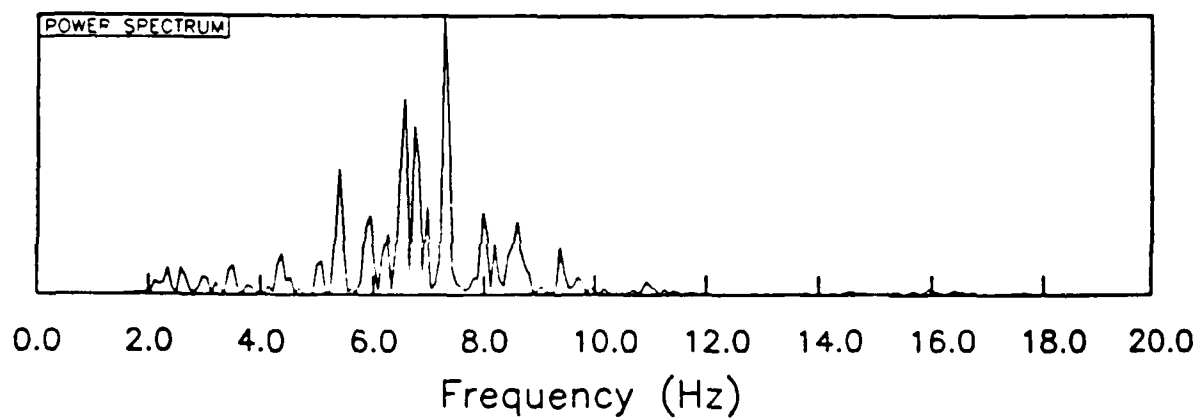
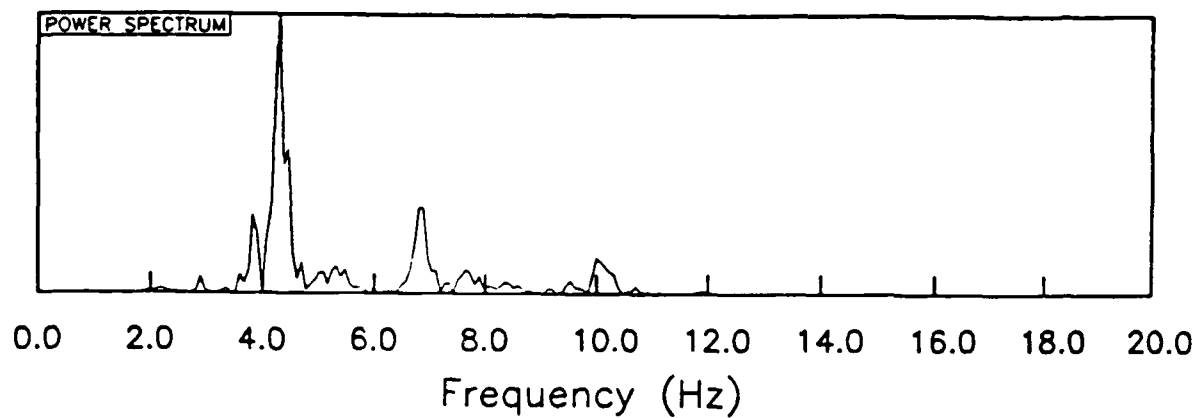


Figure 4. Corresponding power spectra for the Pn waveforms shown in Figure 2. Earthquake (upper spectrum) and chemical explosion (lower spectrum).

Is this observed difference between the power spectra of Pn waves for this earthquake and chemical explosion a common feature for all events in these two source areas? To answer this question, we have analyzed a dataset consisting of eight earthquakes from the off-shore area and seven chemical explosions from the Titania Mine. The Pn power spectra for the earthquakes are shown in *Figure 5* and the Pn power spectra for the chemical explosions are shown in *Figure 6*.

Although there are some differences among the power spectra for the earthquakes, all of the events have spectral peaks at 4 Hz, while some of them have additional spectral peaks at 7 and 9 Hz. The chemical explosions show a greater variation in power spectra; however, a feature which is common to all the events is the absence of the spectral peak at 4 Hz. Peak power for the chemical explosions occurs between 5 and 15 Hz. These differences in the power spectra of the Pn waves thus appears to be remarkably consistent for the dataset analyzed here.

Based on these observations, we can now go on to propose two waveform "rules" which apply to the earthquakes and Titania Mine explosions studied here. These rules would be used in addition to rules based on array measurements of apparent slowness, azimuth of approach, and Lg-Pn arrival times.

- The power spectra of Pn waves generated by the earthquakes have a primary spectral contribution (i.e., at least 40% of the peak power) at 4 Hz. The earthquakes may or may not have additional spectral contributions above 4 Hz.
- The power spectra of Pn waves generated by chemical explosions at the Titania Mine do not have a primary spectral contribution at 4 Hz. The explosions have primary spectral contributions above 4 Hz.

Thus, when incorporated into an operational procedure, the above "rules" could be applied after detection and location within their respective areas of applicability. If these observed differences in the Pn power spectra could be confirmed over a wider range of source magnitudes, the differences may prove to be a useful discriminant. Resolution of contributions from the source and path could be determined if there were an area with comparable sized earthquakes and chemical explosions at nearby locations.

Given the above "rules," we must now devise a way to automate their application. To do this, we first need to develop a "fingerprint" or other representation of the power spectrum of a reference earthquake and chemical explosion, as well as for an event in question. Although we have not yet tested an automated procedure, a method under consideration is to discretize the power spectrum of an event in question into cells. Each cell would be 0.1 or 0.2 Hz wide, and associated with each cell would be the power within the cell, referenced to some minimum. Such a minimum level could be the 40% of peak power level, mentioned above. For the earthquake in *Figure 2*, such a fingerprint would consist of the value 1.0 associated with the cell at 4.3 Hz. The power spectra of an event in question could then be simply searched for the value in this cell. For an event previously identified as originating from the Titania Mine area, an absence of the cell would be indicative

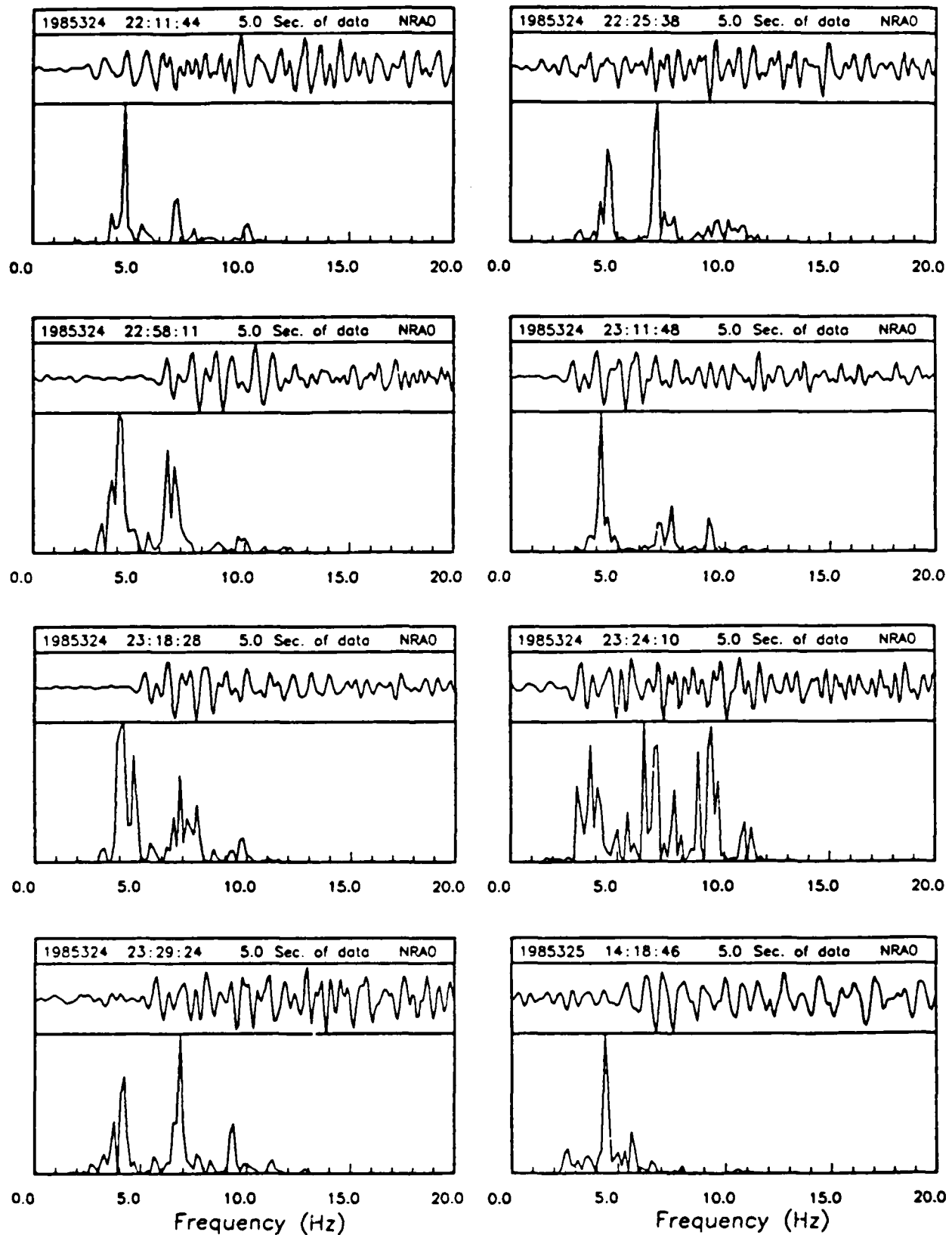


Figure 5. Pn waveforms and power spectra for earthquakes recorded at NORESS.

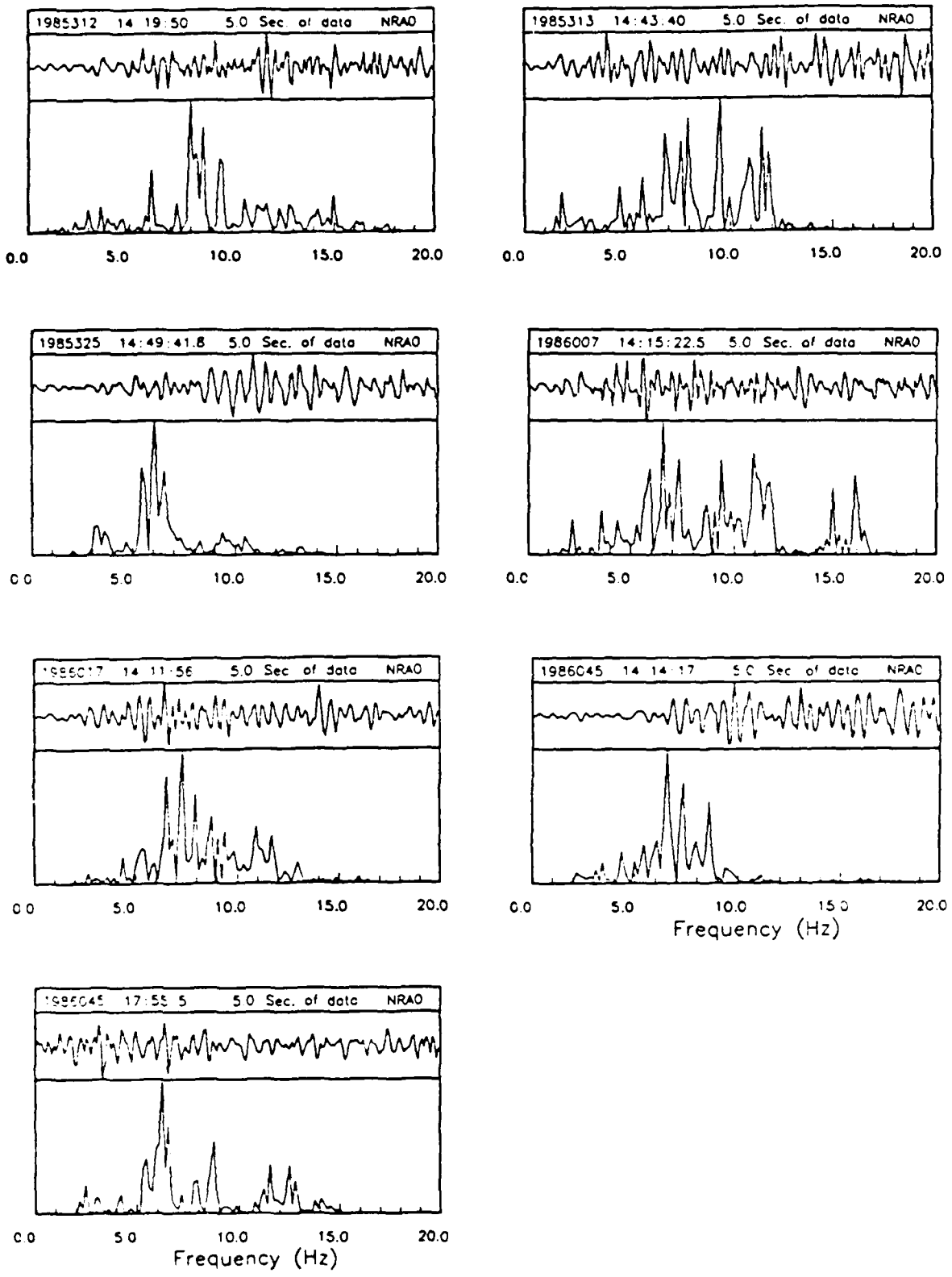


Figure 6. Pn waveforms and power spectra for Titania Mine blasts recorded at NORESS.

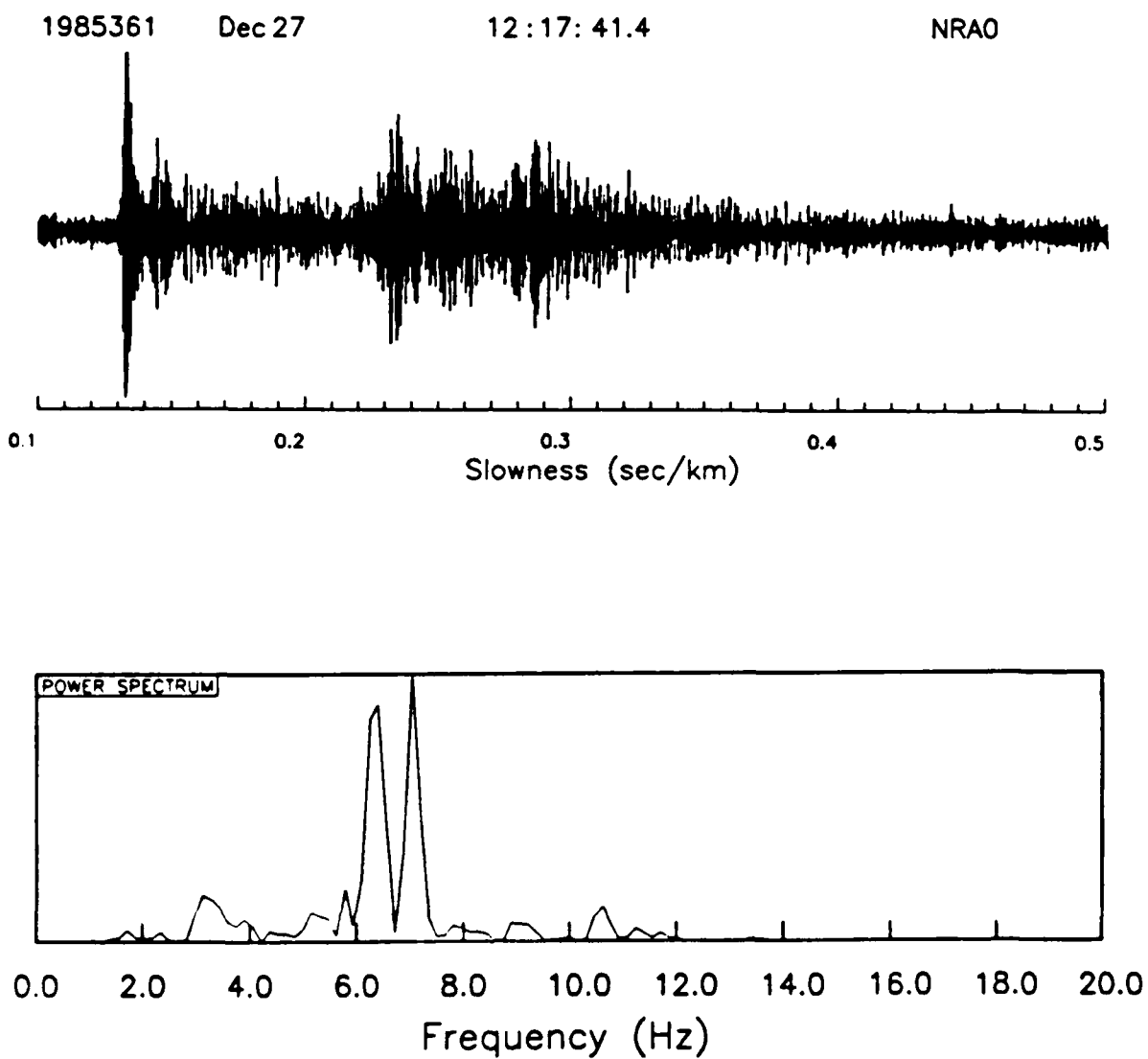


Figure 7. NORESS seismogram for mine E8 in Estonia, western Soviet Union. The Pn power spectrum for this event is shown in the lower figure.

of a chemical explosion. This method is similar to the one used to automatically interpret mass spectrograms in the field of chemistry. Certainly, this represents a highly simplified version of a discriminant, and more detailed fingerprinting and comparisons would likely need to be made. However, the results to date do hold promise for the application of interpretational methods to regional seismology.

Since the character of regional seismic phases is highly dependent on path effects, there will likely be a specific set of observational "rules" for each source-to-receiver path. As an example of a chemical explosion in a different source region and at a greater epicentral distance, we have examined an event identified by the University of Helsinki Institute of Seismology as a blast at Mine E8 in Estonia, western USSR, recorded at NORESS on December 27, 1985. The epicentral distance of this event is 8.6 degrees. The seismogram is shown in *Figure 7*. Within the passband of this plot (4 to 8 Hz), the Pn wave is very clear. The power spectrum for 5.0 seconds of the Pn wave is also shown in *Figure 7*. Note that there is minimal spectral contribution at 4 Hz, and primary spectral contribution at 6.3 and 7.0 Hz. The power spectrum for this event is thus very similar to those of the Titania Mine explosions shown earlier. Whether or not we are observing distinct characteristic features of the power spectra of chemical explosions remains to be seen. As more data are accumulated for this and other areas, we will continue to search for distinct features of waveforms with the goal of developing an automated system for recognizing seismic events from a given source region.

Jay J. Pulli

3. NETWORK CAPABILITY AND DESIGN

3.1. NOTE ON EARTHQUAKE DETECTABILITY: RADIATION PATTERN EFFECTS

3.1.1. Introduction

The earthquake detection capability of a network of seismological stations is often estimated by the so-called "Networth" method. This method usually assumes that the energy radiated from the earthquake focus is isotropic, i.e., the emitted amplitudes are independent of the direction to the seismological stations. Nevertheless, recorded amplitudes of teleseismic P-waves vary considerably, even if corrected for geometrical spreading and average path attenuation, but this variation is usually attributed primarily to local station effects.

In this note, an attempt is made to correlate radiation pattern effects with variation in amplitude measurements at a global station network.

3.1.2. Radiation of P-Wave Amplitudes

Measurements of short period P-wave amplitudes in the teleseismic distance range are analyzed below in terms of a simple standard model for a double couple source. The unit slip vector, the normal to the fault plane, and the direction of radiation are denoted: \mathbf{u} , \mathbf{n} , and \mathbf{d} , respectively. The radiated normalized amplitude can then be written as:

$$A(\mathbf{u}, \mathbf{n}, \mathbf{d}) = |(\mathbf{d} \cdot \mathbf{n})(\mathbf{d} \cdot \mathbf{u})|$$

The mean and standard deviation of the radiated amplitudes can be calculated assuming that the focal sphere is sampled uniformly. With $\mathbf{u}=(1,0,0)$, $\mathbf{n}=(0,0,1)$, and writing the direction of radiation, \mathbf{d} , in polar coordinates with the angles, θ and ϕ , the amplitude becomes:

$$A(\theta, \phi) = |\sin(2\theta)\cos(\phi)|$$

Integration gives the mean amplitude, $E(A)$, and variance, $V(A)$:

$$E(A) = 4/(3\pi)$$

and

$$V(A) = 4/15 - (4/(3\pi))^2$$

Usually it is assumed that the recorded amplitudes follow a log normal distribution, i.e., $\alpha = \ln(A)$ is normally distributed with mean m and standard deviation σ . The standard deviation of this log normal distribution can be derived from, for example, the moment generating function, $M(t)$, which is equal to:

$$M(t) = E(e^{t\alpha}) = e^{mt + \sigma t^2/2}$$

with the argument t . This gives:

$$E(A) = E(e^\alpha) = e^{m + \sigma^2/2}$$

and

$$E(A^2) = E(e^{2\alpha}) = E^2(A) \cdot e^{\sigma^2}$$

and the following expression is obtained for σ :

$$\sigma = \ln(1 + V(A)/E^2(A))$$

One gets a σ value of 0.27 using the values above for $E(A)$ and $D(A)$ for a 10 base logarithm, i.e., $\log_{10}(A) = \alpha \log_{10}(e)$.

In practice the focal sphere cannot be sampled uniformly, but on a rather limited portion, and the standard deviation obtained here is probably larger than for a non-uniform sampling.

3.1.3. Amplitude/Period Data

The data analyzed here consist of amplitude/period ratios obtained at globally distributed stations from earthquakes in the Lake Baykal region between 1971-1980. The data have been extracted from the monthly bulletins of the ISC, and ratios have been used from in all 46 events; the geographical distribution of which is shown in *Figure 1*. The events are fairly uniformly distributed along a 100-200 km wide zone, which has an extension of about 700 km.

The Lake Baykal area was selected because of stationarity in earthquake sources over the time period considered here.

The magnitude range of the earthquakes is less than one magnitude unit, and since the data are moreover limited to a small region, it is felt that the wave periods have little influence on the amplitude/period ratios.

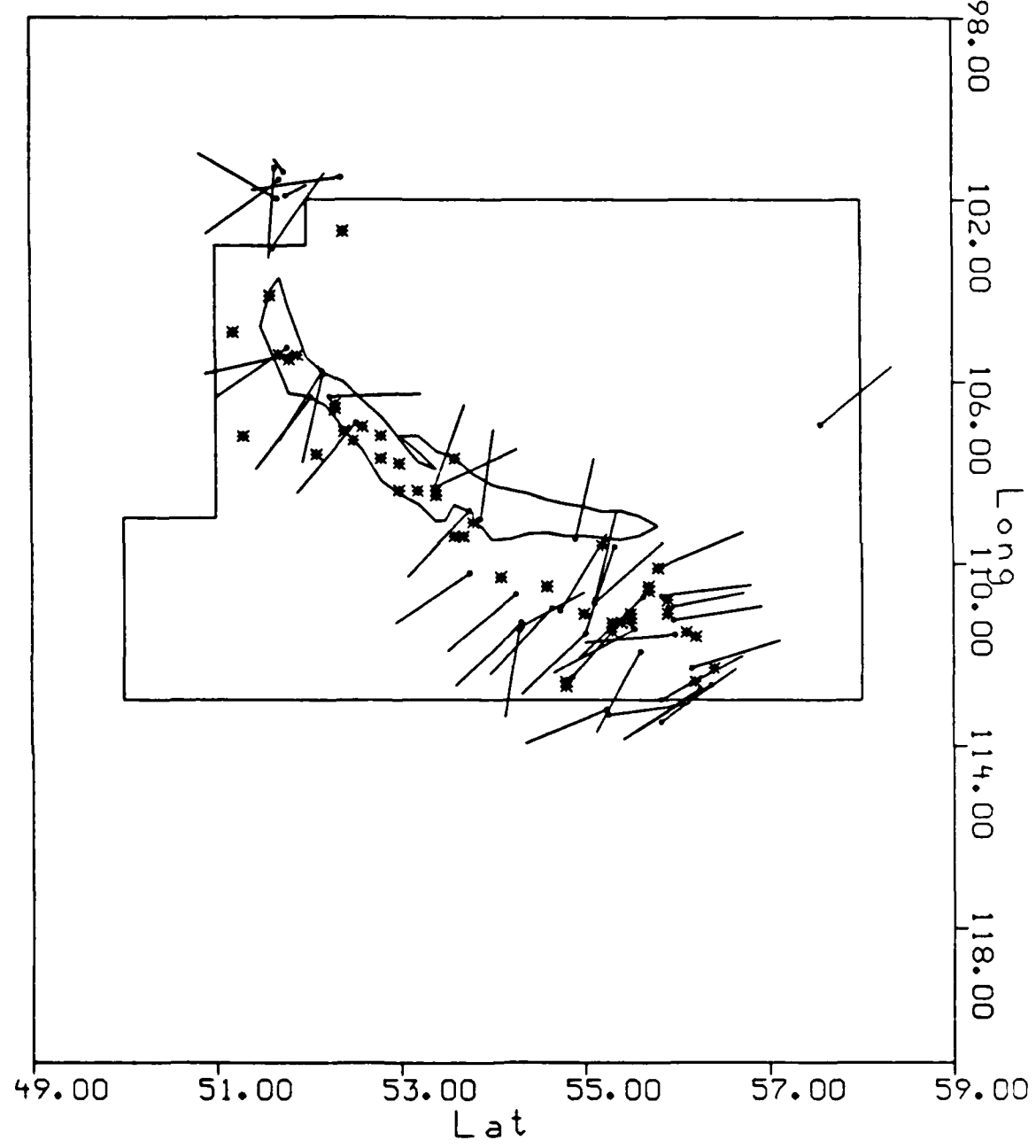


Figure 1. The geographical distribution of earthquakes, indicated by asterisks, the amplitude/period data of which is analyzed here. The lines are projections of tensional stress axes of groups of earthquakes, the centers of which are indicated by dots.

The location of the stations for which measurements have been used, relative to the Lake Baykal region, is shown in *Figure 2*. Although there are seismological stations in all quadrants as seen from the Lake Baykal region, there is a heavy concentration in the Northwesterly and Northeasterly directions, which correspond to Europe and North America, respectively. Stations in these directions taken together, however, provide a fairly dense coverage in a 90 degree azimuthal sector. It can be noted that the radiation pattern has a 90 degree symmetry.

3.1.4. Station Corrections

It is assumed that the logarithm of the amplitude/period ratio, r_{ij} , at station j for event i can be written as:

$$m_{ij} = r_{ij} + B(\Delta_{ij})$$

where $B(\Delta_{ij})$ is the amplitude distance correction (Gutenberg-Richter correction is used here). The station magnitude is then defined as:

$$m_{ij} = m_i + s_j$$

where m_i is the event magnitude and the term s_j is a station correction.

A least squares solution was obtained for the equations above assuming that $\sum s_j = 0$ and resulting estimates of s_j for 40 stations are listed in Table I. The estimated uncertainties, (σ_j) , are also given in the table and they reflect largely the number of observations available for each station. Only events with at least two observations of the amplitude/period ratio and stations with at least three measurements were used in the computations. The solutions were obtained for 266 observations, 32 events, and 40 stations. No truncation of the data was made.

Many of the stations listed in Table I have been included in earlier studies on station magnitude bias (Ringdal, 1984; North, 1977). Values obtained by Ringdal and North are included in Table I for comparison. Estimates in such studies were obtained from a global distribution of earthquakes with a view of removing possible source effects. That is to say that the station corrections, s_j , relate to local station effects only, whereas the corrections obtained here could also include source effects related specifically to the Lake Baykal region.

Comparisons between station corrections are made in *Figure 9*, which compares the estimates by North with those of Ringdal as well as the estimates obtained here with those of Ringdal. The values in the figure have been normalized so that the mean values for the two sets are both equal to zero. The estimates by North and by Ringdal are based on the order of several hundred thousand station m_b values, whereas the estimates for Lake Baykal here are based on 200 station magnitude values.

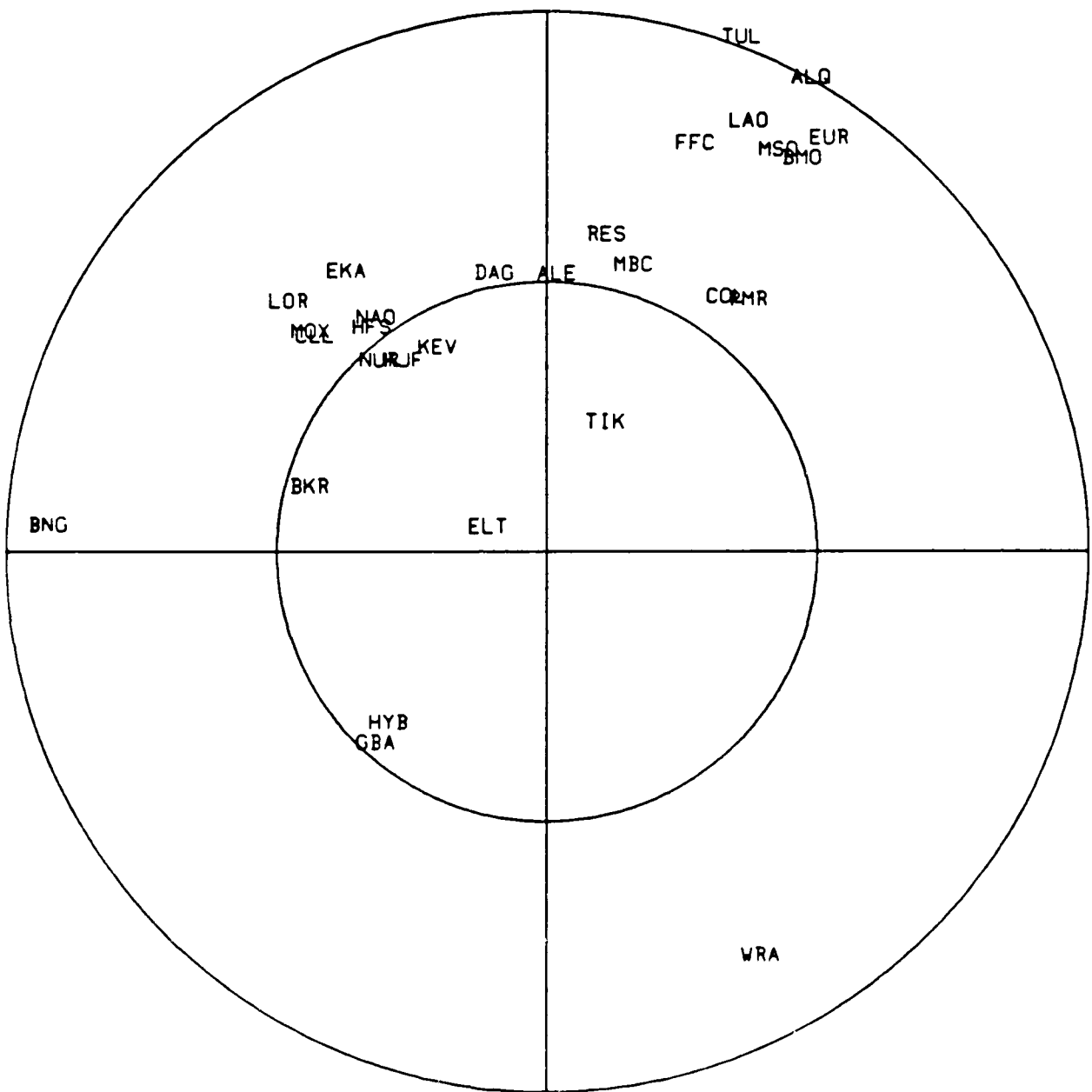


Figure 2. Geographical distribution of stations relative the Lake Baykal region. The circles indicated epicentral distances of 45 and 90 degrees respectively.

TABLE I. COMPARISON OF STATION CORRECTIONS

Station Code	Lake Baykal Mean	Global Ringdal Std.	Global North
ALE	-0.20	0.10	-0.04
ALQ	0.04	0.08	-0.20
BKR	0.32	0.12	0.38
BMO	0.02	0.09	-0.28
BNG	-0.16	0.14	0.01
BRG	0.05	0.12	-0.11
CLL	0.10	0.12	0.20
COL	0.23	0.06	0.01
DAG	0.22	0.09	-0.02
EKA	-0.01	0.13	0.00
ELT	0.22	0.09	0.15
EUR	-0.45	0.11	-0.24
FBA	0.39	0.09	
FFC	-0.09	0.13	0.08
GBA	-0.07	0.12	0.04
GIL	0.29	0.15	-0.04
HFS	0.08	0.06	0.05
HYB	0.04	0.12	0.19
KEV	-0.15	0.10	0.02
KJF	-0.08	0.07	0.09
LAO	-0.21	0.09	-0.10
LBF	-0.30	0.14	
LOR	-0.15	0.11	0.06
MAIO	-0.17	0.14	-0.11
MBC	-0.01	0.07	0.14
MOX	-0.01	0.09	0.02
MSO	0.16	0.09	-0.06
NAO	-0.15	0.08	-0.10
NB2	-0.34	0.13	
NUR	0.01	0.14	0.19
NVS	-0.44	0.13	
PMR	-0.27	0.12	-0.08
RES	-0.11	0.08	0.13
SEY	0.23	0.14	
SLL	0.08	0.14	
SSF	-0.16	0.12	
TIK	-0.17	0.11	0.03
TLG	-0.71	0.14	
TUL	0.25	0.10	0.21
WRA	-0.21	0.08	-0.20

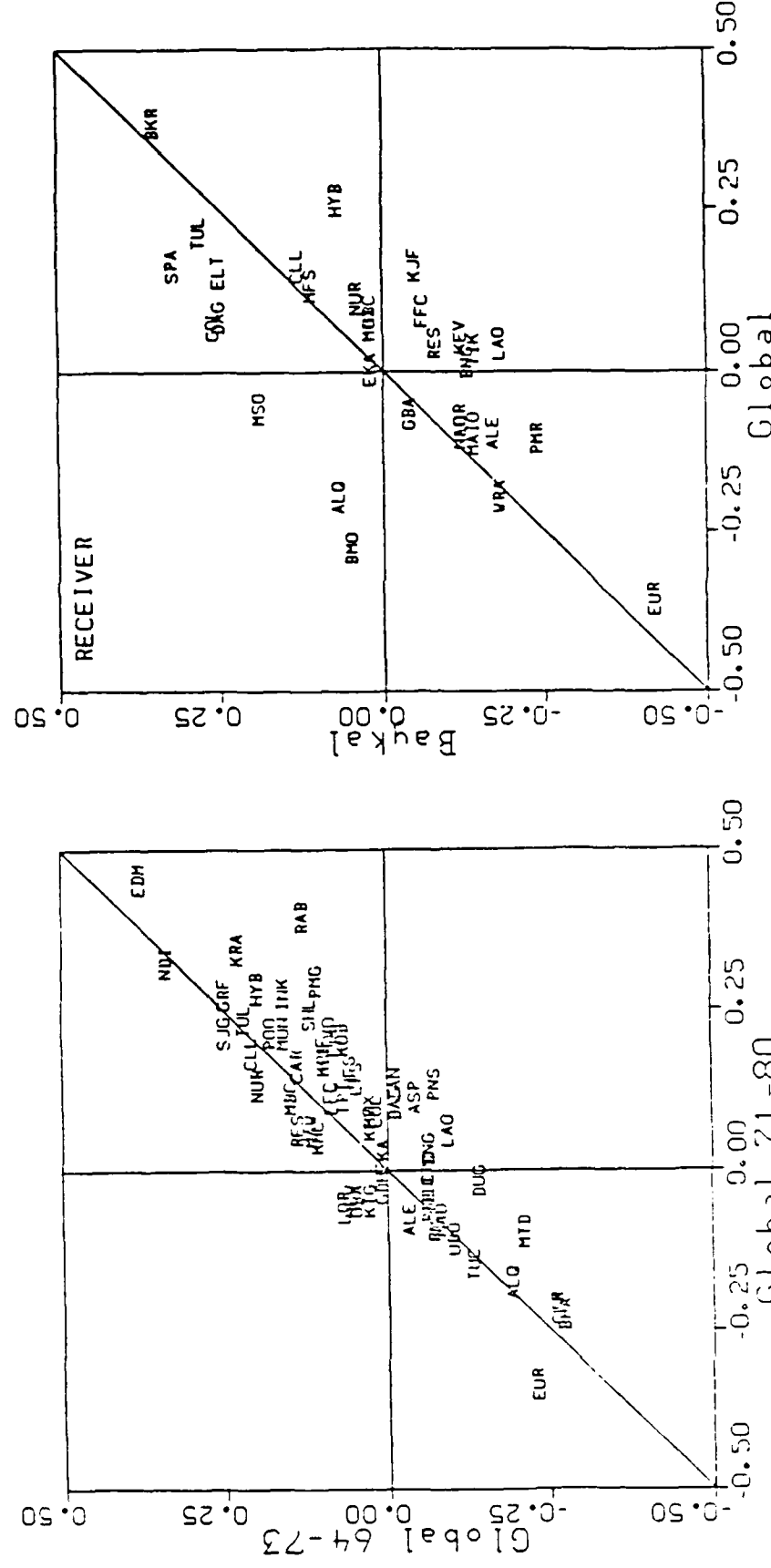


Figure 3. Comparison of station magnitudes corrections. The diagram to the left compares estimates based on a global distribution of earthquakes as reported by the ISC for the time periods 1964-1973 and 1971-1980. The diagram to the right compares the estimates obtained for the Lake Dayakal region with those based on ISC data for 1971-1980.

The estimates of North and of Ringdal are quite consistent and are based on largely independent data with about 30% overlapping. The standard deviation of the difference between the two estimates for 59 common stations is 0.08.

The estimates obtained for the Lake Baykal are also in reasonable agreement with those of Ringdal as can be seen from *Figure 3*. Apart from the general agreement there are also, however, some stations (e.g., BMO, ALQ, COL, and MSO) that are significantly different. Attempts are made below to correlate these differences with source radiation pattern effects.

3.1.5. Mechanism Determinations in Lake Baykal

Estimates of focal mechanisms have not been published for any of the earthquakes, for which amplitude/period data are analyzed here. However, mechanisms have been estimated for a number of earlier occurring moderate and strong events ($M \geq 5$) in the Baykal region as well as for a number of groups of weaker events ($K \leq 9$) with consistent results (Misharina, 1979).

Broadly speaking, the mechanisms are characterized by near vertical axes of compressional stress, and near horizontal orientation of tensile axes, mainly perpendicular to the strike of surface structures of the Baykal Rift zone.

The orientation of stress-axes of small earthquakes have been determined from groups of small events because of the sparsity of the local network. This method assumes stationarity of mechanisms over a limited volume in the crust. *Figure 1* shows the directions of tensile axes projected on the earth's surface for 50 groups of small magnitude earthquakes covering the area considered here. Data from, in all, about 1000 earthquakes were used to obtain the results summarized in the figure (Misharina, 1979).

The dominant mechanism with near vertical compressional axis implies that the radiated amplitudes would largely be dependent on the epicentral distance and the larger the distance the larger the amplitude.

3.1.6. Calculated Source Corrections

Radiated P-wave amplitudes can be calculated from directions of compressional (c) and tensional (t) axes estimated for an earthquake of earthquake group using the relations:

$$u = \frac{1}{\sqrt{2}} c + \frac{1}{\sqrt{2}} t$$

$$n = \frac{-1}{\sqrt{2}} c + \frac{1}{\sqrt{2}} t$$

and the formula for the amplitude, A, in Section 2 above.

The direction of radiation (d) for a given station is obtained from the source station azimuth and the take-off angle. The take-off angle is obtained here from the simple formula in standard notations:

$$\sin(i) = \frac{dT}{d\Delta} \cdot \frac{v}{r}$$

Jeffrey-Bullen's travel time model was used to obtain the slowness. The value of the velocity (6.25 km/s) was obtained from a velocity-depth curve for the crust (Olsen, 1983) at the average depth of earthquakes (around 12.5 km) in the Lake Baykal region. The selection of velocity value is illustrated in *Figure 4*, which shows the depth distribution of earthquakes and that the mean focal depth coincides with a shallow low velocity zone derived from crustal profiling.

The following procedure was applied to calculate average radiated P-wave amplitudes for the stations. For a given event, for which sufficient amplitude/period ratio data were available, closely (within 0.5 degrees) located groups of events, for which stress axes had earlier been estimated, (Misharina, 1979) were identified. The map in *Figure 1* compares the epicentral distributions for the earthquakes and the groups of small events. P-wave amplitudes were calculated (transformed to a logarithmic scale) using the directions of stress axes for stations that reported amplitude/period data for the given event. An average value was then formed for each station. Total average values were formed for each station over the events. These station averages were normalized so that their average became equal to zero, and these normalized averages can be considered as calculated source-station corrections, c_j . A standard deviation was calculated along with each individual source-station correction.

3.1.7. Statistical Testing

Assuming that the station corrections determined on a basis of globally distributed events, $s_j(G)$, represent local station effects only, and that station corrections estimated from Lake Baykal events, $s_j(B)$, represent local station effects as well as source effects; the difference: $s_j(B) - s_j(G)$, should correlate with the calculated source corrections, c_j .

The data for 27 stations in the scatter diagram in *Figure 5* show little correlation between c_j and the difference $s_j(B) - s_j(G)$. If the stations LAO, HYB, RES, BNG, FFC, and PMR in the lower right part of the diagram were disregarded a clear correlation can, however, be noted. The following simplified chi-squared testing has been applied to the data in *Figure 5* to quantify these conclusions.

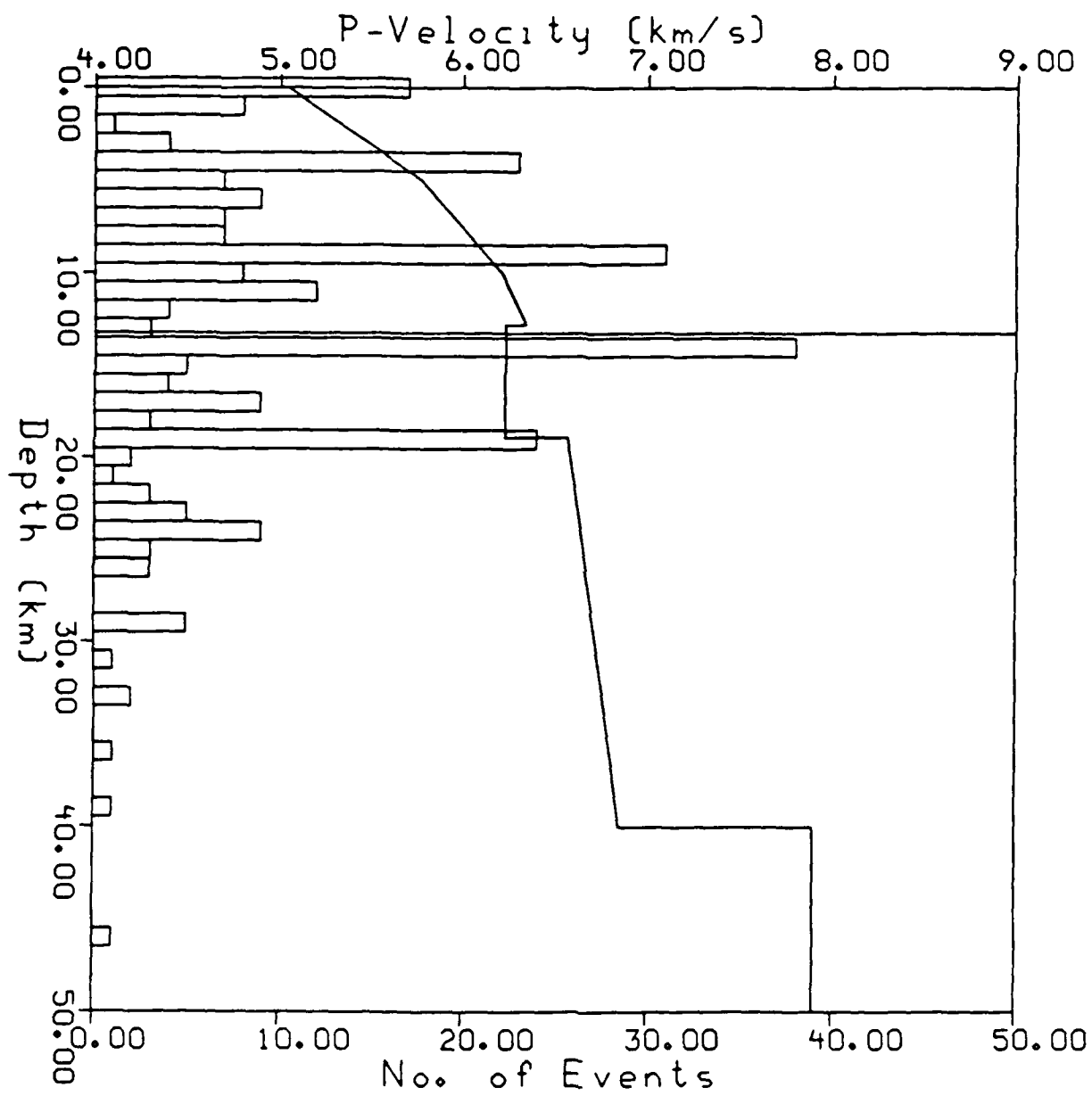


Figure 4. The bars show the distribution of earthquake depth for the Lake Baykal region. The curve outlines the P-wave velocity as a function of depth obtained from crustal profiling.

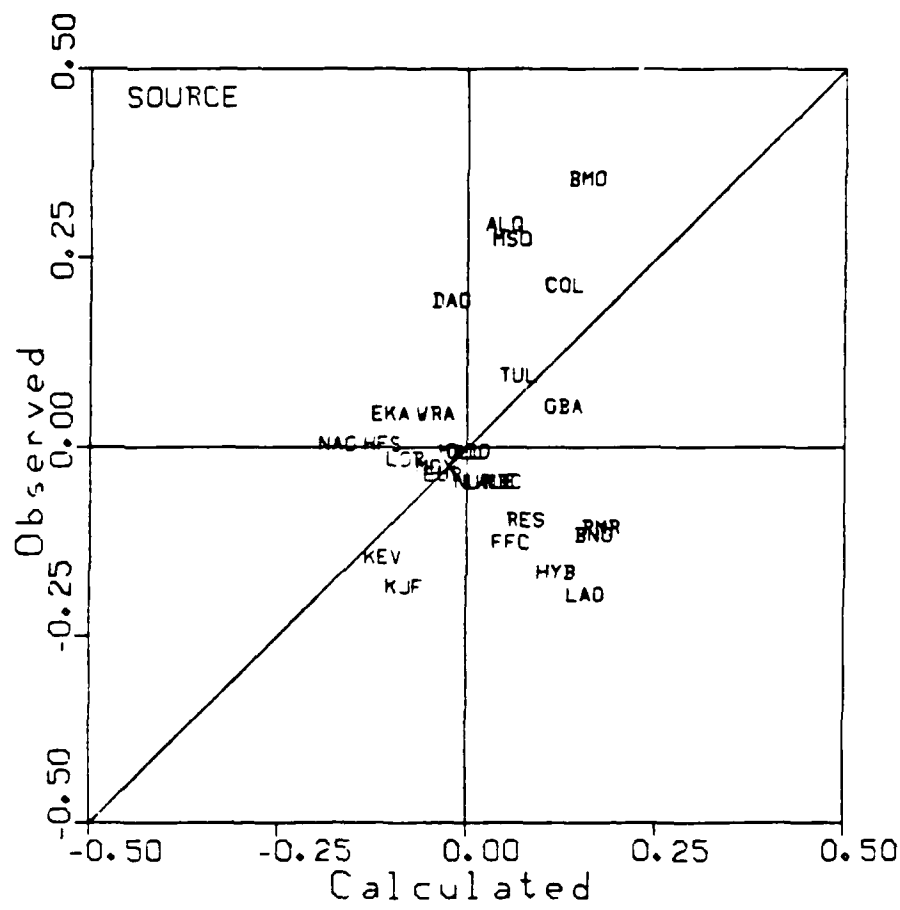


Figure 5. The figure compares calculated and observed source corrections as defined in the text.

We assume that $s_j(B)$ is an observation of a normally distributed variable with mean value, $C_j + S_j$, and standard deviation σ_j , with C_j and S_j being a radiation and a station effects respectively. In a similar way we assume $s_j(G)$ to be normally distributed with mean S_j , and standard deviation $\sigma = 0.08/\sqrt{2}$. We test the hypothesis that: $C_j = c_j$, and assuming independence among station data one can use a chi-squared test with the sum:

$$\sum \frac{(s_j(B) - s_j(G) - c_j)^2}{\sigma^2 + \sigma_j^2}$$

This hypothesis cannot be rejected at the 5% level if the stations LAO, HYB, BNG, and PMR are omitted from the sum. In other words, one cannot reject the hypothesis that the source corrections calculated from typical source mechanisms of the area are different from those obtained from the observed amplitude/period data. It should be noted, however, that there is no obvious seismological basis for omitting the data for the four stations, LAO, HYB, BNG, and PMR.

3.1.8. Concluding Remark

Even if the data studied here do not unambiguously support the hypothesis of significant and consistent source radiation pattern effects on short period P-wave amplitudes, some of the observations show some correlation that may warrant further study on this issue.

Hans Israelsson

REFERENCES

- Ringdal, A. F., 1984. "Study of magnitudes, seismicity and earthquake detectability using a global network," *NTNF/NORSAR*, N-2007 Kjeller, Norway.
- North, R. G., 1977. "Station Magnitude Bias--Its Determination, Causes, and Effect," *Technical Note* 1977-24.
- Misharina, L. A. and Solonenko, N. V., 1979. "Seismic Regionalization of Eastern Siberia and its Geological and Geophysical Formations," *Izdatelstvo Nauka* (Translation from Russian).
- Olsen, K. H., 1983. "The role of seismic refraction data for studies of the origin and evolution of continental rifts," *Tectonophysics*, 94 pp. 349-370.

3.2. A NOTE ON EARTHQUAKE DETECTABILITY: A COMPARISON BETWEEN A LOCAL AND A GLOBAL NETWORK

3.2.1. Introduction

Detection capabilities of seismological station networks are mostly estimated from station noise levels or from magnitude recurrence curves. Estimates obtained from station noise are called "simulated" estimates in this paper, as opposed to "empirical" estimates which are based on observed detection statistics. Simulated estimates are often found to be more optimistic than empirical ones.

The purpose of this note is to compare simulated and empirical estimates of a global station network by using observations of a much more sensitive local network as a reference. The comparison, which is limited to the Lake Baykal region in the USSR, also serves to illustrate detection capabilities of "external" and "internal" stations for this particular region.

This note also discusses the shape of the magnitude recurrence curve in the low magnitude range for this region using the observations of the local network. The number of earthquakes in the low magnitude range is an important consideration in the context of test ban monitoring and such estimates are usually obtained from downward extrapolation of magnitude recurrence curves which are assumed to be exponential.

3.2.2. The Lake Baykal Region and Station Networks

This study is limited to earthquakes in the geographical region of Lake Baykal (region no. 327), (Flinn, 1965) which is part of the larger seismic region of Alma Ata to Lake Baykal (region no. 28). This small region was selected in order to maintain "stationarity" of earthquake source parameters. The geographical region, which is shown in the map of *Figure 1*, encompasses most of the Baykal Rift system, which is characterized by moderate seismic activity, and covers a well defined geophysical area. Presumed underground nuclear explosions in or near this region have also been reported but are not included in this study.

The *local* network of seismological stations consists of about 20 stations in or near the Lake Baykal region. The *global* network consists of 115 selected stations reporting the ISC which were studied by Ringdal (Ringdal, 1984).

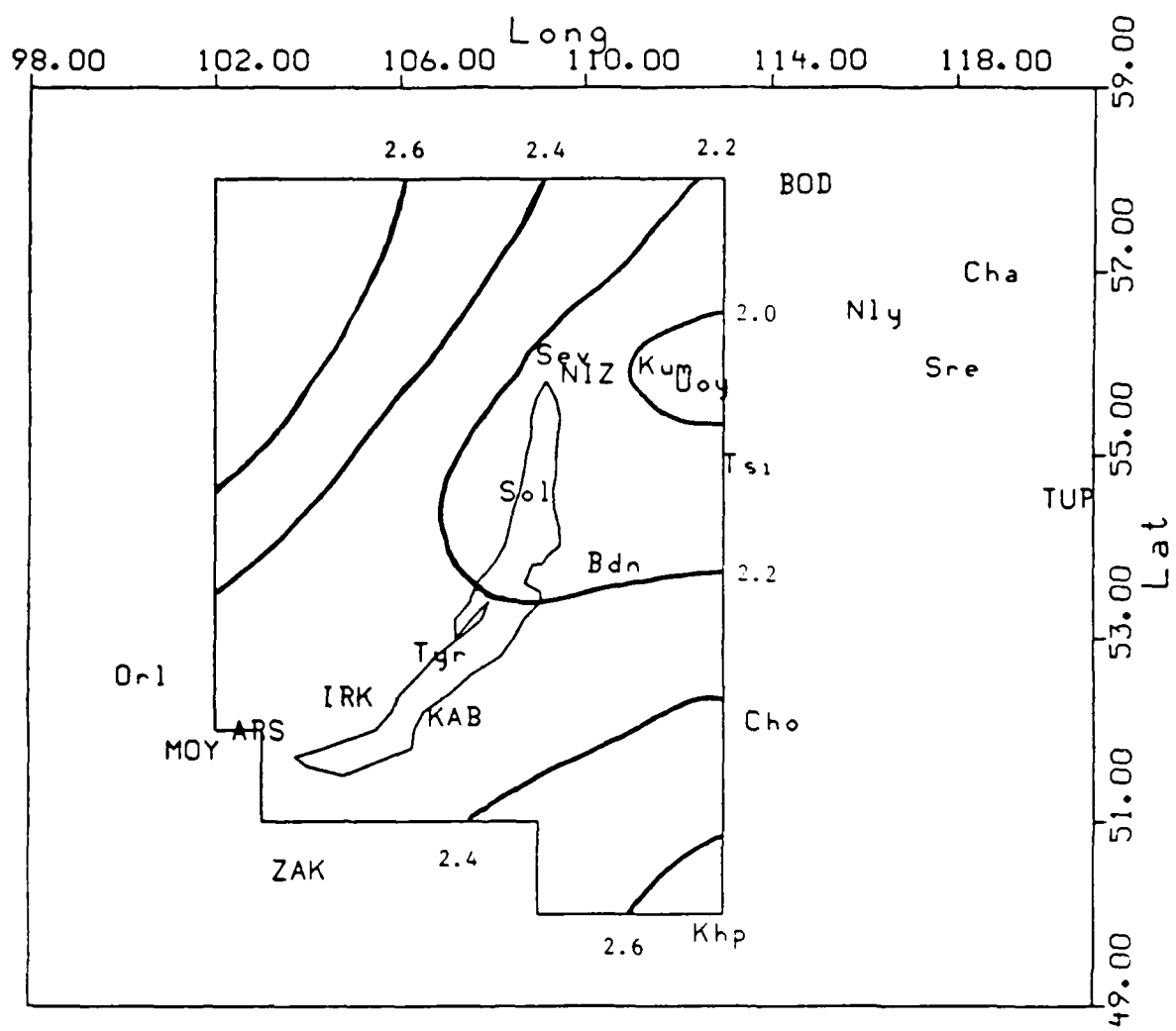


Figure 1. The map shows the extent of the Lake Baykal region, and the relative locations of the seismological stations of the local network. Contours of the 90% magnitude detection thresholds obtained from a simulation on the basis of station amplitude detection thresholds are also drawn in the figure.

3.2.3. Local Network

The stations of the local network are listed in Table I and their relative locations are shown on the map in *Figure 1* (Golenetskij, 1983). Table I also gives magnifications and estimated amplitude detection thresholds when available. Most of the stations employ CKM-3 short period instruments, the amplitude response curve of which is compared with that of a standard response of a WWSSN station in *Figure 2*. The CKM-3 has a higher relative response to frequencies above 1 Hz. The scatter diagram in *Figure 3* show a clear correlation between instrument magnification and station amplitude detection threshold and the linear relation drawn in the figure has been used to estimate threshold values for stations for which such values were not otherwise available. The distribution of the thresholds are shown in *Figure 4*. The median value is 11.7 nm/s and the values vary between 9.1 nm/s to 56.2 nm/s.

Estimates of the detection capability of this network shown in *Figure 1* have been based on the station thresholds arrived at either directly or indirectly from the station magnifications as described above. The contours represent 90% magnitude thresholds using the amplitude distance correction shown in *Figure 5*, which has been derived for the Lake Baykal Region and is based on local observations (Solonenko, 1979). This curve agrees in the distance interval 2 to 9 degrees with an average curve obtained from stations throughout the USSR (Marshall, 1986). The event magnitude is computed from this curve, $\sigma(\Delta)$, as : $M = \log(A) + \sigma(\Delta)$, i.e., with the maximum ground displacement, A , (in μ) without the associated wave period. In the computations it has been assumed that at least four stations detect a P-wave.

The network is rather unevenly distributed across the region and the detection threshold varies accordingly between $M=2.0-2.7$.

3.2.4. Global Network

The global network consists of 115 stations selected by Ringdal (Ringdal, 1984). The distribution of the amplitude detection thresholds for these stations, based on data reports to the ISC, is shown in *Figure 4*. Even if the median threshold (12.3nm/s) is similar to that for the local station network there are about 40 stations which have lower amplitude thresholds than any station in the local network. It is assumed that the majority of the stations of this global network have amplitude response curves of the WWSSN type. The relative locations of the stations and the Lake Baykal region are shown in the azimuth-distance projection in *Figure 6*. Four of the stations: BOD, IRK, MOY, and ZAK are also part of the local network.

The detection capability of this network has also been estimated on the basis of the station noise values, giving a 90% threshold around $m_b=4.1$. In the calculations it has been assumed that at least five stations detect a P-signal. Five stations were required in order to be consistent with the number of stations used by the ISC for locating events.

TABLE I. LOCAL STATION NETWORK

Station Name	Code	Location Lat(N)	Long(E)	Magnific. (1000)	Threshold (nm/s)
ARSHAN	ARS	51.90	102.40	31.00	
BODYBO	BOD	57.85	114.18	52.00	1.03
BODON	bdn	53.72	110.10	31.00	
CHARA	cha	56.90	118.20	22.00	
CHITA	cho	52.00	113.50	31.00	
IRKUTSK	IRK	52.27	104.31	17.00	1.20
KABANSK	KAB	52.05	106.65	1.10	
KHAPCHERANGA	khp	49.70	112.40	45.00	
KUMORA	kum	55.88	111.22	42.00	
MONDY	MOY	51.68	100.98	31.00	1.10
NELYATY	nly	56.48	115.68	26.00	
NIZHNE-ANGARSK	NIZ	55.78	109.55	26.00	
ORLIK	orl	52.50	99.92	31.00	
SEVEROBAYKALSK	sev	56.00	109.00	22.00	
SOLONTSOVAY	sol	54.50	108.50	12.00	
SREDNIY_KALAR	sre	55.87	117.37	45.00	
TSIPIKAN	tsi	54.80	113.00	39.00	
TUPIK	TUP	54.43	119.90	49.00	
TYRGAN	tyr	52.75	106.33	32.00	
UOYAN	uoy	55.70	112.00	4.00	
ZAKAMENSK	ZAK	50.38	103.28	51.00	0.97

Station codes in lower case have been adopted for this study to show relative location of the stations in the local network.

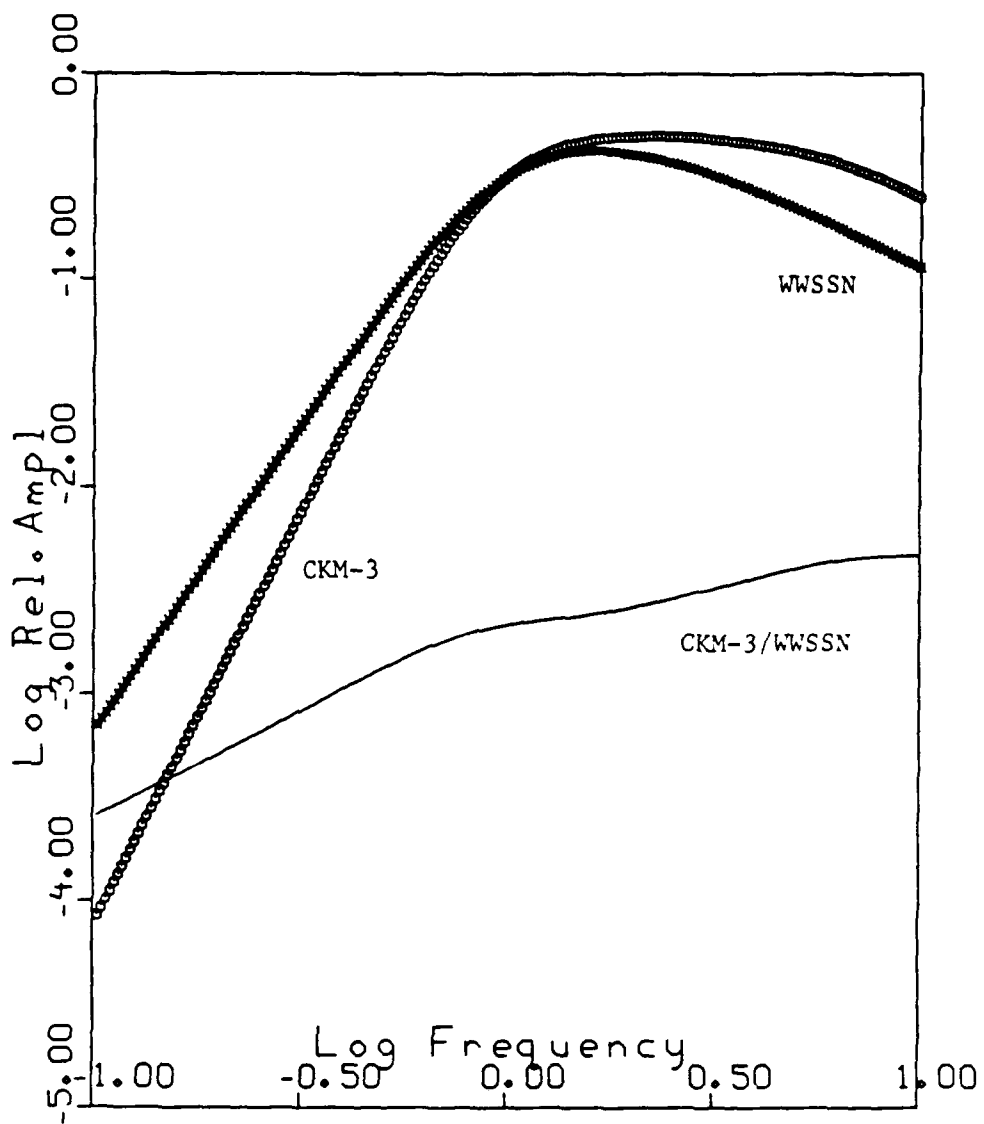


Figure 2. Comparison of amplitude response curves for a WWSSN and CKM instruments.

AD-A171 744

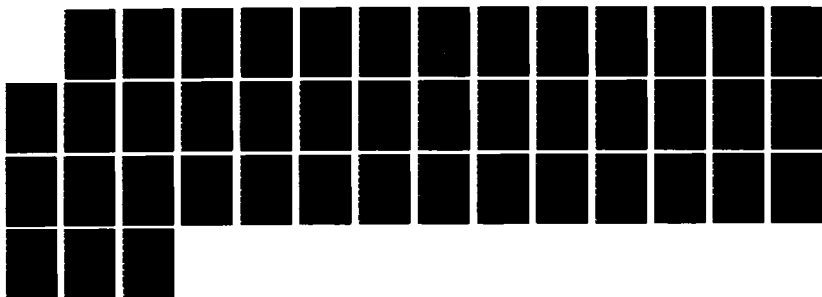
EVALUATION OF THE PERFORMANCE DURING THE GSE TECHNICAL
TEST(U) SCIENCE APPLICATIONS INTERNATIONAL CORP
ARLINGTON VA A CAMPANELLA ET AL JUL 86 SAIC-86/1114
MDA983-84-C-0028

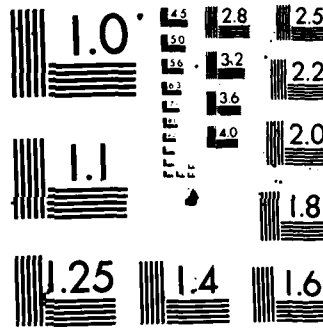
2/2

UNCLASSIFIED

F/G 17/18

NL





MICROCOPY RESOLUTION TEST CHART
NATIONAL BUREAU OF STANDARDS-1963-A

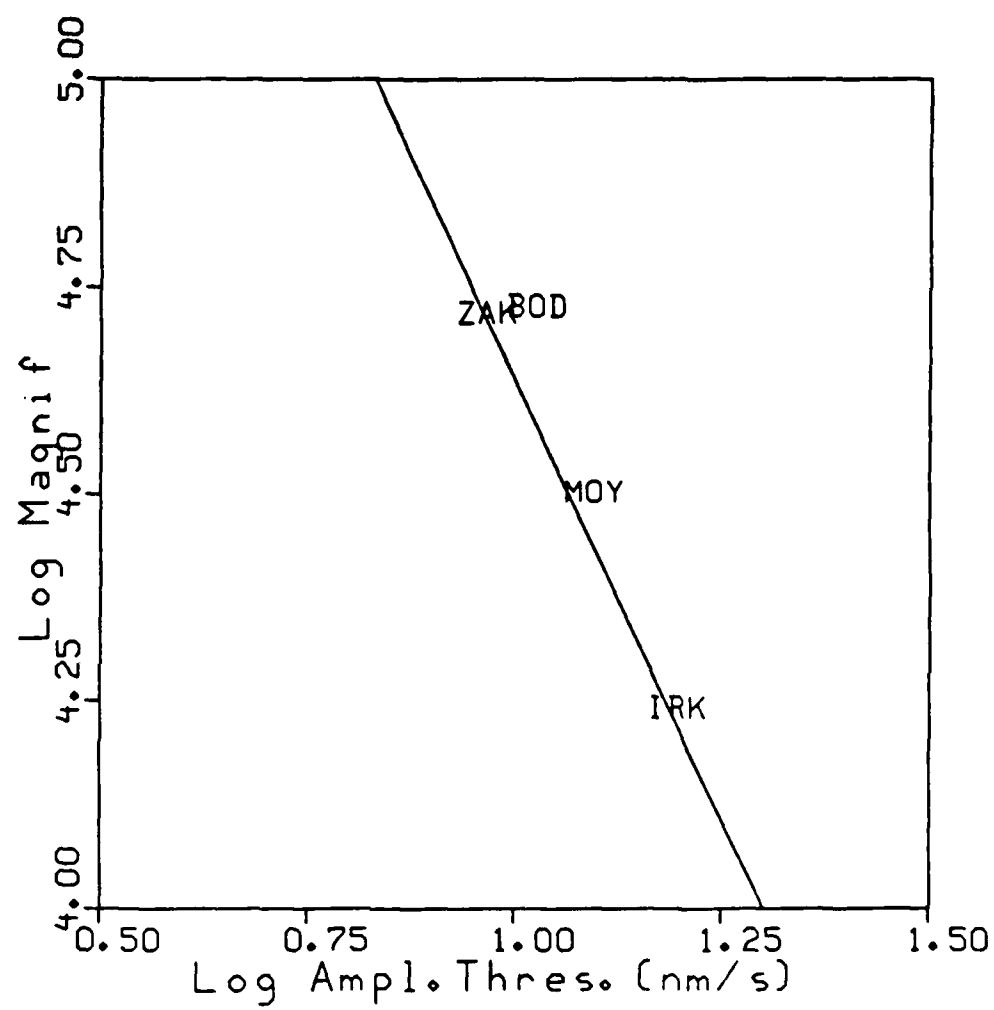


Figure 3. Instrument magnifications plotted against estimated amplitude detection thresholds for four stations (BOD, IRK, MOY, and ZAK) belonging to both the local and the global networks.

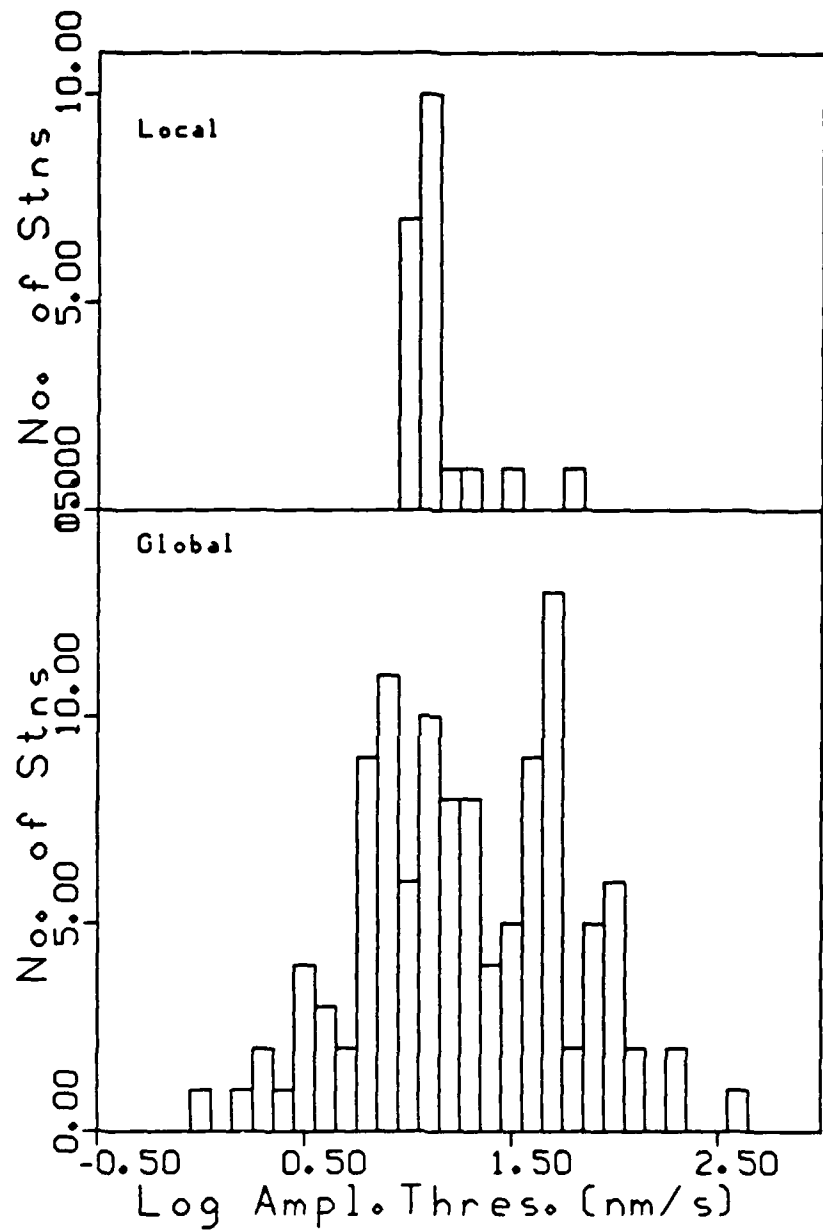


Figure 4. Distribution of amplitude detection thresholds for the local and the global networks.

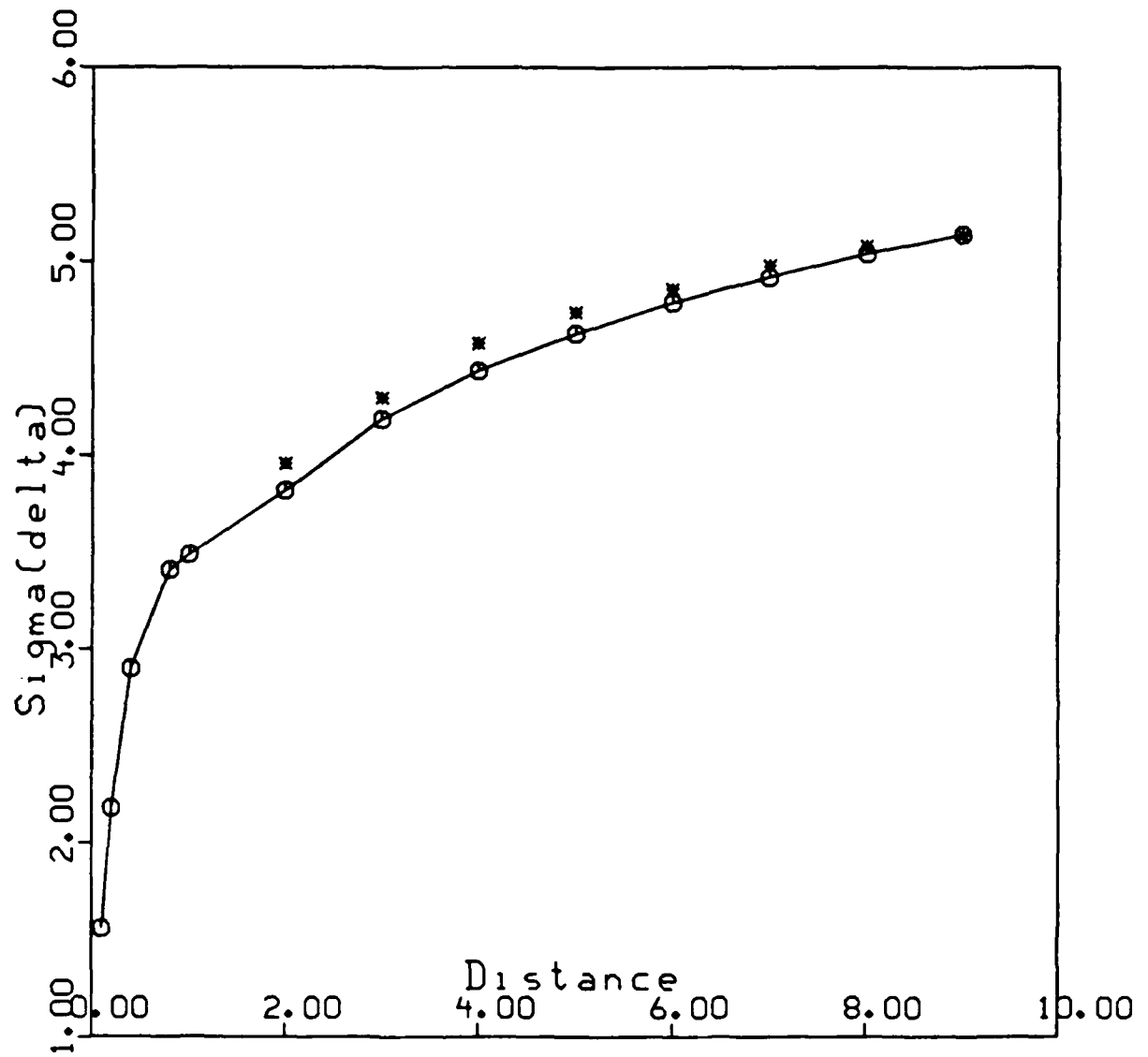


Figure 5. Amplitude distance curve for the Lake Baykal region (open circles). The curve is compared with a function (stars in the figure) estimated for the entire USSR.

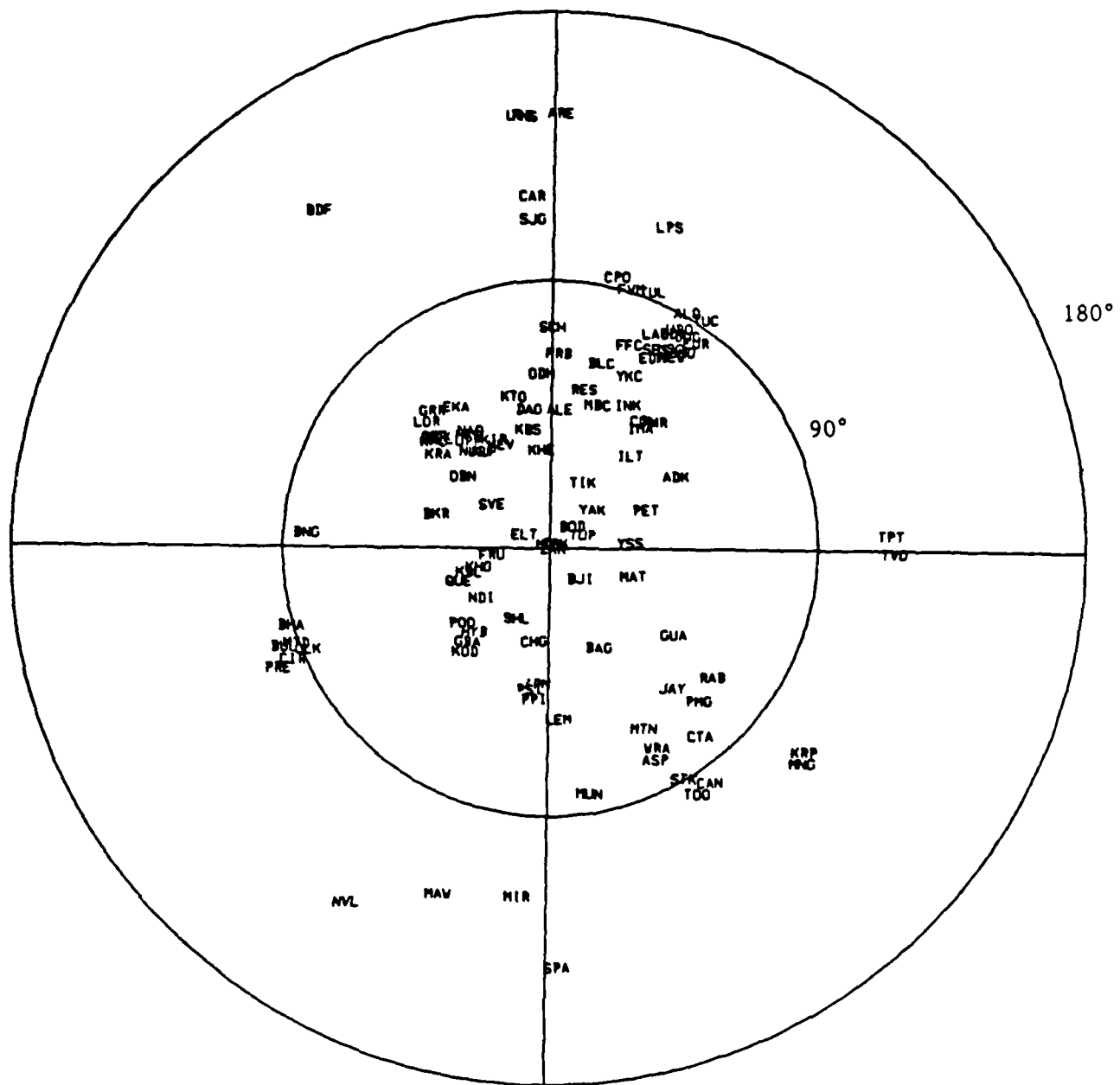


Figure 6. Locations of the seismological stations of the global network in relation to the Lake Baykal Region, which has been used as projection point.

3.2.5. Detected Earthquakes

Earthquakes detected by the two networks in the ten year period 1971 to 1980 have been used in this note. The data have been obtained from the ISC catalog and the annual catalogs of earthquakes in the USSR published by the USSR Academy of Sciences (Golenetskij, 1983).

The ISC events for the global network have been limited to events with at least one teleseismic detection. The average annual numbers are 130 and 4.5 for the local and the global network, respectively. If one assumes that the magnitude distributions are exponential with a "b"-value = 1, the ratio of number of detected events suggests a difference in detection threshold between the two networks of about 1.5 magnitude units. The geographical distributions of events are shown in *Figure 7*. The overall pattern for the two networks are similar with the activity essentially confined to the Baykal Rift zone. The map, based on the local network with its higher resolution, also shows concentrations along linear zones and scattered low-level seismicity in areas where no seismicity at all is indicated by the map based on global network data.

3.2.6. Distribution of K

The earthquakes defined and located by the local network are all classified by *K*-value, a concept introduced by Rautian in the early 60's. The *K*-value is supposed to represent the logarithm (base ten) of the part of the total energy at the earthquake focus that is converted into elastic wave energy (in Joule).

The cumulative number of earthquakes as a function of *K*-value is drawn in *Figure 8*. The network is supposed to report all earthquakes above *K*=9.0, which should be compared with $M=2.8$ (from the formula $K=4+1.8 \cdot M$) (Solonenko, 1979) and the computed thresholds below which all are less than $M=2.7$.

The *K*-values are reported only to the nearest integer and this is not sufficient for statistical testing of the distribution function. The values follow, very approximately, an exponential distribution. It appears, however, that the number of earthquakes with small *K*-values is larger than expected from a standard exponential increase. Moreover, there seems to be a local maximum of the distribution for *K*-values around 12.

3.2.7. Relation between K and m_b

Maximum likelihood estimates of the body wave magnitudes, m_b , have been obtained for all the events defined and located by the global network (Ringdal, 1984). All events detected by the global network were also detected by the local network.

The m_b -values are plotted against the *K*-values for 46 common events in *Figure 9*. Since the *K*-values are rounded to the nearest unit and given as integers, and the

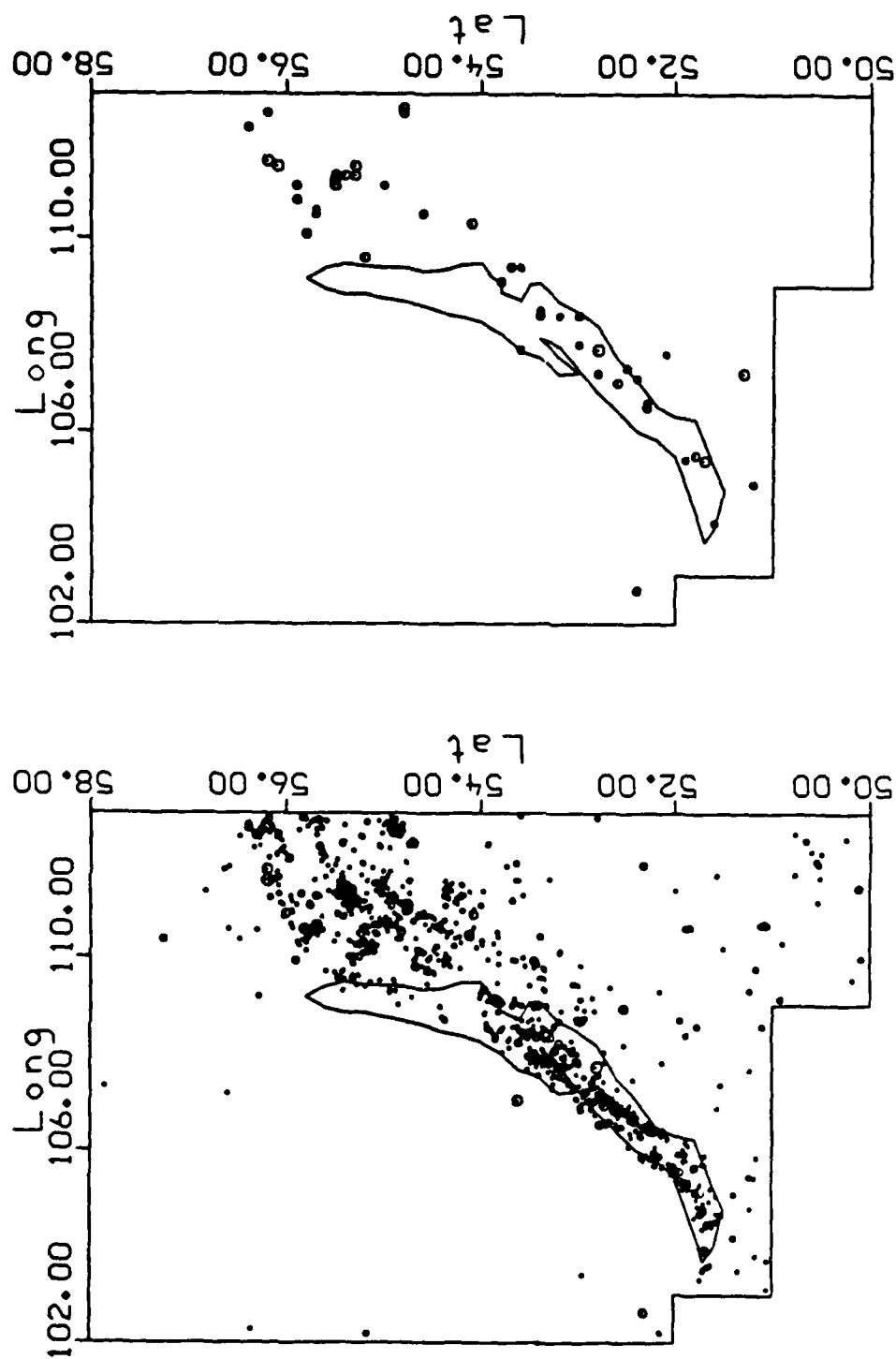


Figure 7. Geographical distribution of seismic events detected and located by the local (left) and the global (right) networks for the period 1971 to 1980. The size of the symbols are proportional to the event magnitudes and K-value determinations by the local network have been converted to equivalent magnitudes by the relation derived in the text.

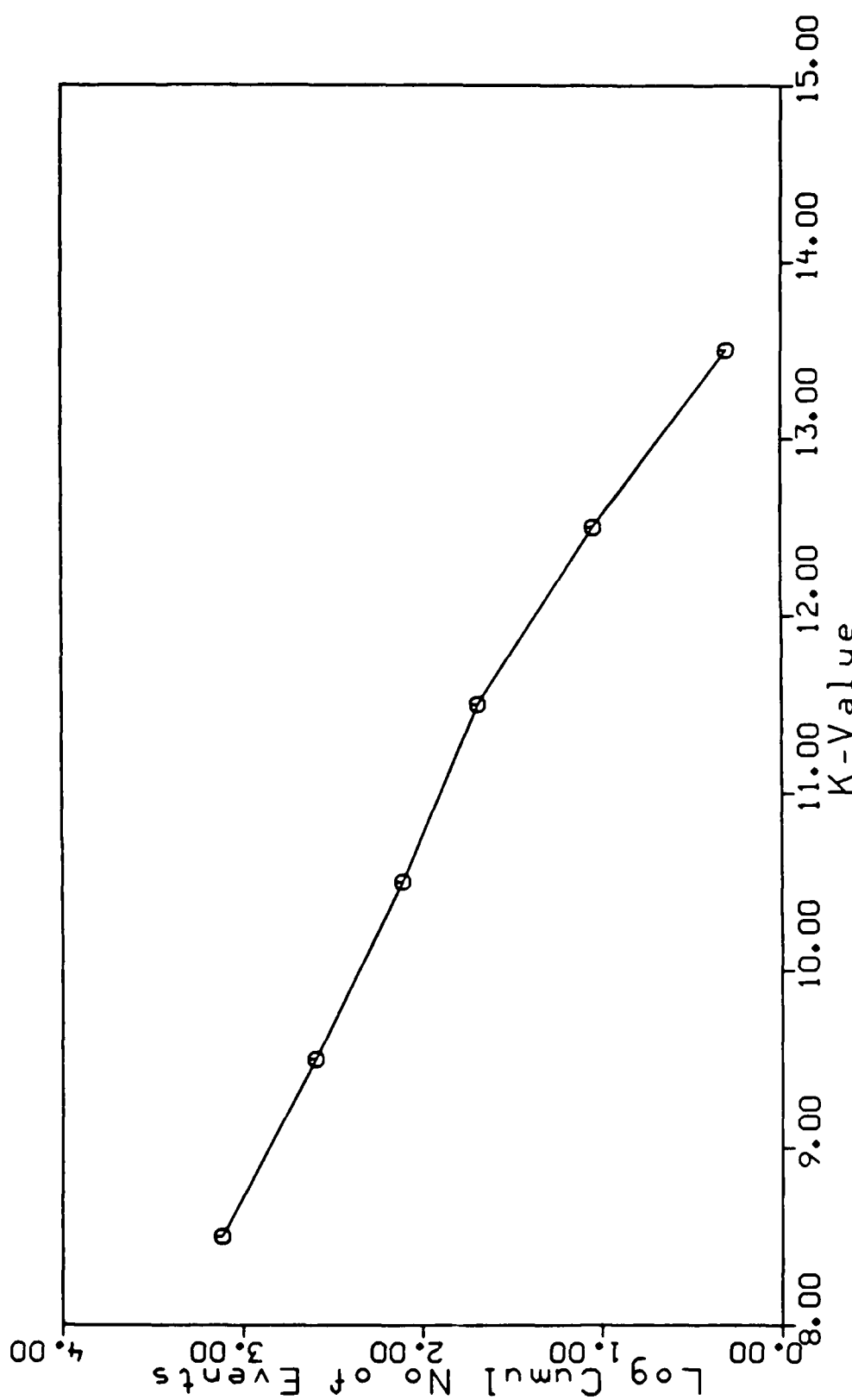


Figure 8. Cumulative number of events detected and located by the local network as a function of K-value.

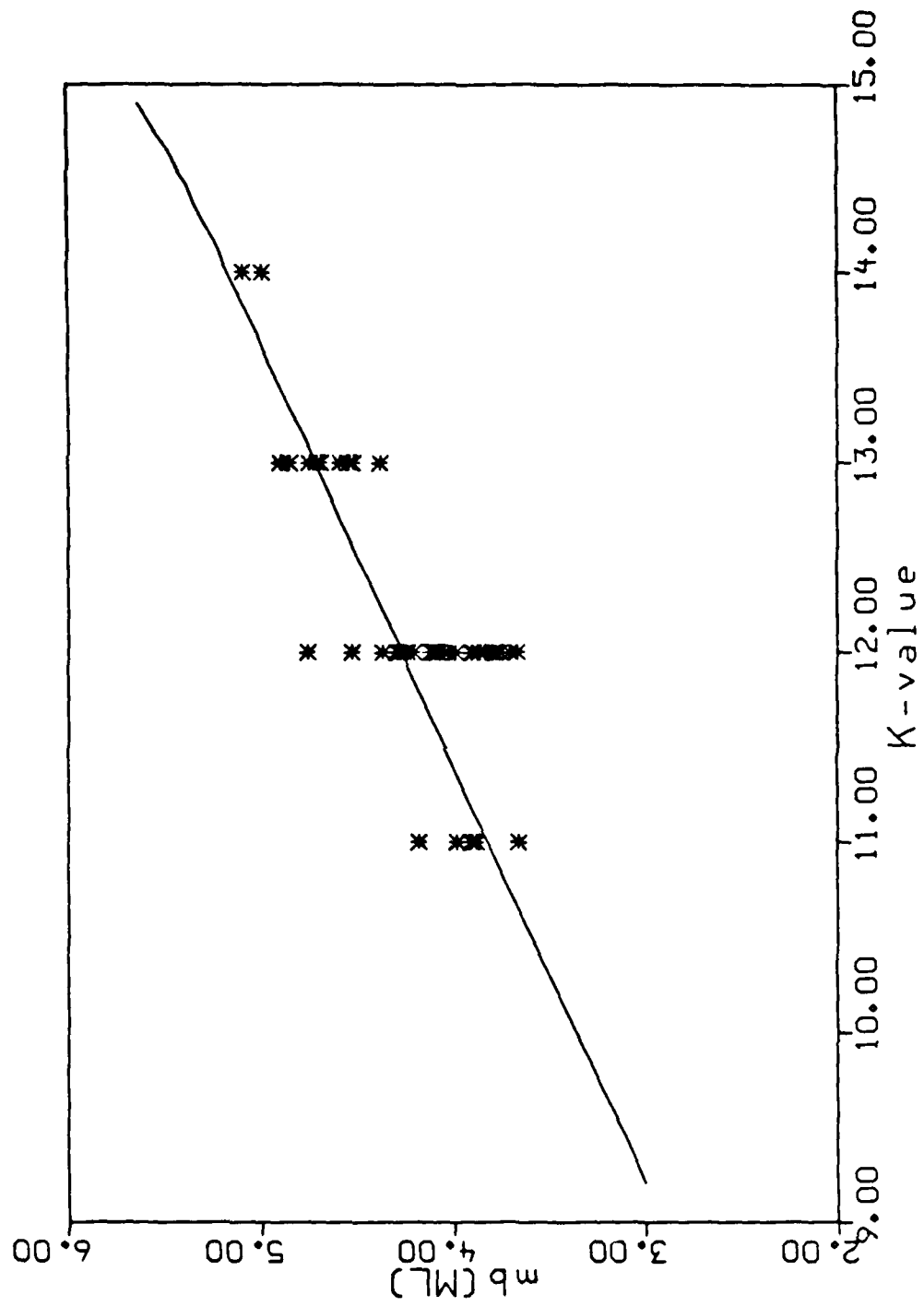


Figure 9. Scatter diagram showing m_b (maximum likelihood) plotted against K -values. The curve has been obtained as a relation between the two parameters from the model described in the text.

magnitude estimates are given to the hundredths of a magnitude unit, some considerations have to be made in deriving a relation between these two parameters.

First of all it appears that the m_b determinations are complete only for events with $K \geq 13$. Some of the $K=12$ events are close to 11.5 which in turn can be clearly below the detection threshold around $m_b = 4.0$ (Cf. Figure 9). A relation between the two parameters has, therefore, to be based on data with $K \geq 13$, which, however, leaves only two K -values for estimation. We have, therefore, derived a relation from a simple model between m_b and K described below, which has been adjusted to fit the m_b determinations for events with $K=13$.

The following model and procedure were used. The recorded amplitudes, R , as a function of frequency, f , at stations in the global (G) and in the local (L) network are assumed to be of the form:

$$R_G(f) = S(f) \cdot e^{-\pi f t} \cdot I_G(f)$$

and

$$R_L(f) = S(f) \cdot I_L(f)$$

Here, the source spectrum is assumed to be described by a corner frequency, f_c , and a constant c_f :

$$S(f) = \frac{c_f f_c^{-3}}{|(1+j(f/f_c)^3)|}$$

and the value of $t = 0.12$. The instrument response curves, I_G and I_L are supposed to be those of a WWSSN and CKM-3, respectively (Cf. Figure 1). A relation between m_b and K can be obtained from this model in the following manner. For a given value of f_c , the frequencies, f_G and f_L that maximize the recorded amplitude spectra are determined. One can then compute:

$$m_b = \log_{10}(f_G \cdot S(f_G) \cdot e^{-\pi f_G t}) + c_m$$

and

$$K = 2 \cdot \log_{10}(f_L \cdot S(f_L)) - \log_{10}(f_c) + c_K$$

The f_e term is introduced for the K -value as a measure of the source duration. The constant c_m is chosen so that $m_b=5.25$ for a seismic moment $M_0=10^{24}$ (dyne-cm). The constant c_K can then be determined to fit the observations of m_b for $K=13.0$. Attention is paid to the fact that the m_b -values really represent K -values between 12.5 and 13.5, which are assumed to have an exponential distribution over this limited interval (K_{\max}, K_{\min}). A Taylor expansion over the interval around ($K_0=13$) gives:

$$m_b = m_b(K_0) + (K - K_0) \cdot \frac{dm}{dK}$$

and $m_b(K_0)$ is then the parameter that can be estimated by the formula:

$$m_b(K_0) = E(m_b(K)) - (E(K) - K_0) \cdot \frac{dm}{dK}$$

where $E()$ denotes expected values and:

$$E(m_b(K)) = \frac{1}{n} \sum_i x_i$$

is obtained as the average value of the observed m_b determinations, x_i , by the global network. Furthermore:

$$E(K) = \frac{1}{\beta} + \frac{K_{\min} e^{-\beta K_{\min}} - K_{\max} e^{-\beta K_{\max}}}{e^{-\beta K_{\min}} - e^{-\beta K_{\max}}}$$

Approximate values of β ($\ln(10)b, b=0.75$) and the derivative $\frac{dm}{dK} \approx 0.5$ were used.

The resulting relation between m_b and K is shown in Figure 9. Up to about $K=14$ this is very close to a straight line, and above this K -value the curve turns upwards. The following linear approximation to the curve in Figure 9 can be obtained for K -values less than 14:

$$m_b = 0.45 \cdot K - 1.14$$

which can be compared with the relation between the local magnitude M and K (Solonenko, 1979):

$$M=0.56 \cdot K - 2.22$$

and this in turn gives an approximate linear relation between the two magnitudes:

$$m_b = 0.81 \cdot M + 0.66$$

An M -value of 2.8, which represents an approximate upper limit of the detection threshold for the local network in this area (Cf. *Figure 10*), would correspond to $m_b = 2.9$ according to this linear relation.

3.2.8. Distribution of m_b

The distribution of m_b determinations by the global network is shown in *Figure 10* as the cumulative number of events against magnitude. Even if the data represent a rather long period of time (ten years) the number of observations is still quite small.

The curve clearly deviates from an exponential distribution. The "b"-value is quite large between $m_b = 4.5 - 5.0$ and the curve bends over about $m_b = 4.5$ and tapers off around $m_b = 4.0$. It is difficult to clearly identify the tapering off of the curve due to decreasing detection capability, and the standard procedure of estimating the detection threshold from a recurrence relation can not readily be applied.

An empirical m_b distribution for the events in the region can also be obtained from the distribution of K -values reported by the local network by converting the K -values into m_b using the model introduced above. The resulting cumulative curve is shown in *Figure 10* for comparison. The two curves agree reasonably well in the common interval and both have a high "b"-value between $m_b = 4.5 - 5.0$ and turn around $m_b = 4.0$. The curve based on K -values also seems to indicate a relatively large number of small events, i.e., about $m_b = 3.0$ or below.

Even if the cumulative curve in *Figure 10*, which has been obtained from K -values, is based on values over about half a magnitude unit, it seems to deviate from an exponential distribution and indicates that downward extrapolation with a b-value model for estimating the number of small magnitude earthquakes can be associated with significant uncertainties.

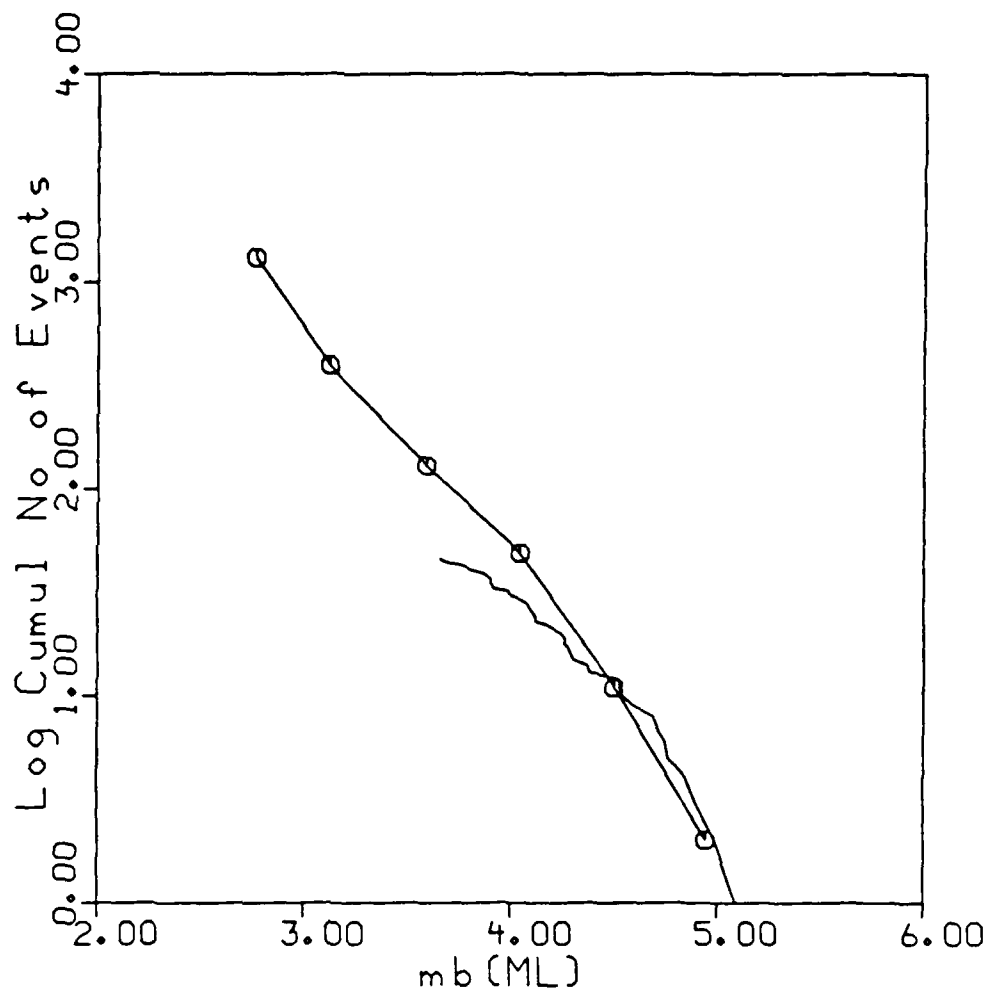


Figure 10. Cumulative number of events as a function of magnitude, m_b (maximum likelihood). The lines with and without circled symbols represent data for the global network and the local network, respectively. The local network data represent K -values reported by the network converted to m_b -values using the model described in the text.

3.2.9. K as a Measure of Energy

When the K -value was introduced by Rautian it was supposed to estimate the energy of the seismic waves emanated at the focus and be based on observations in the epicentral area, whereas magnitude determinations were relative measures based on the amplitudes on seismograms reduced to a certain standard distance. In other words, the K -value and magnitude were supposed to be direct and indirect measures of energy released at the focus.

The K -values can be compared with energy estimated from the m_b -values and the corresponding moment values using the model above.

The following two relations between energy E , surface wave magnitudes, M_s , and m_b gives a relation between m_b and energy that should give a rough estimate:

$$\log(E) = 1.5 \cdot M_s + 11.8$$

and

$$m_b = 0.63 \cdot M_s + 2.03$$

gives:

$$\log(E) = 2.38 \cdot m_b + 6.97$$

Minimum estimate of strain energy drop (Kanamori, 1977) can be obtained from the relation:

$$E = (\Delta\sigma / 2\mu) \cdot M_0$$

Assuming the stress drop $\Delta\sigma = 20 - 60$ bars and $\mu = 3 - 6 \cdot 10^{11}$ dyn/cm² one gets:

$$E = M_0 / (2 \cdot 10^4)$$

Finally, the energy derived from the K -value can be written as (in ergs):

$$\log(E) = K + 7$$

A comparison of numerical values shows that energies obtained from m_b and M_0 are of the same order, whereas that obtained from the K -value is about one order or more larger. For example, the model and formulas above give for $m_b=4.72$, values of $\log(M_0)=23.10$ and $K=13$ with the energy values: $\log(E)=18.2, 18.8$, and 20.0 , respectively.

3.2.10. Incremental Detection Probabilities

The incremental detection probability, p , as a function of magnitude, m , is usually assumed to have the shape of a Gaussian distribution function:

$$p(m) = \Phi\left(\frac{m - m_T}{\sigma_T}\right)$$

where m_T is the magnitude threshold (50%) and σ_T the associated standard deviation.

The incremental detection probability as a function of body wave magnitude computed for the global network on the basis of station amplitude thresholds is shown in Figure 11. The mean value and standard deviation are, respectively, $m_T=3.89$, and $\sigma_T=0.12$.

An "empirical" curve can be obtained as a function of the K -value from the ratio of number of events detected by the global network and the number of events detected by the local network. The K -values can be converted to m_b -values using the model described above. Since the K -values are integers, the incremental "curve" as shown in Figure 11 is a piecewise constant function.

As can be seen from the data in Figure 11, the empirical incremental probabilities are greater than zero and less than one in two intervals. The values for these intervals can, however, be used to estimate an incremental curve with the shape of a normal distribution. Such a curve takes the distribution of K -values into account.

If one assumes as before that the K -values are exponentially distributed in the two intervals (with different β -values) and uses linear relations between m_b and K over these intervals, the probability density of m_b , $g(m)$ also becomes exponential over the intervals ($m(1)_{\min}, m(2)_{\max}$):

$$g(m) = \gamma \frac{e^{-\gamma(m - m(i)_{\min})}}{1 - e^{-(m(i)_{\max} - m(i)_{\min})}}$$

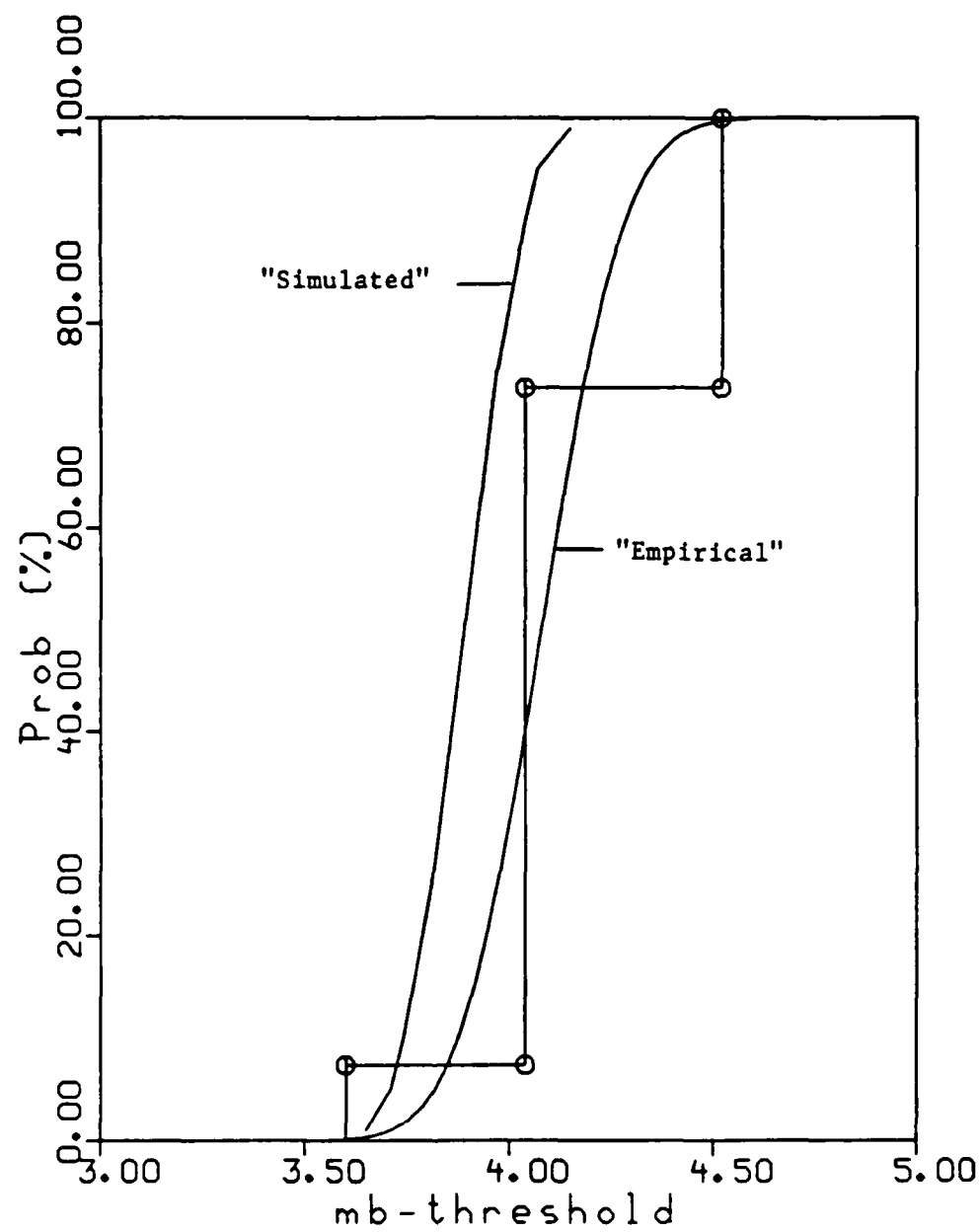


Figure 11. Incremental detection probabilities obtained from simulated and empirical estimates.

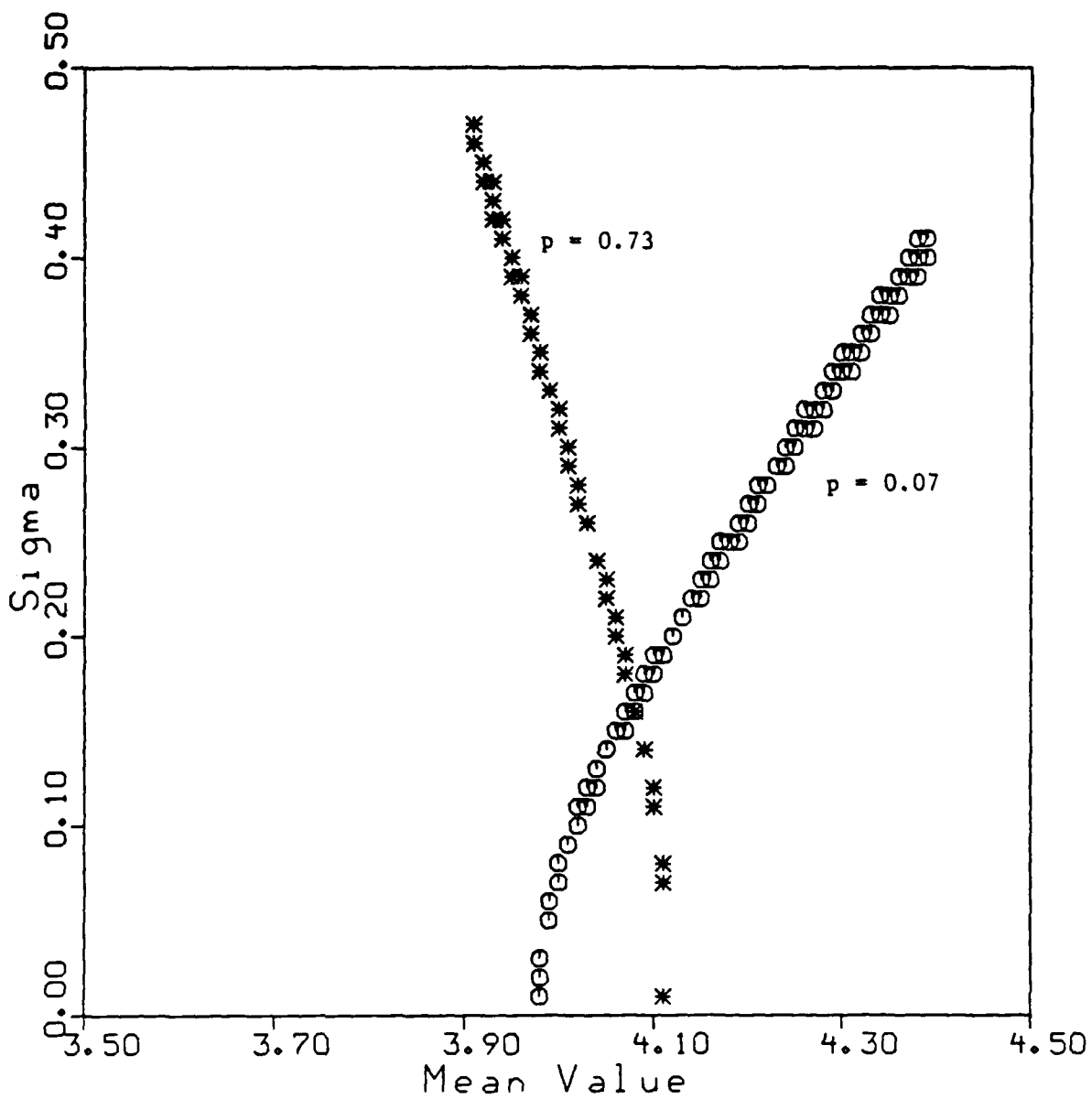


Figure 12. The figure shows the threshold values (m_T, σ_T), which satisfy observed detection probabilities as described in the text. The crossing point gives values for a solution, corresponding to the "empirical" curve in *Figure 11*.

with $\gamma = \beta / \frac{dm}{dK}$. Values of β and $\frac{dm}{dK}$ can be obtained from *Figure 9* and *Figure 10*. The two incremental probabilities, p_i , (7% for $K=11$ and 73% for $K=12$) can then be related by the two integral equations ($i=1,2$):

$$p_i = \int_{m(i)_{\min}}^{m(i)_{\max}} g_i(m) \cdot \Phi\left(\frac{m - m_T}{\sigma_T}\right) dm$$

Pairs of (m_T, σ_T) that satisfy the two integral equations are plotted in *Figure 12*. The crossover point (4.08, 0.16) gives the pair that satisfies both equations and is chosen as a solution. The corresponding "empirical" curve is drawn in *Figure 11* and is shifted about 0.2 magnitude units towards higher magnitudes relative to the "simulated" one.

3.2.11. Concluding Remarks

A simple model has been used to derive a relation between m_b and the K -value, which is in reasonable agreement with other estimates based on larger data samples. Energy values from K estimates, however, appear to be consistently larger than values derived from a model for moments used here.

The local network, consisting of stations with fairly low detection capability, has a detection threshold one magnitude unit or more lower than that for the global network which includes stations with higher detection capability.

The "empirical" detection threshold for the global network is slightly lower than the "simulated" threshold obtained by the "Networth" approach.

The data for m_b and K suggest that the number of earthquakes may not necessarily vary exponentially over the entire magnitude range and, in particular, at smaller magnitudes. This, in turn, has implications for downward extrapolation of a magnitude recurrence curve in order to estimate the number of small magnitude earthquakes.

Hans Israelsson

REFERENCES

- Flinn, Edward A. and Engdahl, Eric B., 1965. "A proposed Basis for Geographical and Seismic Regionalization," *Reviews of Geophysics*, 3 pp. 123-149.
- Ringdal, Frode, 1984. "Study of magnitudes, seismicity and earthquake detectability using a global network," *Preprint NTNF/NORSAR*, N-2007, Kjeller, Norway.
- Golenetskij, S. I., 1983. "Earthquakes in the Baykal region," *USSR Academy of Sciences*.
- Solonenko, V. P. and Kotchetkov, V. M., 1979. "Energy Classification of Earthquakes," *Seismic Regionalization of Eastern Siberia and its geological and geophysical foundations*.
- Marshall, P. D., Bingham, J., and Young, J. B., 1986. "An analysis of P-wave amplitude recorded by seismological stations in the USSR," *Geophys. J. R. Astr. Soc.*, 84 pp. 71-91.
- Kanamori, H., 1977. "The energy release in great earthquakes," *J. Geophys. Res.*, 82 pp. 2981-2987.
- Gutenberg, B. and Rochler, C. F., "Earthquake magnitude, intensity, and acceleration," *Bull. Seism. Soc. Am.*, 46:105-145.
- Weichert, D. W. and Basham, P. W., "Deterrence and False Alarm in Seismic Discrimination," *Bull. Seism. Soc. Am.*, 63:1119-1132.

4. YIELD ESTIMATION

4.1. SENSITIVITY OF m_b TO EARTH ATTENUATION

4.1.1. Introduction

A short study has been performed to examine the sensitivity of teleseismic P waveform shapes and body-wave magnitudes to changes in explosion source parameters and earth attenuation. Most recent estimates of attenuation have been based on frequency-domain analyses--often on impressive volumes of data--with assumptions made about the source parameters. Additional assumptions have also been made about the attenuation model used for these estimates, that is, whether Q is constant or frequency-dependent, and if the latter, what the dependency is. Our objective is to determine if observations of waveform characteristics in the time domain could help limit these assumptions and increase our understanding of the trade-offs between source effects and earth attenuation.

The study is divided into two parts. First, synthetic seismograms are constructed by combining the effects of a source time function, near-source reflections and interactions with the free surface, earth attenuation and short-period instrument response. The simulated waveforms and corresponding m_b values are displayed as functions of the source corner frequency and the degree of attenuation. In the second part of the study, additional anelastic attenuation is introduced to RSTN short-period teleseismic recordings of P-waves from several underground nuclear explosions. The resulting waveforms are examined in the time domain and the sensitivity of m_b to the additional earth attenuation is compared for NTS and Semipalatinsk events.

The synthetic waveforms are numerically generated using a linear convolutional model

$$w_t = s_t \otimes c_t \otimes a_t \otimes i_t \quad (1)$$

where

s_t is the source time function computed using the von Seggern-Blandford explosion source model,

c_t is the earth impulse response containing near-source reflections or other effects that modify the source function from the idealized von Seggern-Blandford model,

a_t is the minimum-phase earth attenuation operator,

i_t is the RSTN short-period instrument response, and

\otimes denotes convolution.

The source time function s_t was computed using the von Seggern-Blandford source model of underground nuclear explosions (von Seggern & Blandford, 1972). This source model yields a far-field displacement pulse with an f^{-2} decay in displacement amplitude at high frequencies. The corner frequency as well as the (low-frequency) amplitude level of displacement spectrum are determined by the explosion yield. A parameter "B" controls the overshoot of the displacement spectrum in the vicinity of the corner frequency. Since this study is primarily concerned with variations in m_b with source and attenuation parameters, the low-frequency level of the von Seggern-Blandford source was held constant. This normalization of the source moment enabled a direct evaluation of the sensitivity of m_b and waveform shape to the trade-off between earth attenuation and source corner frequency.

The near-source earth response c_t contains no geometric spreading or other rigorous wave-propagation factors. Instead, it is based on a simple model of an impulse for the direct P-wave arrival followed by various phases based on hypothesized linear or non-linear reflections between the source and the surface. This near-source term is varied from a single unit impulse to an impulse followed by one delayed pP phase to a simulated "non-linear" response consisting of a series of reflection coefficients based on results of finite-element modeling of buried explosions including non-linear effects (Perl *et al.*, 1979; Bache *et al.*, 1980).

The earth attenuation operator a_t has an amplitude spectrum of the form

$$e^{-\pi f t^*(f)}$$

where $t^*(f)$ is the path-averaged attenuation term which may depend on frequency. The minimum-phase spectrum is computed using the Kolmogorov method (Claerbout, 1976) after extending the amplitude spectrum to twice the Nyquist frequency. Two different models for the frequency dependence of t^* were tested. The first model was frequency-independent t^* (constant Q) and the second had a frequency dependence of the form

$$t^* = t^*_0 \quad f < 1 \text{ Hz}, \quad (2)$$

$$t^* = t^*_0 f^{-0.5} \quad f > 1 \text{ Hz}$$

in which Q increases with frequency. The exponent of -.5 and corner frequency of 1 Hz for the second attenuation model are not based on any one particular physical model of anelastic attenuation. These parameters are, however, within the range of published estimates. It is commonly recognized (Cormier, 1982) that attenuation must decrease with frequency across the mid-period to short-period band. This particular form of the frequency variation of attenuation was chosen to examine the effects of a reasonable frequency-dependent attenuation for comparisons with the frequency-independent case. The earth attenuation operator, with its minimum-phase spectrum, is meant to account for intrinsic anelastic attenuation but not for scattering from earth inhomogeneities. The

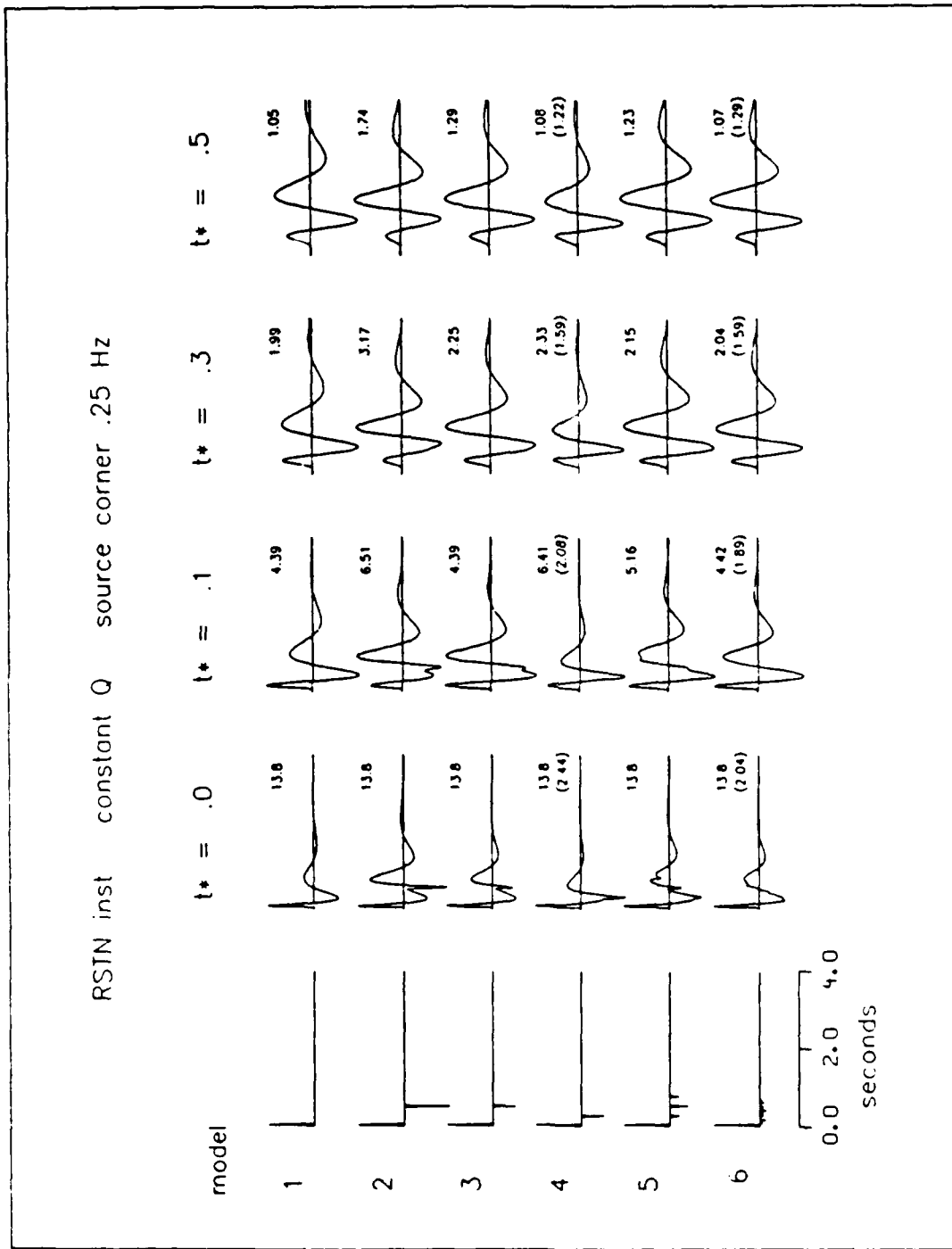


Figure 1. Synthetic waveforms constructed by combining various near-source reflection models (shown in the left column) with a source time function, constant-Q earth attenuation and RSTN short-period instrument response. The source function has a corner frequency of .25 Hz. The degree of attenuation is indicated by the term t^* . The numerical values adjacent to each waveform are the peak amplitudes. The m_b values, measured between the first trough and subsequent peak, are displayed in parentheses for models 4 and 6.

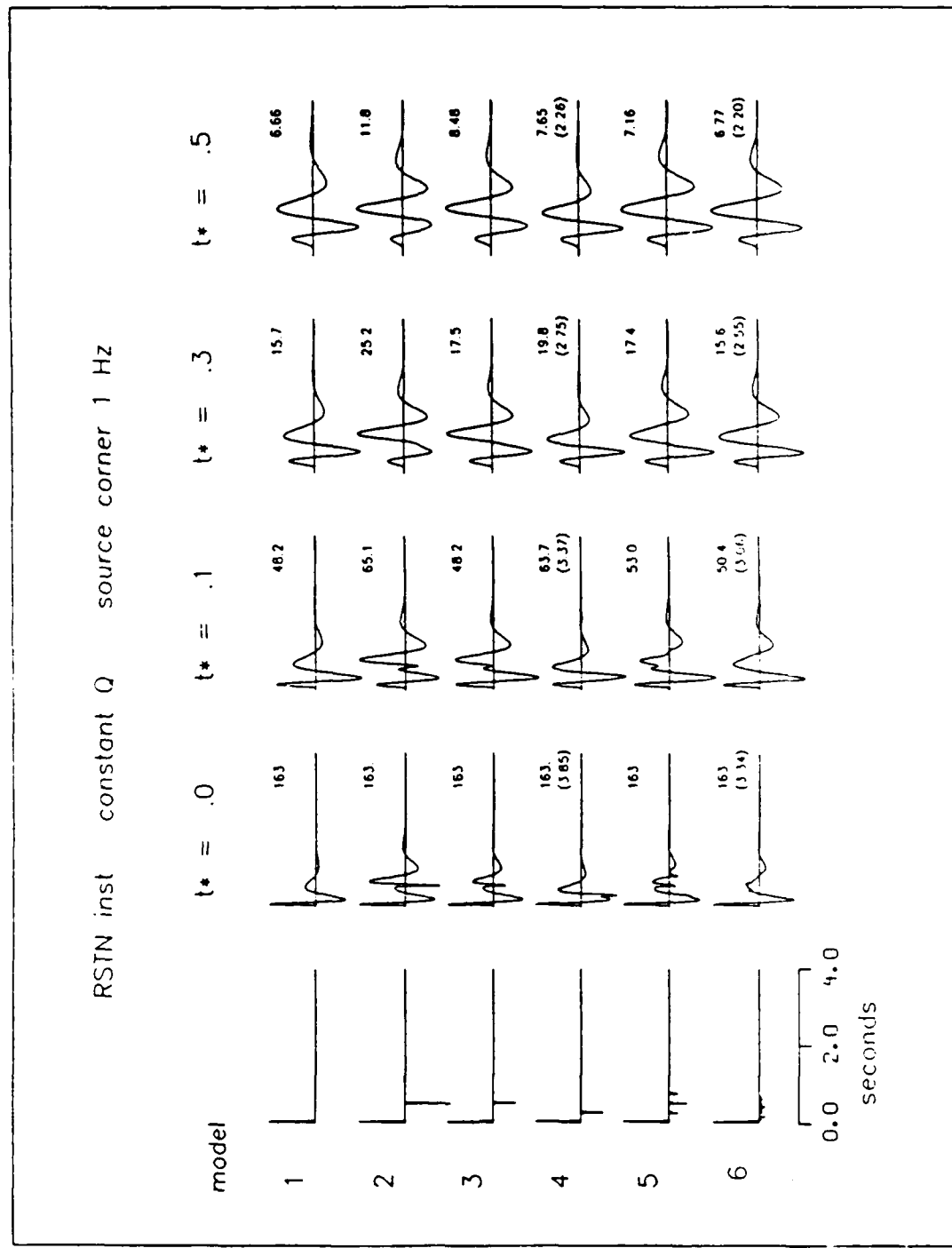


Figure 2. Synthetic waveforms similar to those in Figure 1 constructed using constant-Q attenuation and a source corner frequency of 1 Hz.

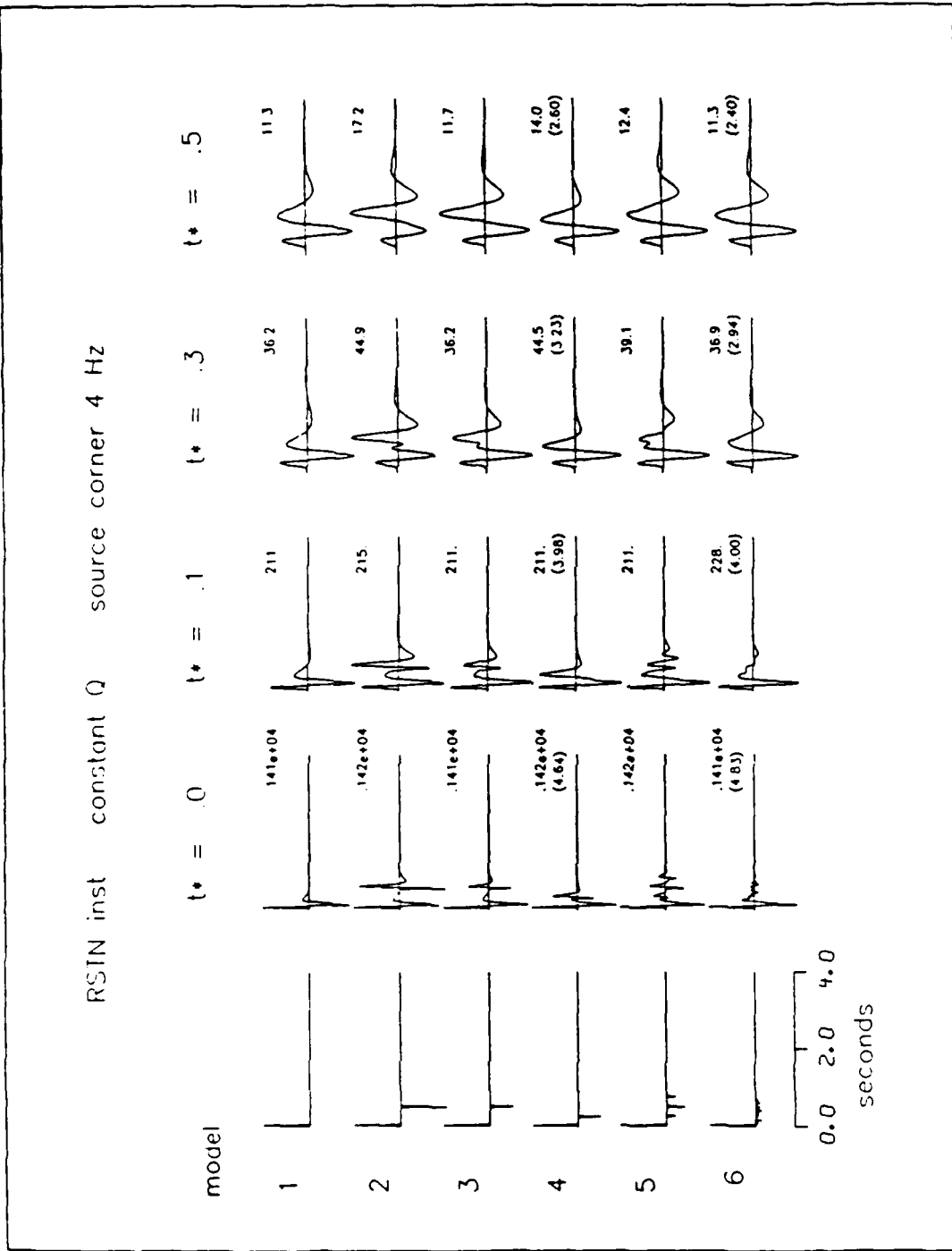


Figure 9. Synthetic waveforms constructed using constant-Q attenuation and a source corner frequency of 4 Hz.

Figures 4-6 show results analogous to *Figures 1-3*, except that a frequency-dependent t^* , as described in Equation 2, was used. As was true for the cases using a frequency-independent t^* in *Figures 1-3*, near-source effects (for a given corner frequency and t^*) cause significant variations in the waveforms, amplitudes and m_b values. The dependence of m_b on source corner frequency is even greater than was the case for a frequency-independent t^* . As shown on *Figures 4-6*, a shift in corner frequency from 0.25 to 1 Hz causes more than a full order of magnitude change in m_b for $t^* = 0.3$ seconds. A further corner-frequency shift to 4 Hz causes an additional change of 0.5-1.0 magnitude units in m_b .

Figure 7 shows a summary of the variation in m_b in response to t^* and source corner frequency. The values plotted correspond to near-source model 4, in which a primary pulse of unit amplitude is followed by a reflection of amplitude -0.5 and delay of 0.25 seconds. The m_b values have been normalized at $t^* = 0.0$ seconds to emphasize the change of magnitude with t^* . Results are shown for all three source corner frequencies analyzed: 0.25, 1.0 and 4.0 Hz. Also plotted in *Figure 7* are lines corresponding to the equations

$$\Delta m_b = -1.0 \Delta t^*$$

and

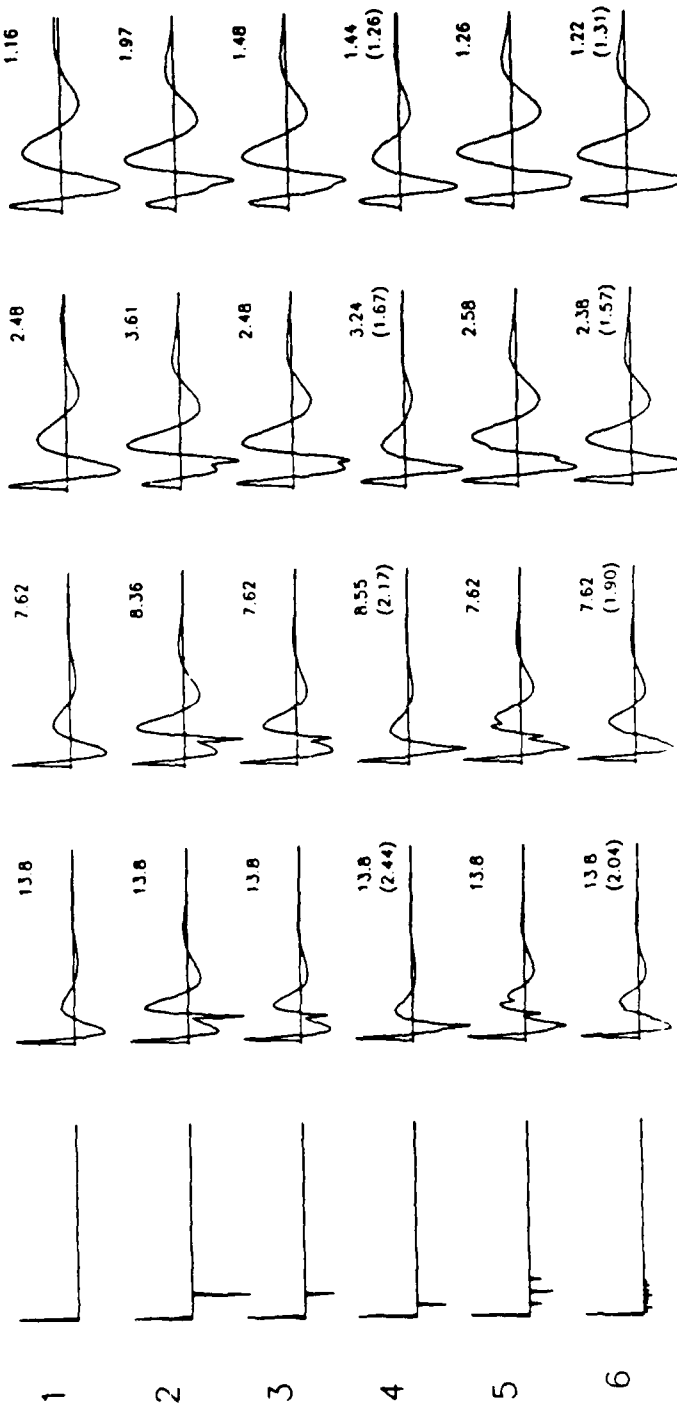
$$\Delta m_b = -2.0 \Delta t^*.$$

For comparison, Der *et al.* (1979; 1981) have empirically determined a slope of -1.35 by analyzing amplitude spectra of P-wave signals on short-period recordings. In fact, Der *et al.* found a considerable scatter in their results and the value of -1.35 is an average result. All of the present modeling results show a greater slope in the m_b vs t^* relation than do the frequency-domain empirical studies of Der *et al.*. The modeling results indicate that the slope of m_b vs t^* flattens with increasing t^* , so the sensitivity of m_b to t^* is more consistent with the empirical value of -1.35 for larger t^* . As the corner frequency of the source decreases (i.e., as yield increases) the effects of attenuation on m_b become less pronounced. This is to be expected since sources with larger yields contain proportionately less high-frequency energy. *Figure 8* shows the slopes of the curves in *Figure 7* plotted as a function of t^* and source corner frequency. At larger t^* , the slopes are approximately the same for constant and non-constant Q. Note that the slopes of the m_b vs t^* curves in *Figure 8* are indistinguishable for different combinations of source corner frequency and attenuation, illustrating the well-known trade-off between the source and attenuation effects.

Magnitude values for near-source models 4 and 6 are shown in Table I as a function of source corner frequency and t^* . Again, the sensitivity of m_b to changes in either t^* or source corner frequency are clearly shown. A somewhat more detailed look shows that, for sources having corner frequencies near 1 Hz and for t^* near 0.3, a change in corner frequency of about one-half octave produces the same Δm_b as a t^* change of about 0.1 seconds. Table I shows results for frequency-independent Q; similar results occur for frequency-dependent Q.

RSTN inst non-constant Q source corner .25 Hz

model $t^* = .0$ $t^* = .1$ $t^* = .3$ $t^* = .5$



0.0 2.0 4.0
seconds

Figure 4. Synthetic waveforms similar to those shown in Figure 1 except the earth attenuation is based on a non-constant Q model. Q is constant up to 1 Hz and varies as $f^{-1.5}$ for higher frequencies. The source corner frequency is .25 Hz as in Figure 1.

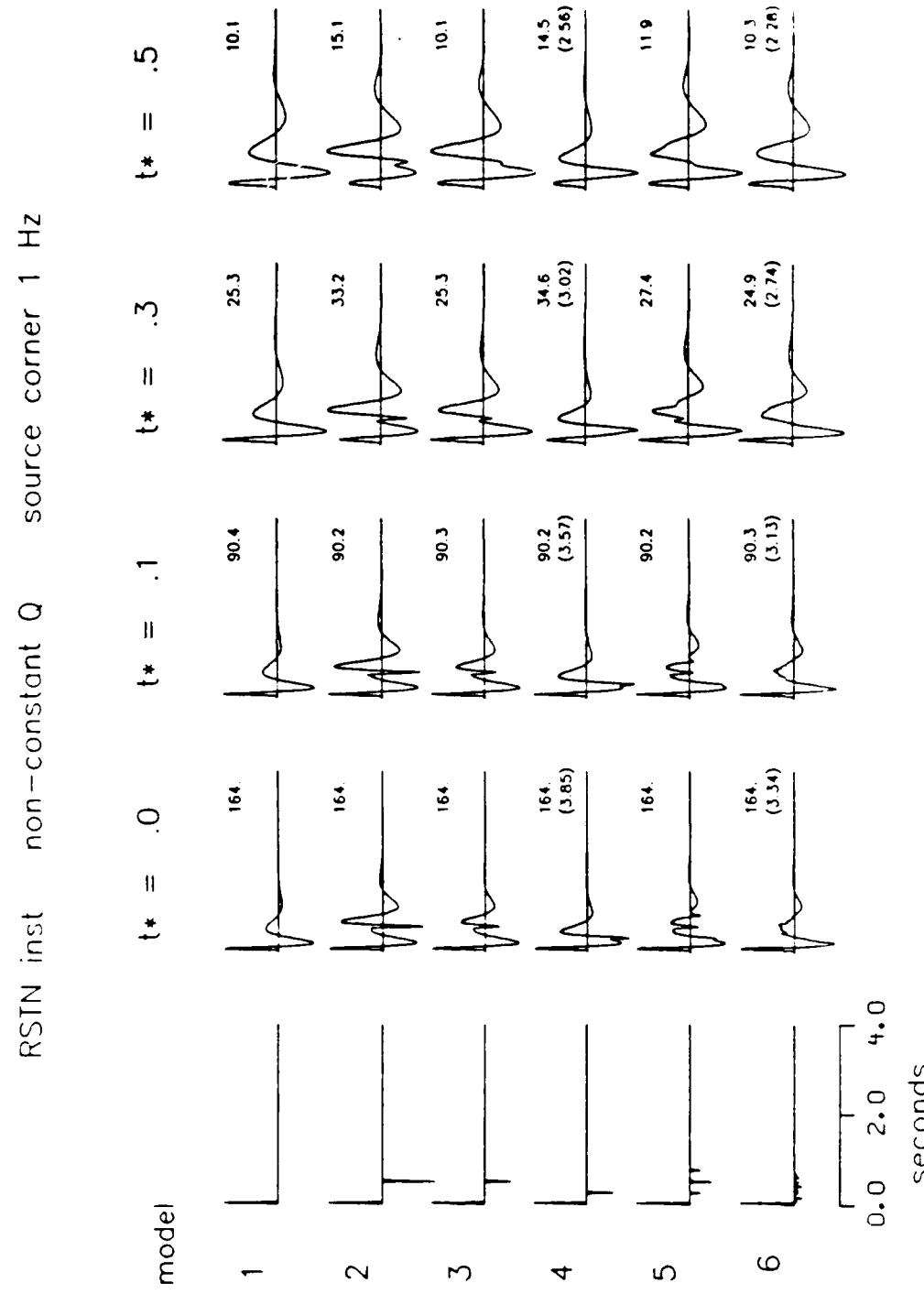


Figure 5. Synthetic waveforms similar to those in Figure 4 constructed using a non-constant Q model and a source corner frequency of 1 Hz.

RSTN inst non-constant Q source corner 4 Hz

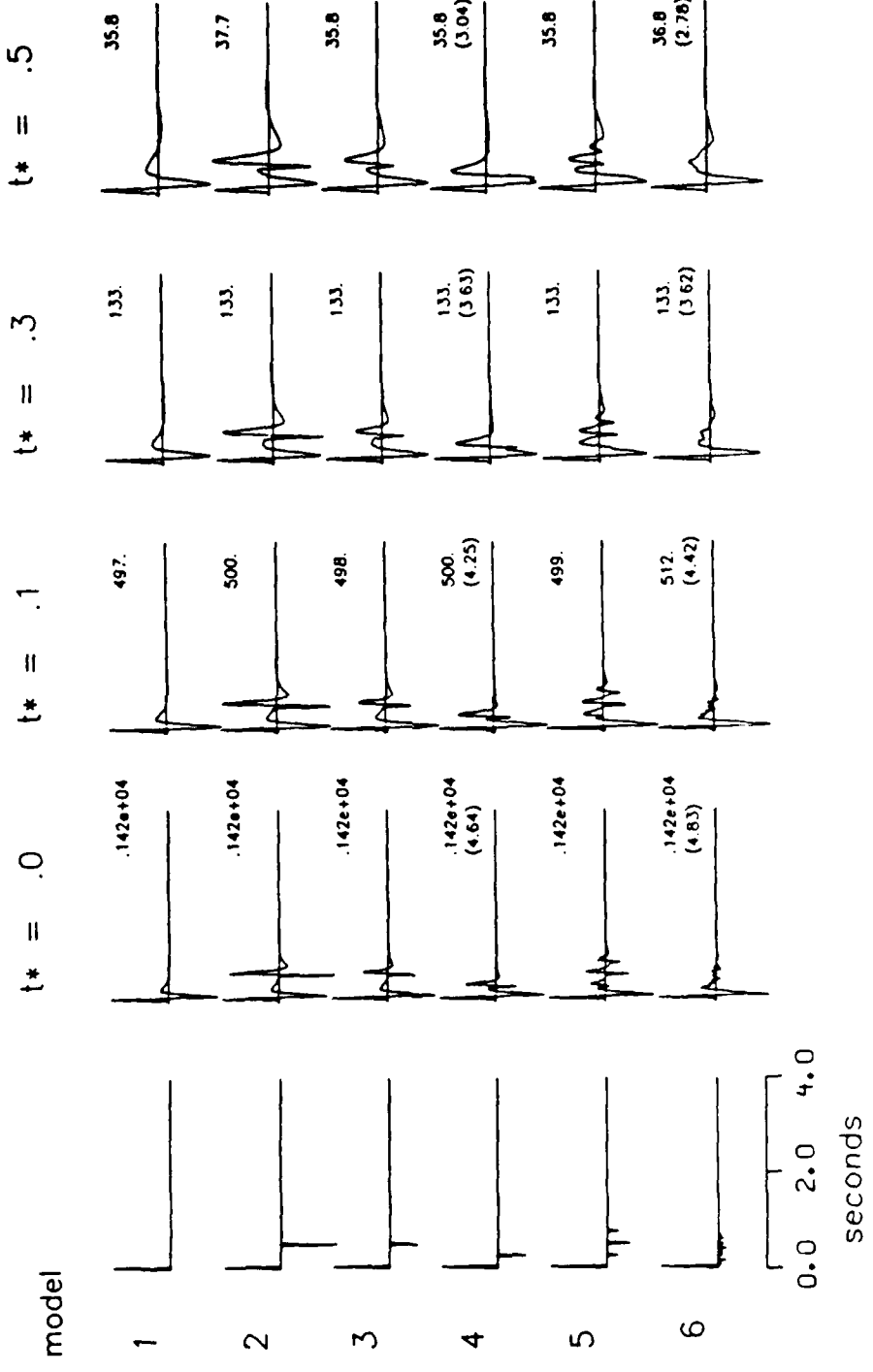


Figure 6. Synthetic waveforms constructed using a non-constant Q model and a source corner frequency of 4 Hz.

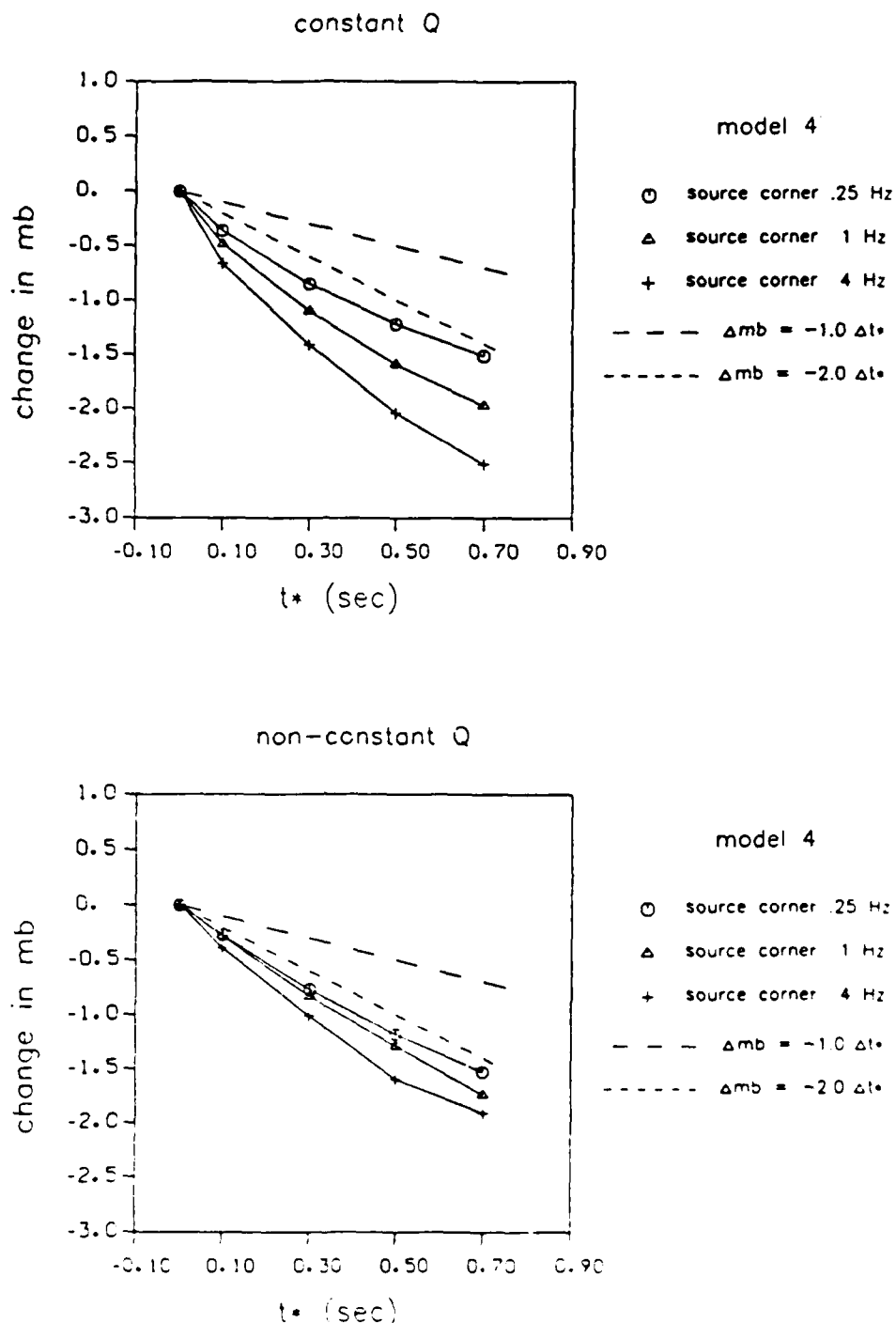


Figure 7. Plots of the variation in m_b as a function of t^* for both constant and non-constant Q. The values plotted correspond to near-source model 4. The m_b values have been normalized at $t^* = 0.0$ to enable comparison between the slopes of the individual curves. The dashed lines represent slopes of -1.0 and -2.0, for comparison with empirical results of about -1.35 as determined by Der et al. (1979; 1981).

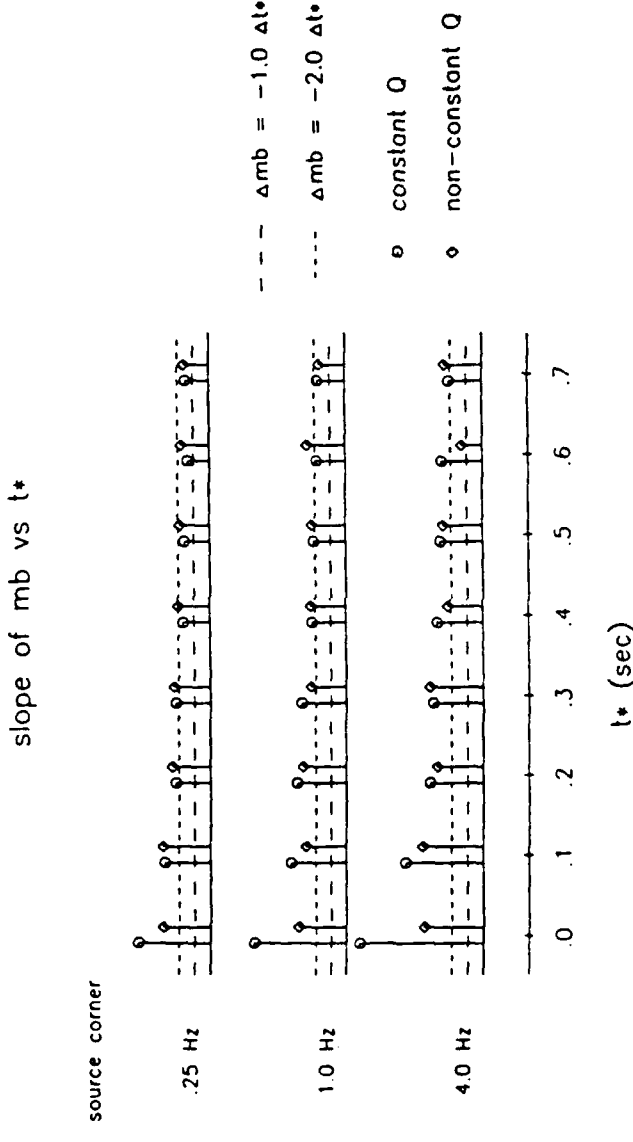


Figure 8. The slopes of the m_b vs t^* curves from Figure 7 are plotted as a function of t^* and source corner frequency. The largest slopes are found near $t^* = 0$, and for the constant Q attenuation. The slopes are steeper than 2.0 for probable values of t^* , i.e., for $t^* < .4$ seconds.

Table I m_b vs Source Corner Frequency and t^*							
t^*	model 4			model 6			
	corner frequency	0.25	1.0	4.0	corner frequency	0.25	1.0
0.0	2.44	3.85	4.64	2.04	3.34	4.83	
0.1	2.08	3.37	3.98	1.89	3.06	4.00	
0.3	1.59	2.75	3.23	1.59	2.55	2.94	
0.5	1.22	2.26	2.60	1.29	2.20	2.40	

As mentioned previously, the waveforms computed in this experiment do not resemble observed short-period teleseismic recordings of explosions in one important aspect. In all cases, even cases including high t^* values, the initial (compressional) pulse is relatively larger than usually observed from teleseismic explosions. This implies that the simple seismogram model used in Equation 1 is not adequate for describing all the features of observed signals. A notable component which has been omitted from the simulations is scattering from earth inhomogeneities. Numerical studies (Richards and Menke, 1983) have shown that the effect of scattering by random thin layers is to delay the arrival of the higher-frequency energy relative to the lower frequency energy. Note that this effect is not minimum phase, and would tend to reduce the relative amplitudes of the first half-cycles of motion in Figures 1-9 and 4-6, since these portions have a relatively high frequency content. Bache *et al.* (1985) have also attributed the differences in relative amplitudes of initial pulses between observed and synthetic P waveforms to the reversed dispersion of earth scattering.

Figures 9-10 show the effects of changing the pP delay times on seismic waveforms for both constant and frequency-dependent Q models. The reflection coefficient has an amplitude of -0.5. The numerical values adjacent to each trace in Figures 9 and 10 are the peak absolute amplitudes of the signals. As can be seen, the waveform shapes change considerably with changing pP delay times. The magnitude changes by only 0.1 - 0.2 magnitude units, although the rate of change is rather rapid for reflection times between 0.1 and 0.3 seconds. The periods associated with the m_b measures for these waveforms are shown in Figure 11. These periods were measured as twice the time between the first trough and subsequent peak. Note that changing t^* changes the character of the waveforms so that the period is not a smooth function of t^* . This is due to the interference effects of the pP reflection. Figure 11 shows that shorter pP delay times tend to result in a shorter-period signal for given t^* , and that, in most cases, even large values of t^* do not produce signals having periods greater than one second when the corner frequency is 1 Hz. The variation of t^* over the wide range of 0.0 to 0.7 seconds and over the different Q models causes a variation in period of less than 0.4 seconds, which is less than a factor of two. A general result from all of the synthetics is that pP is unlikely to be observed as an identifiable arrival when t^* is in a probable range, unless the delay time is about 0.5 seconds or greater.

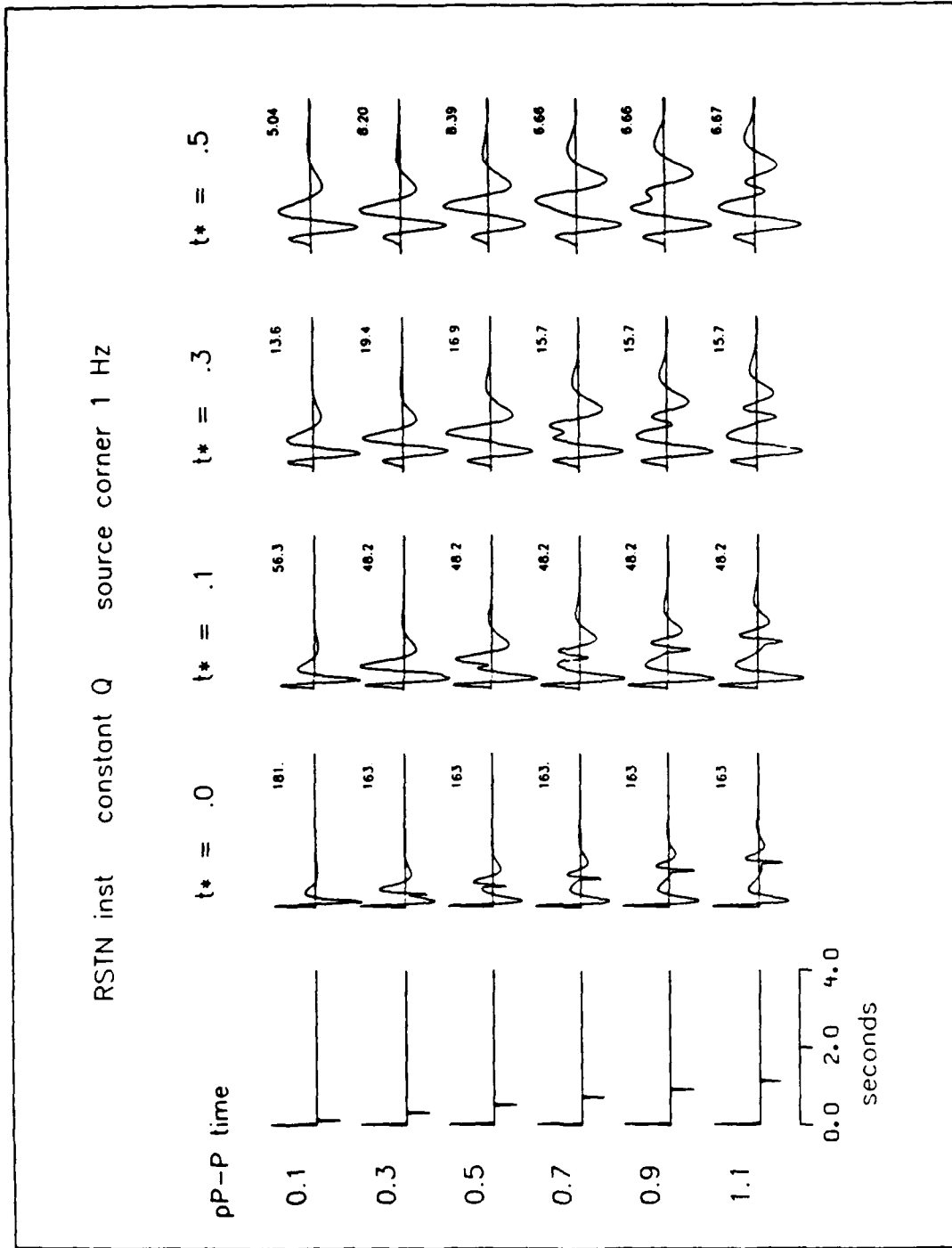


Figure 9. Synthetic waveforms constructed with a source corner of 1 Hz, constant-Q attenuation and various near-source reflectivity models as shown in the left column. The pP coefficient amplitude is -0.5 and the delay time varies from 0.1 to 1.1 seconds. The peak amplitude of each signal is also indicated.

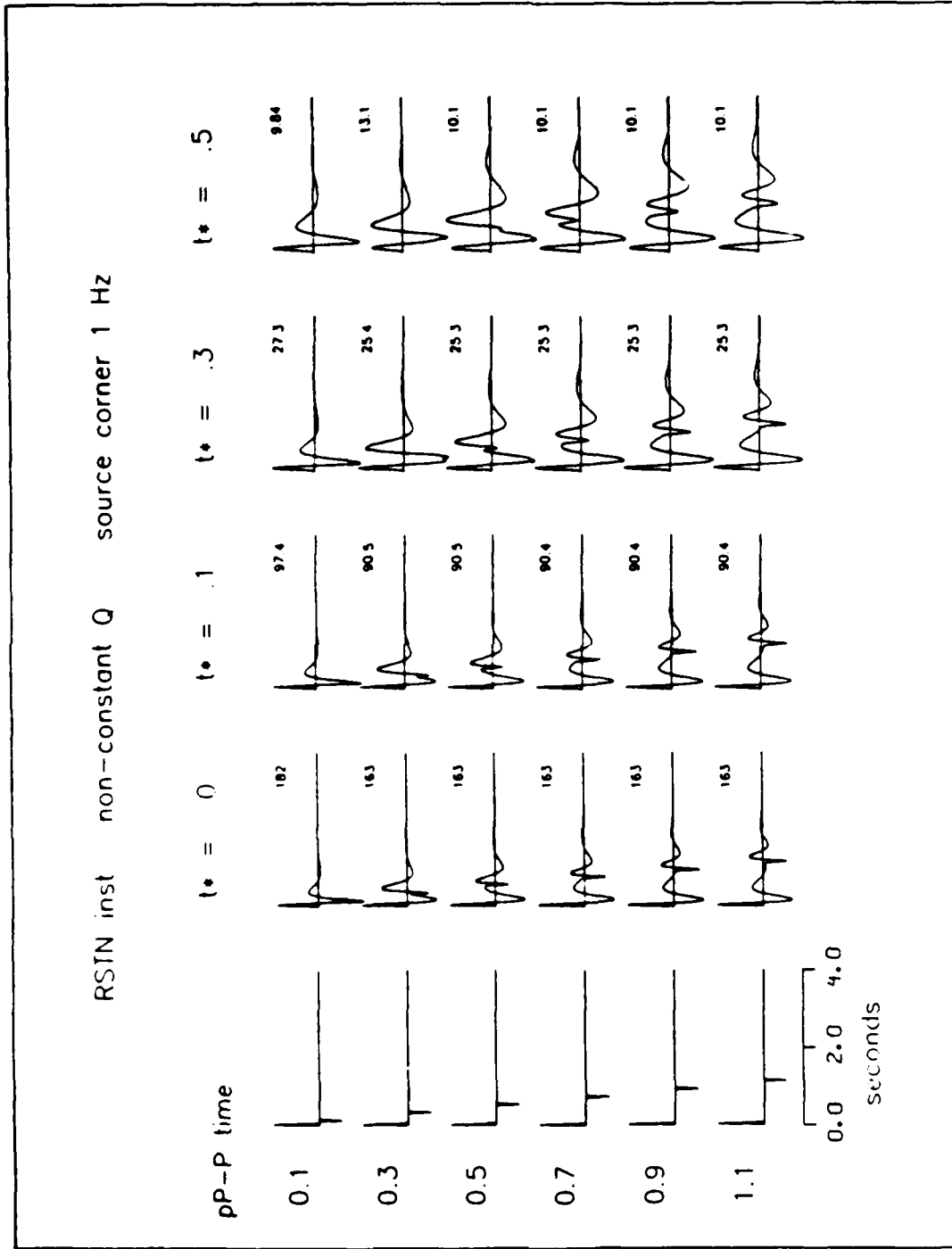


Figure 10. Seismograms constructed identically to those in Figure 9 except the attenuation model was based on non-constant Q.

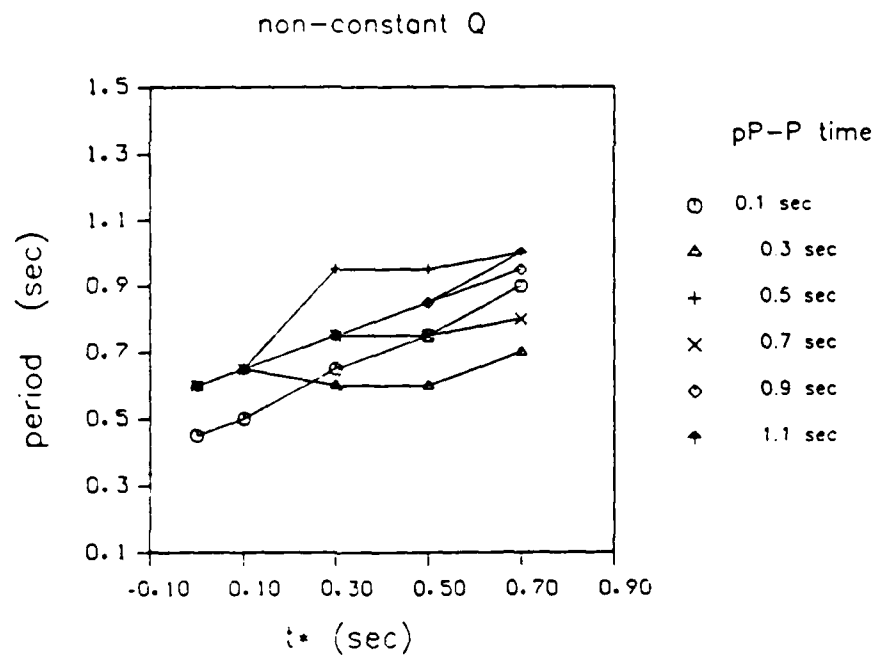
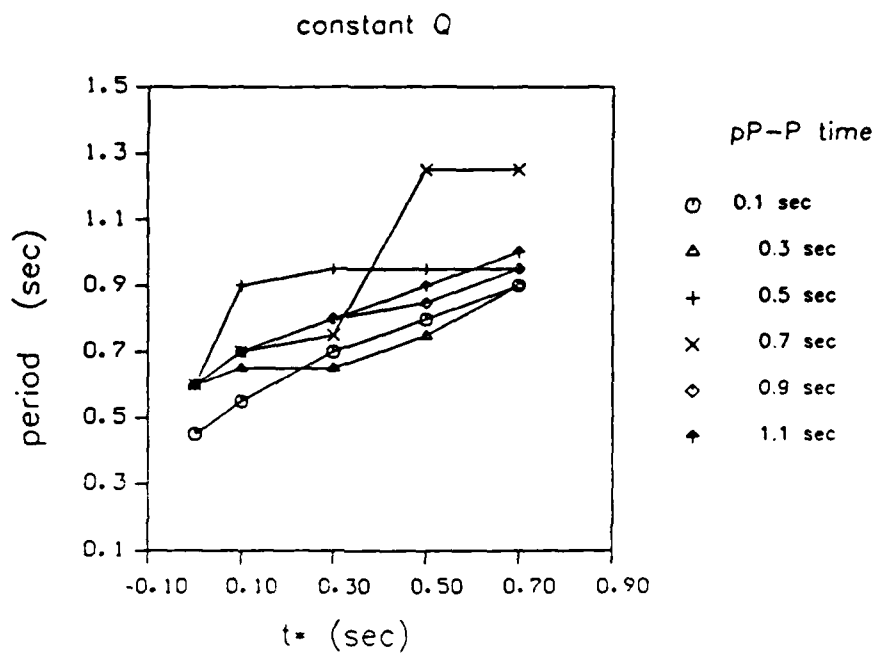


Figure 11. The periods of the waveforms in Figures 10 and 11 are plotted as a function of t^* . The period was measured as twice the time between the first trough and subsequent peak. The periods tend to increase with t^* and are not smoothly varying because of the interference effect of pP.

4.1.3. Analysis of RSTN Data

In the second part of this study, attenuation, in addition to that experienced by the propagating seismic signals, was applied to RSTN short-period teleseismic recordings of five underground nuclear explosions. This additional attenuation alters the amplitude and phase and thus the waveform shapes and corresponding m_b values. The additional attenuation can be applied by convolving the signals with the usual attenuation operator, since the assumption of linearity allows us to write for the amplitude

$$\begin{aligned} e^{-\pi f t^*_{tot}} &= e^{-\pi f (t^*_{earth} + t^*_{add})} \\ &= e^{-\pi f t^*_{earth}} e^{-\pi f t^*_{add}} \end{aligned}$$

where

f is frequency,

t^*_{tot} is the total attenuation,

t^*_{earth} is the attenuation experienced by the propagating seismic waves, and

t^*_{add} is the additional attenuation applied in the study.

Similarly, the phases are additive. As in the synthetic study, the minimum-phase spectrum was computed using the Kolmogorov method.

The added attenuation term t^*_{add} is independent of frequency in this study. Cormier (1982) cites evidence that the differential attenuation between two regions is nearly independent of frequency, so that the differential attenuation between two sites can be approximated by a frequency-independent t^* . Thus, the addition of a frequency-independent Q model in this study gives a conservative result, in terms of the effects on the seismic signals, relative to the addition of a frequency-dependent Q model, which would have less attenuation at high frequencies.

The top traces in Figures 12, 13 and 14 show the P-waves from five different underground nuclear explosions recorded at two different sites in North America. Three of the events are located in the Nevada Test Site and two are at the Semipalatinsk test region in East Kazakh. The locations and origin times of these events are given in Table II. The first four events in Table II were recorded on short-period instruments at RSTN stations RSNY and RSON. The fifth event, Piledriver, was originally recorded on a short-period LRSM instrument at station RKON, which is the present-day site RSON. The LRSM instrument response was removed from this recording and a RSTN short-period instrument response applied in order to permit a direct comparison with the other RSTN recordings. Piledriver was not recorded at the RSNY site. These two stations were

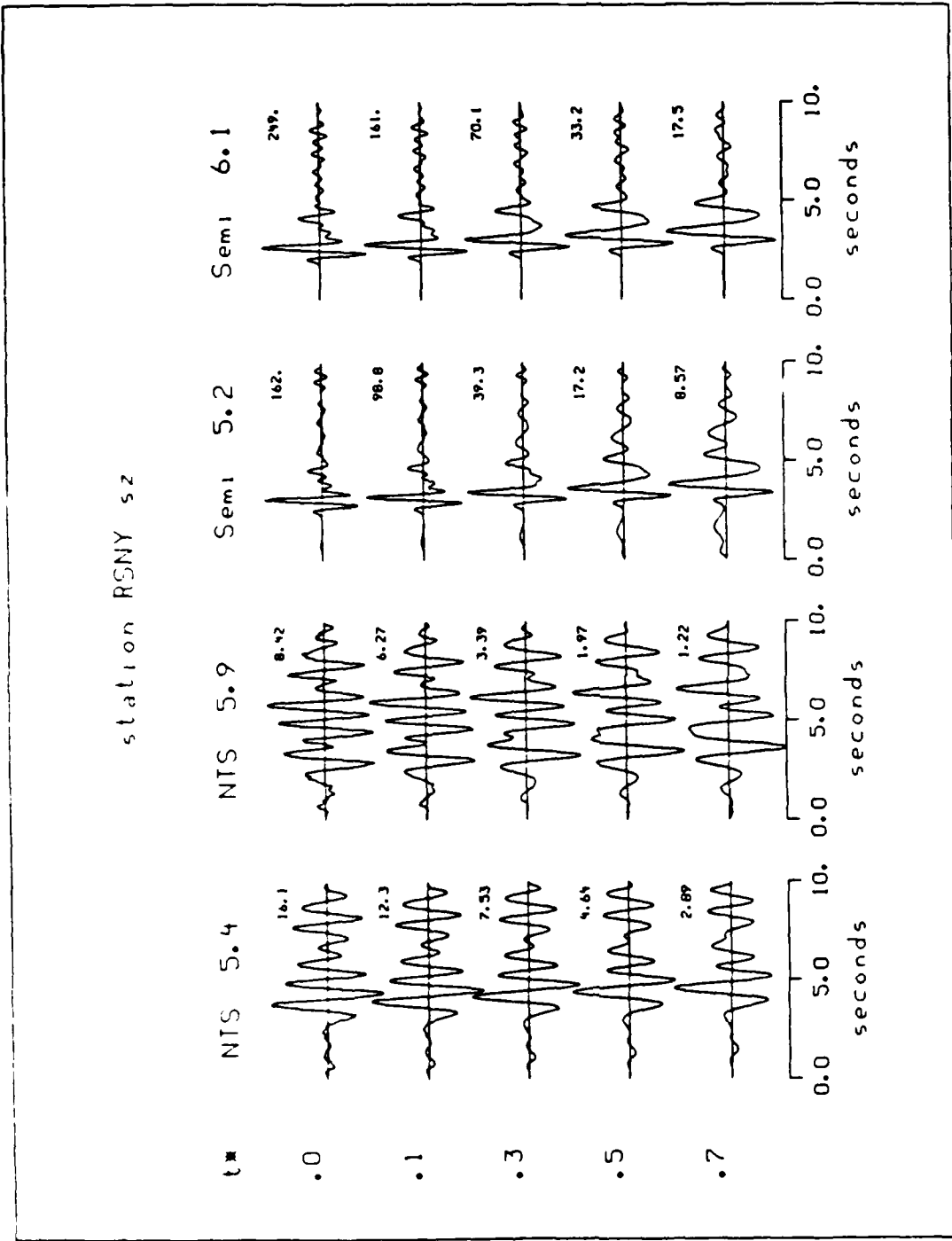


Figure 12. The P-wave signals in the top row were recorded at station RSNY from four underground nuclear explosions listed in Table II. The subsequent rows show the waveforms after various amounts of additional anelastic attenuation has been applied. The additional attenuation was based on a constant-Q model. The numerical values adjacent to the waveforms represent the peak absolute amplitudes of each signal. Note the more complex waveforms associated with the NTS events.

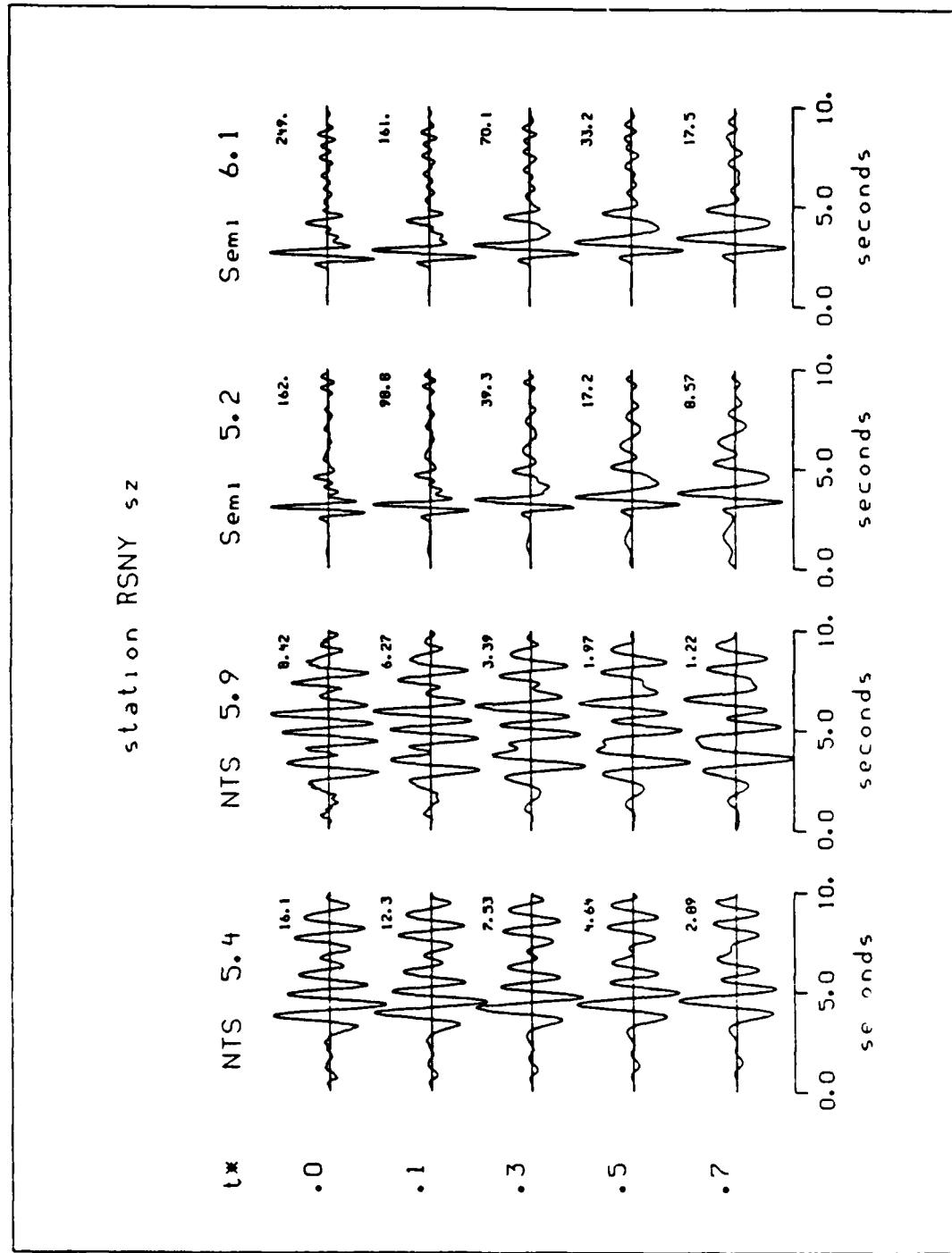


Figure 19. P-wave signals recorded at station RSNY from four events in Table II. The amount of additional attenuation applied is indicated by the value of t^* on the left-hand side and was based on a constant-Q model.

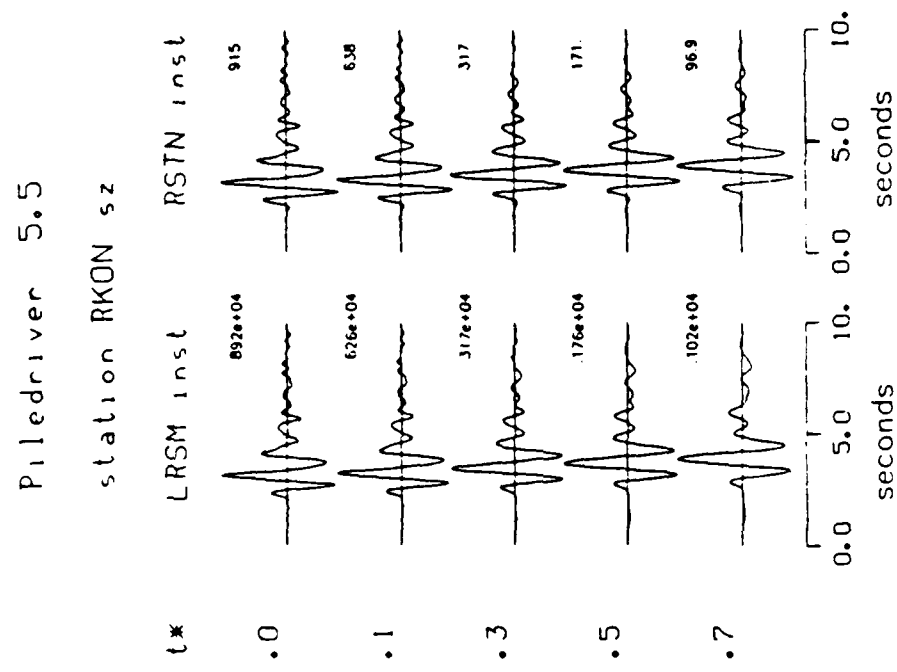


Figure 14. Vertical P-wave signals measured at station RKON from the Piledriver explosion in 1966. The original LRSM instrument recording is shown on the left; this instrument has been replaced by a RSTN short-period instrument response on the right. Levels of added attenuation are indicated by the values of t^* .

selected for this analysis because they are both located within shield-type geologic terrains. The numerical values adjacent to each waveform are the peak absolute amplitudes of the traces in units of digitization counts $\times 10^{-2}$.

Table II

event	year	day	latitude	longitude	m_b	location
NTS 5.4	1984	344	37.3 N	116.4 W	5.4	Nevada Test Site
NTS 5.9	1984	061	37.2 N	116.1 W	5.9	Nevada Test Site
Semi 5.2	1984	337	50.1 N	79.2 E	5.2	Semipalatinsk
Semi 6.1	1984	301	50.0 N	78.9 E	6.1	Semipalatinsk
Piledriver 5.5	1966	153	37.1 N	116.0 W	5.5	Nevada Test Site

The Piledriver explosion was located in the Nevada Test Site and within the Climax Stock, a competent granitic intrusive of Cretaceous age (USGS report, 1983). This distinguishes Piledriver from the two other NTS events which were located nearby but within Tertiary volcanic tuffs with substantially different physical properties than granite. The Semipalatinsk events are generally accepted to be situated within a competent host rock with properties comparable to the Climax Stock granite.

The top traces in Figures 12, 13 and 14 show distinct differences between the waveforms associated with the different source-rock types. The P-wave coda for the two 1984 NTS events are more complex and longer in duration, and their waveforms generally have longer periods. The second through fifth traces of Figures 12-14 show the effects of applying additional attenuation to the original recordings. As may be seen, attenuation applied to the Semipalatinsk and Piledriver recordings does not produce signals that match the complexity and duration of the 1984 NTS events. The added attenuation simplifies the P-coda complexity by removing high-frequency energy. Figures 12 and 13 show that the first few cycles of motion for the Semipalatinsk events are shorter in period than the first few cycles of the NTS events. Additional attenuation of more than $t^* = 0.3$ seconds for RSON and even more for RSNY must be introduced before the periods of the first few cycles become comparable for the two test sites. The corresponding change in m_b , if we were to assume that absorption is the cause of the period differences, would be 0.6 to 1.0 magnitude units or larger. On the other hand, the Piledriver waveform at RKON appears quite similar to the Semipalatinsk recordings at RSON. The first few cycles of the Piledriver recording are also relatively high frequency, although not quite as high as the Semipalatinsk signals. These observations strongly suggest that the lower-frequency, longer-duration recordings from NTS explosions are not evidence for increased attenuation under NTS, as sometimes reported, but rather are caused by different near-source effects and coupling differences.

Der *et al.* (1984) have estimated a differential in t^* of 0.2 to 0.3 seconds between the East Kazakh and Nevada Test Site regions. Their analysis was performed by a linear regression in the frequency domain on a suite of short-period recordings. Der *et al.*, attribute this t^* differential between the two sites to lateral changes in the anelastic

attenuation properties of the upper mantle. Evidence for t^* differences may be found in *Figure 15*, which summarizes the change in m_b with additional attenuation for these five events. Plotted in *Figure 15* are values of m_b measured for the original waveforms minus m_b measured from the waveforms with attenuation added. The m_b values were computed using the first trough and subsequent peak -- the so-called "c" method. Also plotted are lines corresponding to the equations $\Delta m_b = -1.0\Delta t^*$ and $\Delta m_b = -2.0\Delta t^*$. The interesting features in these plots are the slopes of the Δm_b vs Δt^* curves near $\Delta t^* = 0$. *Figure 15* shows that m_b generally falls off faster with added attenuation for the Semipalatinsk events than for the NTS events. The Piledriver and NTS 5.9 recordings at RSON having intermediate slopes. The synthetic experiments showed, in *Figures 7 and 8*, that the slope of Δm_b vs Δt^* is a function of t^* . Thus, the faster fall-off of m_b with Δt^* for the Semipalatinsk events suggests that these signals have experienced less attenuation along their paths than have the signals from NTS. While the method is not very sensitive, if we shift the Soviet m_b vs t^* curve to match the slope of the Piledriver curve, the best fit occurs for a Δt^* of about 0.2 seconds, suggesting that the Piledriver signal had undergone that amount of additional absorption. This does support frequency-domain studies that indicate t^* differences between the two test sites. We note, however, that the differences in slopes may also be attributed to differences in corner frequencies or near-source effects rather than attenuation.

Although the data set used in this experiment is clearly limited in extent, the results do indicate that differences in the P-waveforms and m_b values exist between the NTS and Semipalatinsk test sites which are consistent with an anelastic attenuation differential of the order $t^* = .2 - .3$ seconds, but which could very likely be the result of differences in coupling and other near-source effects.

4.1.4. Summary

The results of the first part of this study involving synthetic seismograms indicated the relationship between m_b and t^* is a strong function of the source corner frequency and the assumed frequency dependence of earth attenuation. Differences of about one-half octave in corner frequency affect magnitude by the same amount as t^* differences of about 0.1 seconds. A value for t^* as small as 0.1 seconds appears to be inconsistent with explosion waveforms as observed because of the large relative amplitudes of the onsets of motion. This discrepancy between synthetics and observed signals may be attributed to forward-scattering effects, which were not included here. The complexity of the early P-wave coda is very sensitive to near-source reflections for low attenuation, but less so for $t^* = 0.3$ seconds or greater. When measured within the first few cycles of motion, m_b was found to vary by more than 0.3 magnitude units for different near-source reflection configurations. The proportionality constant between Δm_b and Δt^* for realistic values of t^* as determined from the synthetic study was considerably larger than the empirically derived value of -1.35 by Der *et al.* (1979; 1981).

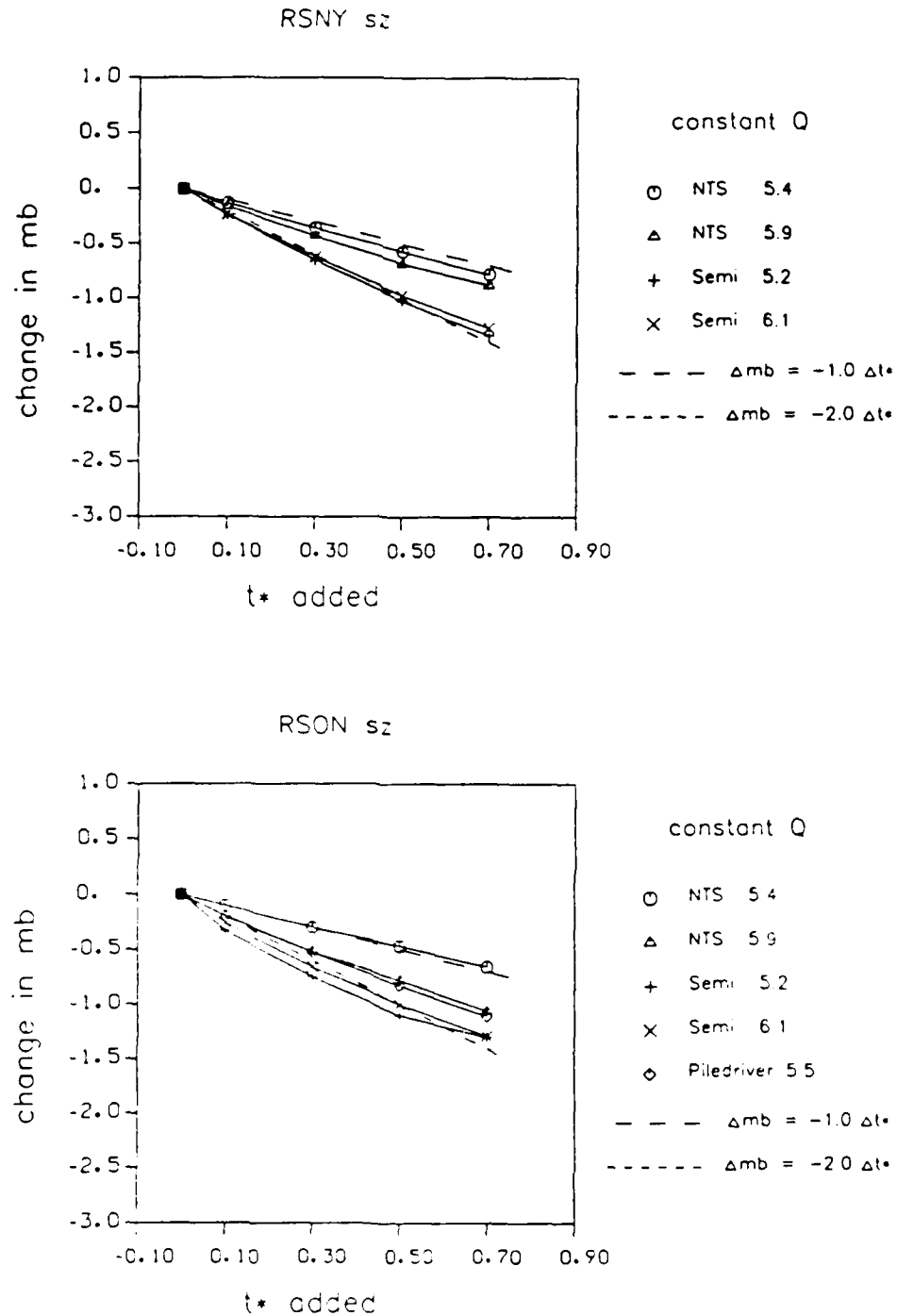


Figure 15. Variation in m_b with additional t^* for the five events in *Table II*. The m_b values have been normalized at $t^* = 0.0$ to enable a comparison of the slopes of the curves.

The second part of the study, in which additional anelastic attenuation was applied to RSTN short-period recordings of teleseismic nuclear explosions, showed that the waveforms and relationship between m_b and additional attenuation differs substantially between explosions at Semipalatinsk and those in volcanic tuffs at NTS. The waveforms of the Piledriver shot, located in granitic material at NTS, appear very similar to those recorded from Semipalatinsk. The Semipalatinsk signals, which may have experienced less attenuation along their paths to the RSTN sites, have a greater sensitivity to additional attenuation than do the NTS signals. However, the dominant frequency content and early P-wave coda complexity for the NTS events cannot be explained by a simple difference in t^* between the two test sites. Comparison with the model study results suggests that source coupling, scattering, and near-source reflections should be used to fully explain the observations.

4.1.5. Acknowledgments

Dr. D. Baumgardt kindly provided the digitized recording of the Piledriver event and the LRSM instrument response.

Andy Jurkevics and Carl Romney

REFERENCES

- Bache, T. C., Barker, T. G., Rimer, N., and Cherry, J. T., 1980. "The Contribution of Two-Dimensional Source Effects to the Far-Field Seismic Signatures of Underground Nuclear Explosions," *S-Cubed Report*, SSS-R-80-4569.
- Bache, T. C., Marshall, P. D. and Bache, L. B., 1985. "Q for Teleseismic P Waves from Central Asia", *Jour. Geophys. Res.*, Vol. 90, pp.3573.
- Breding, D., 1983. "User's Guide for the Regional Seismic Test Network (RSTN)," *Sandia Report*, SAND 82-2935.
- Claerbout, J. F., 1976. "Fundamentals of Geophysical Data Processing: With Applications to Petroleum Prospecting," *McGraw-Hill, Inc.*
- Cormier, V. F., 1982. "The Effect of Attenuation on Seismic Body Waves," *Bull. Seism. Soc. Am.*, Vol. 72, pp.S169.
- Der, Z. A., McElfresh, T. W., and Mrazek, C. P., 1979. "Interpretation of Short-Period P-Wave Magnitude Anomalies at Selected LRSM Stations," *Bull. Seism. Soc. Am.*, Vol. 69, pp.1149.
- Der, Z. A., McElfresh, T. W., and O'Donnell, A., 1981. "Results of the SDCS (Special Data Collection System) Attenuation Experiment," *Teledyne Geotech Report*, VSC-TR-81-14.
- Der, Z. A., McElfresh, T. W., Wagner, R., and Burnett, J., 1984. "Spectral Characteristics of P-Waves from Nuclear Explosions and Yield Estimation," paper submitted to *Bull. Seism. Soc. Am.*
- Perl, N., Thomas, F. J., Trulio, J., and Woodie, W. L., 1979. "Effects of Burial Depth on Seismic Signals," *Pacific Sierra Research Report*, PSR-815.
- Richards, P. G. and Menke, W., 1983. "The Apparent Attenuation of a Scattering Medium," *Bull. Seism. Soc. Am.*, Vol. 73, pp.1005.
- U.S.G.S. report, 1983. "Geologic and Geophysical Investigations of Climax Stock Intrusive, Nevada," *United States Geological Survey Open-File Report*, USGS-OFR-83-377.
- von Seggern, D. and Blandford, R., 1972. "Source Time Functions and Spectra of Underground Nuclear Explosions," *Geophys. Jour. R.A.S.*, Vol. 31, pp.83.

F N O

D T / C

10 — 86